Institute for
Communications
and Navigation

TUM

Modeling of Barometric Altimeter Measurements to support Geodetic Altitude Navigation

Maximilian Simonetti

Master's Thesis

Institute for Communications and Navigation

Prof. Dr. Christoph Günther

Supervised by Prof. Dr. Christoph Günther, TUM
Omar García Crespillo, DLR

Munich, July 2021

Institute for Communications and Navigation
Technische Universität München
Theresienstrasse 90
80333 Munich

Acknowledgements

I would like to thank Professor Günther for giving me the rewarding opportunity of working on my master's thesis at the DLR Institute of Communications and Navigation.

I want to express my gratitude to Omar García Crespillo too for his careful supervision and his constant support.

My deep gratefulness goes also to my brothers, my friends and Arianna for their cheering daily presence in my life despite the hundreds of kilometers that have sometimes been between us.

My final and deepest thankfulness to my parents. I owe them everything.

Abstract

Vertical Navigation is of great importance for safe aircraft navigation and guidance, which have been for decades based on standard pressure altitude to support the determination of aircrafts flight levels. This altitude is obtained from airborne pressure measurements performed by barometers and is referenced to the International Standard Aatmosphere Mean Sea Level isobar surface.

Standard pressure altitude deviates from true geodetic altitude, that is the one used by GNSS and referenced to an Earth's reference ellipsoid, up to several hundreds of meters for aircrafts flying at typical civil aviation cruise altitudes.

Accurate and reliable geodetic altitude navigation is necessary and critical for airport vicinities operations and for new applications like Urban Air Mobility or Alternative Positioning Navigation applications. Although Inertial Navigation Systems and Global Navigation Satellite Systems are able to provide geodetic altitude estimation, both kinds of navigation systems show normally poorer performances in vertical navigation than in the horizontal one.

First, this thesis investigates the accuracy in the computation of geodetic altitude from a corrected pressure altitude computed with barometric pressure and external weather data. This computation method is herein shown to remarkably reduce the deviation of the standard pressure altitude from the true geodetic altitude.

Secondly, this work derives two robust error models to support the use of barometric pressure measurements for safe geodetic altitude navigation. The first overbounding model is suitable for the use in snapshot (i.e., single-epoch) algorithms. The second dynamic overbounding model is suitable to be included in sequential estimators and in those applications where the time correlation of the pressure measurements must be properly taken into account.

The evaluation of the accuracy obtained in computing geodetic altitude from the corrected pressure altitude as well as the analysis of the residual error models is obtained by the use of data gathered during more than 20 flight hours performed with the Dassault Falcon 20-E5 aircraft within a DLR flight tests campaign.

Contents

1 Introduction

Vertical navigation is crucial in aviation to ensure safe aircraft vertical separation and safe estimation of distance from the ground or other obstacles. Traditionally, vertical separation between airplanes is enabled via the use of standard pressure altitude and the concept of flight levels, which is strictly related to the former [1, 2].

Airborne barometric measurements are used within Air Data Systems to provide an altitude above the International Standard Atmosphere's (ISA) mean sea level (MSL) isobar. This altitude is referred to as standard pressure altitude.

By referring to this isobar, which is defined by a constant value, it is enough for vertical separation to be successful that barometers onboard different airplanes provide accurate pressure measurements. Anyway, the more the actual MSL pressure and temperature differ from the ones assumed by the ISA, the more the standard pressure altitude will differ from the true geodetic altitude.

When flying at lower altitudes than cruise flight altitudes, it is of interest also to have reliable information about the distance from ground or other obstacles. For this purpose, vertical navigation is in these circumstances based on corrected pressure altitude [3, 4, 5]. This kind of pressure altitude is obtained by trying to account for the actual pressure and temperature values at MSL and also for a different evolution of temperature with altitude than the one assumed within the standard pressure altitude equation.

Even in this case, remarkable differences between the values of pressure altitude and the ones of true geodetic altitude are to be expected. This is due to the fact that these two altitudes differ both in regard to their references and their scales and that the atmosphere does not behave as it is assumed to do by the ISA model. Pressure altitude is referenced to an isobar, which is the ISA MSL in the case of standard pressure altitude, while geodetic altitude's reference is the Earth's ellipsoid. The scales are the geopotential and the geometric one for pressure and geodetic altitude, respectively.

Apart from pressure altitude, pressure measurements may also be used, along with wind and aircraft velocity measurements and temperature measurements, to produce geometric altitude above MSL with an iterative algorithm, known as the Blanchard algorithm [6, 7].

1.1 Motivation

In the vicinities of airports, geodetic altitude navigation is crucial for precision approaches and automatic landing. It has also been shown that accurate vertical infor-

mation is fundamental to support APNT horizontal positioning [8]. Furthermore, new UAV applications will need geodetic altitude information for air traffic management in the vicinity of cities to sustain a broad range of Urban Air Mobility use cases. Additionally, the accuracy obtained with pressure altitude, when directly used as geodetic altitude, is not enough to satisfy geodetic requirements in new Performance Based Navigation (PBN) or vertical requirements of UAVs.

Navigation algorithms based on INS integration with GNSS are able to provide geodetic altitude information. Anyway, the inherent instability of the INS vertical channel [9] and the poorer performances of GNSS in vertical navigation [10] than in the horizontal one, along with the numerous threats to GNSS integrity, reduce the accuracy of their provided geodetic altitude information.

Other aiding navigation subsystems are therefore needed to provide robust back-ups to INS&GNSS systems. Given the robustness of their measurements, barometers may be listed among these aiding subsystems for geodetic altitude navigation. The use of barometric altimeters for this purpose, anyway, requires rigorous conversions to geodetic altitude by considering the differences in reference and scale.

In scientific literature, work related to the translation of both altitudes obtained from pressure measurements—pressure altitude and altitude from the Blanchard algorithm—to geodetic altitude can be found [11, 12, 13]. This previous research, anyway, generally lacks rigorous translations to geodetic altitude and/or does not consider the possibility of using external weather data in the pressure altitude equation.

Additionally, some of the previous work focuses on the integration of pressure altitude into multi-sensor navigation algorithms [14, 15, 16]. The methodologies to obtain robust models for the pressure altitude errors, i.e., for its deviations from true geodetic altitude, are rarely mentioned and it may be assumed that tuning approaches are followed.

Furthermore, simulations are often considered in previous research, meaning that realistic errors are not necessarily always portrayed.

1.2 Objectives

This thesis intends to fill these technology gaps by, first, assessing the accuracy of the two aforementioned methods to obtain geodetic altitude from airborne pressure measurements at typical civil aviation altitudes. This is done via a careful conversion both with respect to the differences in scale and reference.

In particular, regarding the option featuring pressure altitude, this work has the goal of analyzing the effect of extensive use of external weather data on the thereby computed corrected pressure altitude.

Additionally, this thesis aims at performing a rigorous error modeling of the residual errors in the geodetic altitude obtained from the corrected pressure altitude. This is a necessary step for future integration of this altitude information in navigation algorithms. In particular, the goals are to derive an overbounding error model for snapshot algorithms—used for example within APNT applications—and one for sequential estimator algorithms, used for the integration with, e.g., INS/GNSS-based navigation sys-

tems.

Finally, this thesis analyzes how the weather data would be considered when attempting to integrate this geodetic altitude in an exemplary sequential estimator.

1.3   Thesis Structure

Chapter 2 summarizes the most relevant theory underlying this work and in particular presents in mathematical terms the different concepts associated to altitude in aircraft navigation.

In Chapter 3, a selection of the relevant scientific literature is reviewed, in order to identify the path this thesis proceeds along.

Chapter 4 describes the methodologies adopted in this work to obtain geodetic altitude from pressure measurements via the Blanchard algorithm and through the corrected pressure altitude.

Chapter 5 focuses on the test flights which provided the data this thesis's analyses are based on. Additionally, it explains the flight tests' processing that needed to be performed before applying the aforementioned methodologies. The results of the latter are presented and discussed in Chapter 6.

Chapter 7 describes how to compensate for the aircraft dynamics effects on the geodetic altitude obtained from the pressure altitude corrected with weather data. In this chapter, the methodology employed to model the residual geodetic altitude errors for snapshot navigation algorithms is presented. This chapter also includes the results of the presented methodology.

Chapter 8 presents the procedure to model the residual errors for sequential navigation estimators and describes how to consider the external weather data within an exemplary sequential estimator. The results of this methodology are shown and discussed in the same chapter.

The thesis is concluded with Chapters 9 and 10, which provide this work's conclusions and future prospects, respectively.

Appendices A, B and C provide additional theory concepts related to this work.

2 Altitude Definitions

This chapter provides a summary of the most relevant theory underlying this work. First, the different definitions associated to the concept of altitude are given in Section 2.1. Then, pressure altitude and its corrections are described in Sections 2.2 and 2.3. The Blanchard's algorithm for altitude computation follows in Section 2.4.

2.1 Geoid, Ellipsoid and Altitude Scales

In navigation, the Earth's surface, which is actually irregular, may be assumed to be as an oblate ellipsoid of revolution, with the equatorial diameter being longer than the line connecting the geographic poles. Two examples of Earth's ellipsoidal models are the Geodetic Reference System 1980 (GRS80) and the World Geodetic System 1984 (WGS84). Both models have their origins in the Earth's center of mass, but they provide slightly different values for the equatorial and polar radii [9].

In this work, the WGS84 model is used, since this is also the model employed by GPS [9]. A further reason for this choice is that the European Centre for Medium-Range Weather Forecasts (ECMWF) provides weather data referenced in the horizontal plane with respect to the WGS84 [17, 18], as will be explained in Section 4.1.

The geodetic altitude (or height) h is the distance from a given point to the ellipsoidal surface along the normal to this surface, as shown in Figure 2.1. In this thesis, a positive value of h corresponds to a location in outside the ellipsoid whilst the opposite is true for a negative value of h.
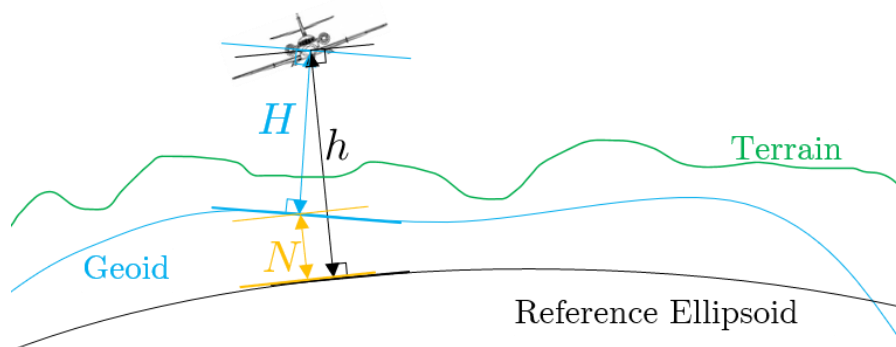

Figure 2.1: Geodetic Altitude, Orthometric and Geoid Height (based on [9])

Another kind of altitude is the orthometric altitude, denoted by H. Since its definition is strictly connected to the geoid surface, the concept of the geoid shall be intro-

duced.

The geoid is a model of the Earth's surface defined as the equipotential surface of the Earth's gravity field—the sum of gravitational and centrifugal acceleration fields—which best fits, in a least squares sense, global mean sea level (MSL) [19]. Since water tends to maintain a constant and in particular the lowest achievable potential energy, it is expected that the geoid almost coincides with the mean sea level. This is the level of the oceans averaged over the tide cycle. Indeed, the geoid offsets from the actual mean sea level are within 1 meter [9].

The distance from a point to the geoid surface along the normal to this surface is called orthometric altitude or altitude (or height) above mean sea level, often shortened to altitude AMSL. It is related to the geodetic altitude through

$$H \approx h - N(L, \lambda) \, , \qquad (2.1)$$

where N denotes the geoid undulation (or height), that is the altitude of the geoid referenced to the ellipsoidal surface, being this positive when the geoid surface at the current location is outside the ellipsoid. The geoid undulation, which is a function of latitude, L, and longitude, λ, ranges worldwide between approximately 105 and 85 meters and takes, exemplarily, the value of 46 meters in Oberpfaffenhofen, Germany.

The worldwide inhomogeneity of geodetic undulation is due to inhomogeneous distribution of the gravity potential on the ellipsoid surface. This, in turn, is caused by the changing value of the centrifugal potential with latitude and the heterogeneous distribution of Earth's mass, that is responsible therefore for a heterogeneous gravitational potential. In Figure 2.2, geoid undulations obtained from the Earth Geopotential Model 1996 (EGM96) are shown.
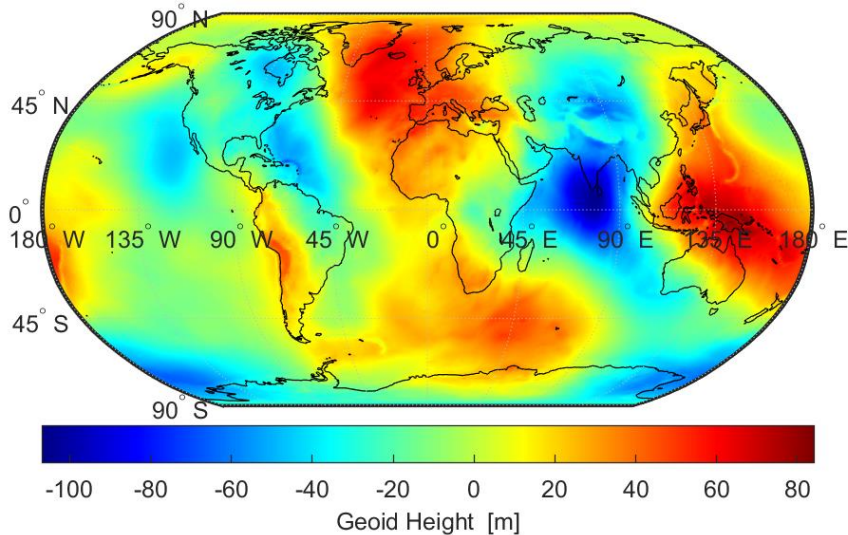

Figure 2.2: Geoid Undulations from the EGM96

As expressed by Equation (2.1), the conversion between orthometric and geodetic altitude is approximated rather than exact, because, at a given location, the normal to the geoid is not necessarily aligned with the normal to the ellipsoid. This can be seen in

14

Figure 2.1.

Geodetic and orthometric altitude are both geometric altitudes, meaning that their scale is geometric. In general, that the scale of the altitude of a point with respect to a reference surface is geometric, indicates that its values correspond to what would be read on a hypothetical ruler connecting the point to the surface along the normal to that surface. This concept is therefore quite much self-explained and intuitive and its definition may appear as superfluous. Nevertheless, it is needed to be pointed out in order to distinguish it from the geopotential altitude scale, which is a key concept in weather sciences.

The geopotential altitude scale is the scale of the geopotential altitude above MSL, that is the virtual altitude of a point above MSL obtained when taking into account the geographic and vertical effects of gravity anomalies [20]. Put in other words, the geopotential altitude AMSL is a measure of the specific potential energy at the corresponding geometric altitude at a given location [21]. In order to provide a mathematical definition for this concept, the gravity potential Φ, at a given latitude, longitude and orthometric altitude—with the MSL as reference—shall be defined: [20]

$$\Phi(L, \lambda, H) = \int_0^H g(L, \lambda, z)dz \quad , \tag{2.2}$$

where g is the acceleration due to gravity and is a function of position.

As a result, the geopotential is merely a function of position and does therefore not depend on atmospheric quantities. Equivalently, a surface of constant geopotential varies with latitude, longitude, and altitude only [20].

Geopotential altitude AMSL, Z_g^{msl}, is then defined as [20]

$$Z_g^{msl}(L, \lambda, H) = \frac{\Phi(L, \lambda, H)}{g_0} = \frac{1}{g_0} \int_0^H g(L, \lambda, z)dz \quad , \tag{2.3}$$

where g_0 is the average MSL acceleration due to gravity, also called standard gravity acceleration, and takes the value 9.80665 ms^{-2}. As a result, the geopotential altitude AMSL at a given location will be larger than the corresponding orthometric altitude if the local gravity acceleration is higher than the standard one, whereas at MSL both altitudes will be zero [20].

Because of the difficulty of solving this integral, a relatively simple model for gravity may be introduced in Equation (2.3) to allow for an analytical solution. This model is based on the Somigliana model, which provides the value of normal gravity at the Earth's ellipsoidal surface, denoted by γ, as a function of latitude [20]:

$$\gamma(L) = \frac{R_e \gamma_e \cos^2 L + R_p \gamma_p \sin^2 L}{\sqrt{R_e{}^2 \cos^2 L + R_p{}^2 \sin^2 L}} \quad . \tag{2.4}$$

In Equation (2.4), R_e = 6378137.0 m and R_p = 6356752.3142 m denote the WGS84 equatorial and polar radii, respectively, while γ_e =9.7803253359 ms^{-2} and γ_p =

15

9.8321849378 ms^{-2} are the equatorial and polar gravity accelerations at the ellipsoidal surface, respectively.

Because of numerical issues, Equation (2.4) may be simplified to [22]

$$\gamma(L) = \gamma_e \frac{1 + k \sin^2 L}{\sqrt{1 - e^2 \sin^2 L}} \quad , \tag{2.5}$$

with

$$k = \frac{R_p \gamma_p}{R_e \gamma_e} - 1 \quad , \tag{2.6}$$

and the first eccentricity of the ellipsoid being defined as [9]

$$e = \sqrt{1 - \frac{R_p{}^2}{R_e{}^2}} \quad . \tag{2.7}$$

This simplified version of the Somigliana formula is the official WGS84 Ellipsoidal Gravity Formula [22]. Upon this surface gravity model, a model for normal gravity above the ellipsoid can be formulated by upward continuing γ by means of a truncated Taylor series expansion [23]. Under this approximation, the formula given in the WGS84 standard for normal gravity above the ellipsoid γ_{h}, is [23]:

$$\gamma_h(L, h) = \gamma(L) \left[1 - \frac{2}{R_e}(1 + f + m - 2f \sin^2 L)h + \frac{3}{R_e{}^2} h^2 \right] , \tag{2.8}$$

whereby the positive direction is the one pointing downward along the geodetic normal to the ellipsoid.

In Equation (2.8), f denotes the ellipsoid's flattening, defined as [9]

$$f = \frac{R_e - R_p}{R_e} \quad , \tag{2.9}$$

while m is a constant given by

$$m = \frac{\Omega^2 R_e{}^2 R_p}{GM} \quad , \tag{2.10}$$

with Ω and GM being the Earth's angular velocity and gravitational constant, respectively.

In an analogous way to how Geopotential altitude AMSL, $Z_{\mathrm{g}}^{\mathrm{msl}}$, was defined in Equation (2.3), geopotential height above the Earth's ellipsoid, $Z_{\mathrm{g}}^{\mathrm{wgs84}}$, may be defined as [20]

$$Z_{\mathrm{g}}^{wgs84}(L, h) = \frac{1}{g_0} \int_0^h \gamma_h(L, z) dz \quad . \tag{2.11}$$

Inserting Equation (2.8) in Equation (2.11) allows for an analytical solution of the integral in the latter equation, thus yielding [20]:

$$Z_{\mathrm{g}}^{wgs84}(L, h) = \frac{\gamma(L)}{g_0} h \left[1 - \frac{h}{R_e}(1 + f + m - 2f \sin^2 L) + \frac{h^2}{R_e{}^2} \right] \quad . \tag{2.12}$$

Figure 2.3 shows the difference between geodetic altitude, h, and $Z_{\text{g}}^{\text{wgs84}}$ as a function of latitude and geodetic altitude for latitudes ranging from -90° to 90° and for geodetic altitudes ranging from 0 to 40 km.

Being the reference of these two altitude definitions the same, i.e., the WGS84 surface, this figure expresses the difference between the geometric and the geopotential scale. As an example, the difference between these two scales at 11 km above Oberpfaffenhofen (Germany) is approximately 16.3 m.
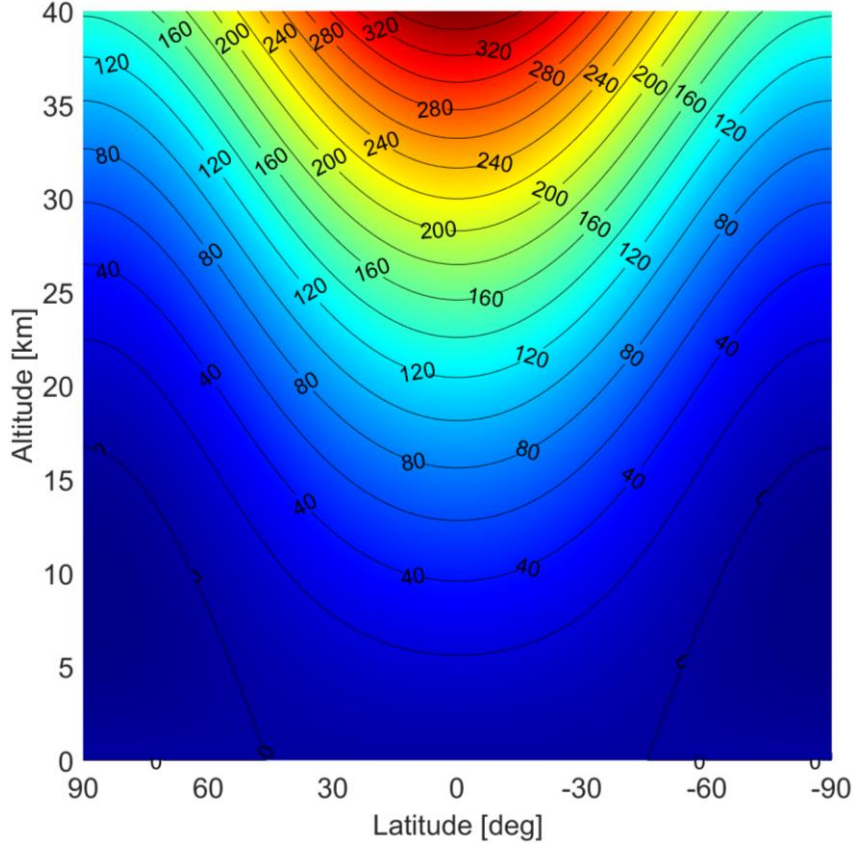

Figure 2.3: Difference between geometric and geopotential altitudes above WGS84 (reproduced with the same style adopted in [20])

In order to convert geopotential altitude above the ellipsoid, $Z_{\text{g}}^{\text{wgs84}}$, to geopotential altitude above the geoid (i.e., MSL), $Z_{\text{g}}^{\text{msl}}$, which is the altitude typically employed in atmospheric sciences [20], the following equation may be used:

$$Z_g^{msl}(L, \lambda, H) = Z_{\text{g}}^{wgs84}(L, h) - Z_{\text{g}}^{wgs84}(L, N(L, \lambda)) \ , \tag{2.13}$$

where the second term on the right side of the equation is the geopotential altitude, above the ellipsoid, of the geoid undulation [20]. The relevance of this conversion in the present work is due to the fact that the altitude information provided by ECMWF is given in terms of geopotential altitude AMSL [17].

Having defined the concepts of geoid, ellipsoid, geodetic altitude, altitude AMSL and

geopotential scale, it is beneficial to visualize them in a single grid, as it is done in Table 2.1. This way, the different altitude definitions given in the previous paragraphs may be distinguished according to two categories: the scale and the reference.

It is noted that when the scale is not explicitly mentioned, the scale will be considered to be geometric throughout this Theis. Furthermore, if no attribute at all is explicitly given for altitude, it is to be intended that the mentioned altitude is the geodetic one.

Another row will be added to this table in the next sections, in order to visualize the relationships of pressure altitude—to be defined in Section 2.2—with the aforementioned altitude definitions.

		Altitude Scale	
		Geometric	Geopotential
Reference	WGS84	Geodetic altitude h	Geopotential altitude above WGS84 Z_{g}^{wgs84}
	MSL (Geoid)	Orthometric altitude H	Geopotential altitude AMSL Z_{g}^{msl}

Table 2.1: Different altitude definitions

2.2   Pressure Altitude

Barometric altimeters are devices which have been for decades widely used in aviation for converting barometric pressure measurements in altitude information, as presented in Section 2.2.2. The principle of this conversion lies on the atmospheric model which is briefly derived and explained in Section 2.2.1.

2.2.1 Atmospheric Model for Pressure Altitude

Since the atmosphere is static with respect to the Earth, it is subject to gravity too [24]. The air static equilibrium is expressed by the hydrostatic equation, which provides a relationship between vertical change of static air pressure $\mathrm{d}p$, acceleration due to gravity g, air density ρ, and change in altitude AMSL H:

$$\mathrm{d}p = -\rho g \ \mathrm{d}H \ . \tag{2.14}$$

Approximating the atmosphere as a perfect gas, then the perfect gas law relates static air pressure to air density and static air temperature, T, as:

$$p = \rho \frac{R^* T}{M_0} = \rho R_{dry} T \quad . \tag{2.15}$$

In Equation (2.15), R^* denotes the universal gas constant and M_0 is the standard sea level molar mass of the air, as it is obtained from the perfect gas law when using the ISA standard MSL values for pressure, density, and temperature, i.e., p_0, ρ_0 and respectively [24]. The quantity derived from R^* and M_0, denoted by R_{dry}, is called specific gas constant of dry air. The values of these constants are given in Table 7.1 [24].

ISA Constants	Values
p_0	101.325×10^3 Pa
ρ_0	1.225 kg m^{-1}
T_0	288.15 K
M_0	28.96442 kg kmol^{-1}
T_1	216.65 K
α	6.5 K km^{-1}
R_{dry}	287.05287 J kg^{-1}K^{-1}
R^*	8314.32 J kmol^{-1}K^{-1}

Table 2.2: ISA Constants

Solving Equation (2.15) for density, and substituting this formulation of Equation (2.15) in Equation (2.14), yields the following:

$$\mathrm{d}H = -\frac{R_{dry}T}{gp}\mathrm{d}p \ . \tag{2.16}$$

When considering the effects of humidity, this equation changes slightly to [25]

$$\mathrm{d}H = -\frac{R_{dry}T_V}{gp}\mathrm{d}p \ , \tag{2.17}$$

where T_V denotes the "virtual" temperature, which is related to temperature through [25]

$$T_\mathrm{V} = T(1 + \epsilon q) \ . \tag{2.18}$$

In Equation (2.18), q denotes the specific humidity, i.e., the mass of water vapor per kilogram of moist air, and the constant ϵ is defined as [25]

$$\epsilon = \frac{R_{vap}}{R_{dry}} - 1 \ , \tag{2.19}$$

where the constant R_{vap}, that is equal to 461.51 J kg^{-1}K^{-1}, denotes the specific gas constant of water vapor [25].

By differentiating Equation (2.2), Equation (2.16) may be rewritten as [25]

$$\mathrm{d}\Phi = -\frac{R_{dry}T}{p}\mathrm{d}p \ . \tag{2.20}$$

Considering Equation (2.3), Equation (2.20) may in turn be rewritten as

$$dZ_g^{msl}g_0 = -\frac{R_{dry}T}{p}\mathrm{d}p \ . \tag{2.21}$$

In order to analytically solve the differential Equation (2.21), some useful simplifications for the temperature evolution with altitude are given by the ISA model [13, 24]. In

particular, the ISA divides Earth's atmosphere in 8 layers of different ranges of geopotential altitude AMSL, from -5 to 80 km [24].

As in the present work, only the geopotential altitude AMSL range between 0 and 20 km is relevant, the equations for evolution of temperature with altitude will be given herein only for the two layers comprised in this range:

$$T_{ISA} = T_0 - \alpha Z_g^{msl} \quad , \qquad\qquad 0 < Z_g^{msl} \leq 11 \text{ km} \;\; ;$$

$$T_{ISA} = T_1 \qquad\qquad , \qquad\qquad 11 \leq Z_g^{msl} < 20 \text{ km} \;\; , \tag{2.22}$$

where the values of α, known as the temperature lapse rate, and of T_1 are given in Table 2.2.

Inserting this model into Equation (2.21) yields

$$dZ_g^{msl} g_0 = -\frac{R_{dry}(T_0 - \alpha Z_g^{msl})}{p} \mathrm{d}p \quad , \qquad\qquad 0 < Z_g^{msl} \leq 11 \text{ km} \;\; ;$$

$$dZ_g^{msl} g_0 = -\frac{R_{dry} T_1}{p} \mathrm{d}p \qquad\qquad , \qquad\qquad 11 \leq Z_g^{msl} < 20 \text{ km} \;\; . \tag{2.23}$$

Finally, integrating along Z_g^{msl} from a certain reference geopotential altitude AMSL, $Z_{g,ref}^{\mathrm{msl}}$, both expressions of Equation (2.23) results in

$$Z_g^{msl} = \frac{T_{ref}}{\alpha} \left[1 - \left(\frac{p}{p_{ref}} \right)^{\frac{kR_{dry}}{g_0}} \right] + Z_{g,ref}^{msl} \qquad , \qquad 0 < Z_g^{msl} \leq 11 \text{ km} \;\; ;$$

$$Z_g^{msl} = 11 \text{km} - \frac{T_{11km} R_{dry}}{g_0} \ln \left(\frac{p}{p_{11km}} \right) \quad , \qquad\qquad 11 \leq Z_g^{msl} < 20 \text{ km} \;\; , \tag{2.24}$$

where T_{ref} and p_{ref} denote the temperature and pressure at $Z_{g,ref}^{\mathrm{msl}}$, respectively, while T_{11km} and p_{11km} denote the temperature and pressure at 11 km of geopotential altitude AMSL.

2.2.2 Barometric Altimeters, Standard Pressure Altitude and Flight Levels

In aviation, barometric altimeters are used to convert static air pressure measurements, $\tilde{p}$, into altitude information, based on the first of the two expressions of Equation (2.24). More in detail, this altitude information is called standard pressure (or barometric) altitude, which is denoted by $Z_{\mathrm{p,std}}$ when the reference is the ISA standard MSL. This means that $Z_{g,ref}^{\mathrm{msl}} = 0$, $T_{\mathrm{ref}} = T_0$ and $p_{\mathrm{ref}} = p_0$, resulting in [26]

$$Z_{p,std} = \frac{T_0}{\alpha} \left[1 - \left(\frac{\tilde{p}}{p_0} \right)^{\frac{kR_{dry}}{g_0}} \right] \;\; . \tag{2.25}$$

Therefore, standard pressure altitude represents an estimate for the altitude above the p_0 isobar surface [26] and the more the actual values of pressure and temperature at MSL at the current location deviate from their corresponding ISA values, the more $Z_{p,std}$ deviates from the true geopotential altitude AMSL. As a result, significant error when approximating the true altitude AMSL may arise and account for a 10% of the truth [6, 11]. An update version of Table 2.1 including standard pressure altitude is shown in Table 2.3.

		Altitude Scale	
		Geometric	Geopotential
Reference	WGS84	Geodetic altitude h	Geopotential altitude above WGS84 Z_{g}^{wgs84}
	MSL (Geoid)	Orthometric altitude H	Geopotential altitude AMSL Z_{g}^{msl}
	ISA MSL isobar		Standard pressure altitude $Z_{p,std}$

Table 2.3: Different altitude definitions, with pressure altitude

Furthermore, even if the actual MSL values at the current aircraft's horizontal (i.e., latitude-longitude) location for temperature and pressure were to be used instead of the ISA values in the computation of pressure altitude, this would still differ from the true geopotential altitude AMSL. This is due to the inherent approximation of the true atmosphere behavior that the ISA model for temperature introduces. Indeed, in reality temperature does not necessary everywhere decrease from T_0 with altitude in a linear way with the temperature lapse rate α.

The expression "temperature effect" refers to the errors due to the real non-standard temperature evolution with altitude [27]. Physically, these errors stem from the fact that temperature causes a contraction or dilatation of the separation between the isobar surfaces along the vertical.

As a result, when the atmospheric temperature is higher than in the ISA standard atmosphere, barometric altimeters underestimate the true geopotential altitude AMSL, whereas the opposite is true in the case of a warmer-than-ISA atmosphere [26]. The temperature effects in the former case, which are referred to as cold (or low) temperature effects are of course more dangerous when flying at low heights above ground, as they lead the pilot to underestimate the altitude above ground and/or other obstacles [27, 28].

The temperature effect's errors' magnitude is generally reduced when choosing as

reference temperature the actual MSL temperature over its ISA standard corresponding value, T_0. This is due to the fact that this way the modeled temperature evolution with altitude is generally closer to the truth.

This temperature effect's error with respect to the true geopotential altitude AMSL adds up to the difference between the geometric and the geopotential scales when trying to approximate the true orthometric altitude with pressure altitude. This is shown in a qualitative way, i.e., out of scale, in Figure 2.4.

Finally, in the approximation of true altitude, i.e., true geodetic altitude, with pressure altitude, the geoid undulation at the current location adds up to the error. So, in the evaluation of the deviation pf standard pressure altitude from geodetic altitude from e.g., GPS, one needs to consider all these different effects.

Nevertheless, standard pressure altitude is extensively used in aviation in order to enable safe aircraft vertical separation, rather than precise altitude information [9, 26, 29]. Indeed, for two airplanes both using the standard ISA MSL isobar as reference, the only factors that may provide two airplanes with two different standard pressure altitudes are their respective pressure measurement.
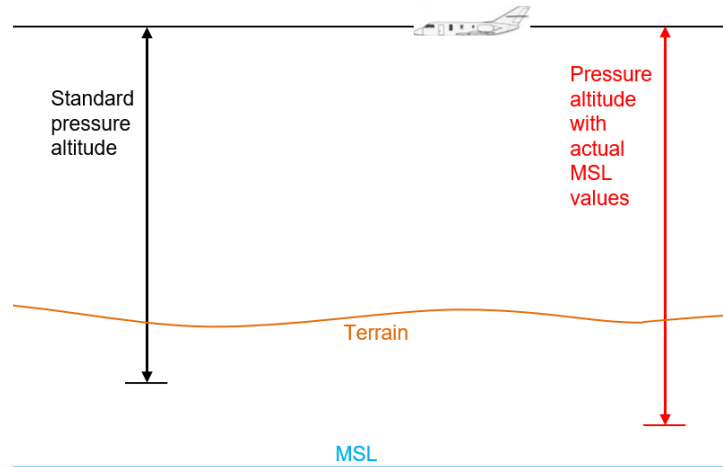

Figure 2.4: Pressure altitude deviation from true altitude AMSL

Flight levels are a concept, strictly connected to pressure altitude, used to ensure safe vertical separation in a straightforward way. A flight level is defined as a surface of constant barometric pressure which is related to the ISA standard MSL pressure, p_0, and is separated from other such surfaces by specific pressure intervals [2, 24]. A flight level indicates therefore a pressure, rather than an altitude. Each flight level is stated with the letters "FL" followed by three digits that represent hundreds of feet, while being a multiple of 500 ft. As an example, FL 350 represents a barometric altimeter indicating 35000 ft [2].

Flight regulation authorities command a switch from flight-level-based guidance (i.e., standard-pressure-altitude-based), to an altitude-AMSL-based one when flying above a certain transition altitude. This has different values, depending on the country and/or

airport [30, 31, 32]. In northern America, for example, the transition altitude is 18000 ft (5486 m) [30, 33]. An indication of altitude AMSL through barometric altimeters is possible through a correction, sometimes referred to as "baro-correction" [26], which is the focus of Section 2.3.

The transition level is the lowest FL available for use above the transition altitude and it also depends on the county and/or airports and/or the pressure measured at the airport or base station. Only above the transition level, altitude information is given in terms of flight levels [1].

The relationships between true orthometric altitude, the ISA standard MSL isobar, and other isobars corresponding to given flight levels are shown in Figure 2.5, which depicts aircrafts flying at different flight levels (out of scale). This figure also shows that flight levels surfaces, i.e., isobar surfaces, are necessarily parallel to the MSL surface.
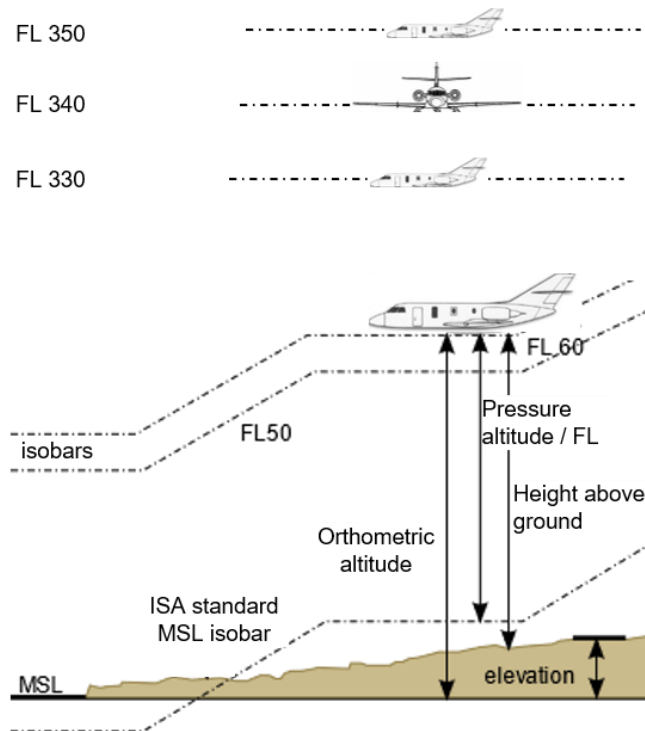

Figure 2.5: Flight levels (based on the figure given in [34])

2.3   Corrected Pressure Altitude

In Section 2.3.1, a correction procedure for increasing pressure altitude's accuracy in approximating true orthometric altitude or true altitude above ground is presented. This procedure, which actually consists in two different sub-options, is sometimes referred to as "baro-correction" [26].

Section 2.3.2 discusses some procedures for compensating temperature effects, which were introduced in Section 2.2.2.

2.3.1 Baro-corrected Pressure Altitude

There are two different options for a baro-correction of standard pressure altitude, which are typically performed in aviation [2, 24, 26]. The correction ΔZ_c provided in both cases is computed as

$$\Delta Z_c = \frac{T_0}{\alpha}\left[1 - \left(\frac{BC_c}{p_0}\right)^{\frac{kR_{dry}}{g_0}}\right] \tag{2.26}$$

and is subtracted from the standard pressure altitude to yield the baro-corrected pressure altitude, $Z_{p,c}$ [26]:

$$Z_{p,c} = Z_{p,std} - \Delta Z_c \tag{2.27}$$

The baro-correction in the pressure domain, BC_c, may be of the "QNH" or "QFE" kind [26]. In the former case, the subscript c in Equations (2.26) and (2.27) is substituted by the subscript QNH, in the latter by QFE.

The QNH correction applied on a barometric altimeters on an aircraft will cause the barometric altimeter to read the reference airport's (or another kind of base's) altitude AMSL when the aircraft is on the runway [3, 26]. Therefore, in the nearness of the airport, the QNH corrected pressure altitude, $Z_{p,QNH}$, approximates to a higher level of accuracy the true orthometric altitude than the standard pressure altitude does. The QNH correction in pressure domain, i.e., BC_{QNH}, which evolves with time for a given airport, is sent regularly within the METAR transmission from the airport to the airplanes in the surroundings [35].

The difference between QNH correction and the QFE one, is that when the latter is applied on a barometric altimeters on an aircraft on the reference airport's runway, this will lead the barometric altimeter to read zero altitude. Therefore, in the nearness of the airport, the QFE corrected pressure altitude, $Z_{p,QFE}$, provide an approximation of the altitude above ground [3].

As anticipated in Section 2.2.2, below the transition altitude, flight management authorities command to shift from the standard pressure altitude (or Flight level, see Section 2.2.2) to a baro-corrected one [5, 36]. This is done in order to still maintain vertical separation between airplanes in the surroundings—the same correction is applied to all airplanes—while ensuring a better estimation of the distance from the ground. More in detail, the baro-correction is in most cases of the QNH kind, although in some countries and/or airports aircraft vicinity operation are performed based on the QFE approach [37, 38].

The QNH and QFE baro-correction are also referred to as QNH and QFE altimeter (pressure) settings, whereas the setting providing standard pressure altitude is also known as QNE altimeter setting [3, 5, 36].

Figure 2.6 integrates the concepts depicted in Figure 2.4 by additionally illustrating in a qualitative way (i.e., out of scale) the relationships between the various aforementioned pressure-altitude related concepts. It shall be noted that, unlike they are repre-

sented in Figure 2.6, the various pressure-altitude-related altitudes may also overestimate the true altitude above MSL (or above the runway). This depends on the actual atmospheric pressure and temperature values at MSL (or at the runway) and on their evolution with altitude.

The BC_{QNH} sent by an airport is obtained by projecting the BC_{QFE} to sea level according to ISA and therefore regardless of the real temperature structure of the atmosphere [3, 26]. Since barometric altimeters use ISA, they will indicate orthometric altitude correctly at the airport, and more in particular at the airport's point that was set as the reference for the BC_{QNH} computation. At other altitudes, but on the same latitude-longitude location, the indicated altitude is most likely to be erroneous, depending on the real temperature of the atmosphere [3].

Therefore, depending on the vicinity of the aircraft to the airport on the horizontal plane and in the vertical channel and also on the spatial changes in atmospheric pressure and temperature, QNH-corrected may be more or less accurate in approximating true orthometric altitude than pressure altitude computed with actual MSL values. In Figure 2.6, whereby the aircraft is currently at the same airport's latitude-longitude location., QNH-corrected pressure altitude is shown to be more accurate.
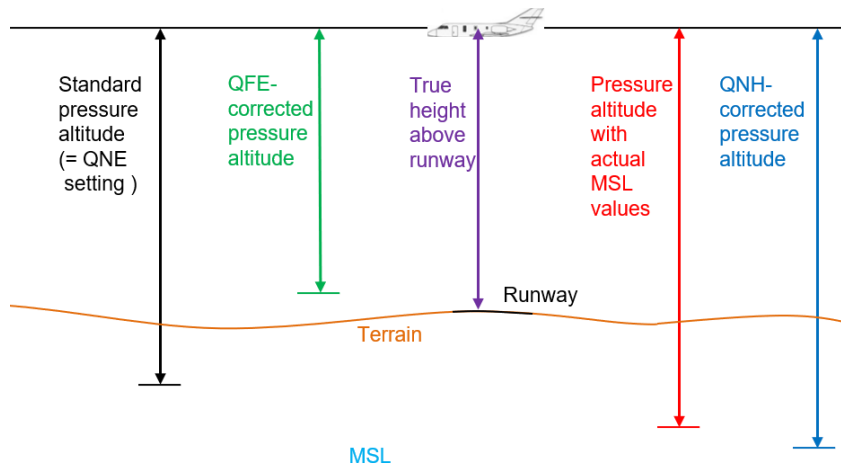

Figure 2.6: Pressure altitude corrections

2.3.2 Temperature Correction for Minimum Safe Altitudes

Minimum Safe Altitude/Height (MSA) is a generic expression adopted in aviation to address an altitude below which it is not safe fly due to the presence of terrain or other obstacles [39].

In [5], different methods for providing corrections for temperature effects, introduced in Section 2.2.2, are briefly presented. In particular, these methods are meant for adjusting MSA when the ambient temperature on the surface is "much lower" than that predicted by the ISA.

For example, for temperatures above -15°C, an approximate correction is the 4% height increase for every 10°C below that one predicted by the ISA at the altimeter set-

ting source, be it the MSL for QNE/QNH or the airport for QFE. Other corrections for cold temperature effects are tabulated in altitude-temperature grids [5].

Since these corrections do not have the goal of increasing pressure altitude's accuracy in approximating true altitude AMSL, rather to enable safe vertical separation from obstacles in a conservative way, their analysis is not in the scope of this work.

They have been briefly mentioned in the current section for the sake of completeness, since, along with the baro-corrections, these are the altimeter corrections the pilot is responsible for [5].

2.4   Blanchard Altitude

The Blanchard algorithm is an additional way of compensating for non-standard atmosphere when obtaining altitude information from pressure measurements. Anyway, unlike the corrections presented in 2.3, the measurements of other quantities are needed apart from pressure.

The Blanchard algorithm provides altitude information through the numerical integration of an equation resulting from the addition to Equation (2.16) of a correction term accounting for the wind influence [7, 11]. This equation is

$$dH = -\frac{R_{dry}T}{gp}dp + \frac{V_g V_{wc}}{g}2\Omega \sin L \ dt \ , \tag{2.28}$$

where dt is the infinitesimal time interval during which an object performs the infinitesimal altitude variation dH, by keeping a velocity along the ground of modulus V_g [7]. The latter quantity is also known as groundspeed. In Equation (2.28), V_{wc} denotes the component of wind velocity perpendicular to the ground track and it is positive when the wind is from the right with respect to the direction of the velocity along the ground [7]. This quantity is referred to as cross-wind speed [11]. Finally, Ω denotes the Earth's rotation rate, in terms of rad/s.

In particular, the Blanchard algorithm consists in the solution of Equation (2.28) by trapezoidal integration [11, 29]:

$$
\begin{aligned}
H_{B,i} = H_{B,i-1} &- \frac{R}{2}\left(\frac{\tilde{T}_i}{g_i\tilde{p}_i} + \frac{\tilde{T}_{i-1}}{g_{i-1}\tilde{p}_{i-1}}\right)(\tilde{p}_i - \tilde{p}_{i-1}) \ + \\
&+ \Omega\left(\frac{\tilde{V}_{g,i}\tilde{V}_{wc,i}\sin L_i}{g_i} + \frac{\tilde{V}_{g,i-1}\tilde{V}_{wc,i-1}\sin L_{i-1}}{g_{i-1}}\right)(t_i - t_{i-1}) \ ,
\end{aligned}
\tag{2.29}
$$

where $\tilde{p}_i$, $\tilde{T}_i$, $\tilde{V}_{g,i}$ and $\tilde{V}_{wc,i}$ denote the pressure, temperature, groundspeed, and cross-wind speed measurements, respectively at the i-th iteration. The remaining terms, i.e. g_i, L_i and t_i are the local gravity acceleration approximation, the latitude estimate and the time at the same iteration, respectively.

Since an approximation for the gravity acceleration is computed at each step as a function of altitude and latitude, and it is not assumed to be constant and equal to its standard MSL value—as it is done in the pressure altitude equation instead—the output of Blanchard's algorithm is an orthometric altitude. For this reason, this altitude, which is referred to as Blanchard altitude [11, 12, 13] is herein denoted with the capital "h", in accordance with the nomenclature introduced in Section 2.1. Additionally, the subscript "B" is used to denote the Blanchard algorithm.

In particular, the local gravity acceleration at the i-th iteration is computed from the Blanchard altitude at the previous iteration, i.e., at the (i-1)-th iteration, and the latitude estimate at the i-th iteration as [6, 11]

$$g_i = g_A + g_B \sin^2 L_{i-1} + g_C H_{B,i-1} \ . \tag{2.30}$$

In Equation (2.30), g_A = 9.780250907 m s^{-2}, g_B = 0.051799217 m s^{-2} and g_C = $-$3.0877321$\cdot$10^{-6} s^{-2}.

Given the fact that Blanchard altitude is based on a recursive algorithm, it needs to be initialized. Since it is an orthometric altitude, the initial altitude should correspond to the base orthometric altitude, e.g., the take-off airport's altitude AMSL, as it was done in [11].

As it is likely to be the case, measurements about the wind perfomed by aircraft Air Data Systems (ADS), are expressed in terms of the modulus of the wind velocity and its direction with respect to the north. From this information, the east and north components of the wind velocity, v_{wE} and v_{wN} may be easily computed [40]. These wind components, in turn, may be used to calculate the product between groundspeed and cross wind speed—which appears in the Blanchard algorithm—in alternative way as

$$V_g V_{wc} = -v_{aN} v_{wE} + v_{aE} v_{wN} \ , \tag{2.31}$$

where v_{aN} and v_{aE} denote the east and north components of the aircraft velocity [11].

The limitations of this algorithm are two. The first stems from the fact that it requires an initialization, so the output degrades with the time passed and the horizontal distance covered after the initialization.

The second limitation consists in the fact that the first term of algorithm requires pressure variations $(\tilde{p}_i - \tilde{p}_{i-1})$ to take the effects of the temperature variations into account. This means that from this first term no correction can be computed when the aircraft is at constant barometric altitude such as in cruise flight, i.e., when it flies on a given flight level [26].

3 State of the Art of Pressure Altitude Integration in Navigation Algorithms

3.1 Integrated Flight Level Guidance

Standard pressure altitude has been traditionally used in third-order control loops to damp the inherent instability of the vertical channel of Inertial Navigation Systems (INS) [6, 26, 29], also called Inertial Reference systems (IRS). Such a control loop, in which the gains are chosen based on tuning, is exemplarily shown in Figure 3.1. It shall be noted that in such control loops, the input to the loop from the barometric altimeter is the standard pressure altitude and not a corrected one [26].
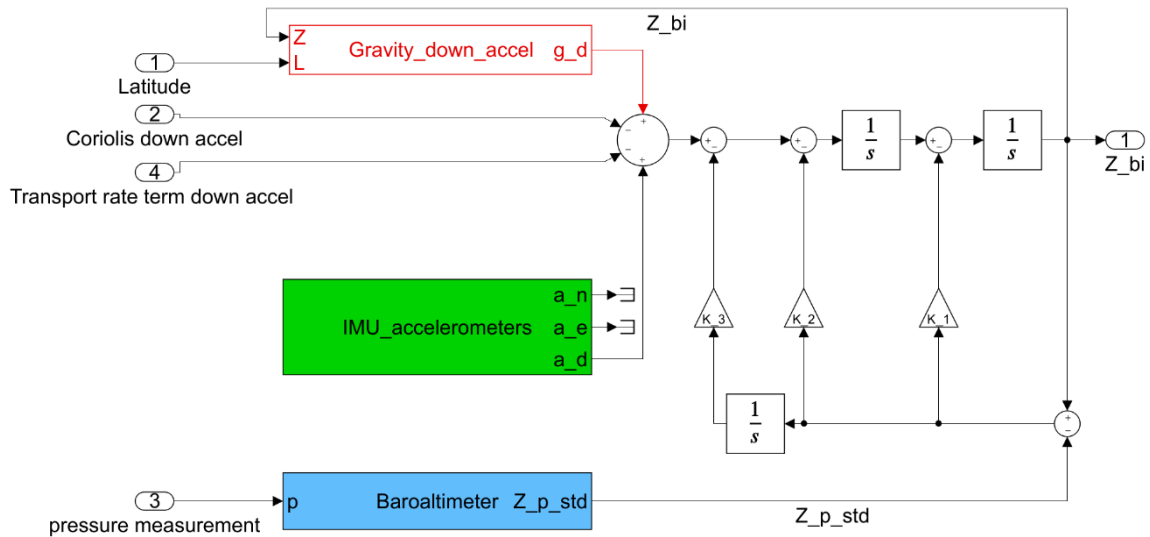
Figure 3.1: 3$^{\mathrm{rd}}$ order control loop for baro-inertial altitude computation [26]

The damped inertial altitude is in this case referred to as baro-inertial altitude and, as the standard pressure altitude, it is referenced to a surface related to air, i.e., the standard MSL isobar surface. As such, it is not referenced to a surface related to the Earth, e.g., the geoid or a reference ellipsoid [26].

This loop's output is therefore strictly related to the concept of flight level guidance, as discussed in Section 2.2.2.

29

Since this thesis focuses on geodetic altitude information from pressure measurements, and not on traditional flight level guidance, integration options as the one illustrated by Figure 3.1 are not in the scope of this thesis.

3.2 Integrated Geodetic Altitude Navigation

Work related to the translation of barometric pressure altitude to geodetic altitude within integrated navigation algorithms can be found in the literature.

In [14], the geoid undulation at the current location is added to the pressure altitude before using this within a GPS least-square estimator to provide 3D positioning. The approach was applied in an urban environment, for a relatively short time. It is not specified aboard what vehicle or person the navigation unit was installed. Most likely, low altitudes have been here considered a valid reason to neglect the difference in altitude scale between pressure and GPS altitudes.

A snapshot algorithm coupling baro-altimeter and DME is considered in [16]. The results presented by the authors are based on simulations and not on data gathered during actual flight tests. Furthermore, it is not stated what leads the author to choose a specific value for the standard deviation of the barometric altimeter's errors. Finally, it is not declared whether the barometric altimeter measurements originate are standard or corrected pressure altitudes.

Similarly, in [9] the author provides a model for the integration of standard pressure altitude measurements within multi-sensor KF-based navigation systems. In particular, both a bias and a scale factor term due to uncorrected reference pressures and uncorrected sensors are incorporated as augmented states. Anyway, the system models of these augmented states are not declared. It neither is stated whether this measurement model would be suitable for corrected pressure altitude measurements.

The integration of a barometric altimeter with INS and INS&GNSS with various KF-based estimators has been simulated in [41], whereby the simulation scenario has not been precisely declared. Furthermore, the values of the parameters, e.g., system noise and measurement noise variances are not stated either.

The measurement model used in that work for the barometric altimeter features a bias with a first-order Gauss-Markov Process structure. This bias is incorporated in the states vector as an augmented state (see Appendix C). Finally, it is not declared whether barometric altimeter's output is the standard pressure altitude or a corrected pressure altitude.

In [15], an adaptive data fusion algorithm is proposed for the integration of a barometric altimeter with GPS, whereby the errors between the barometric altimeter's output and the true altitude are assumed to be normally distributed.

Unlike in [41], in [15], the barometric altimeters outputs are computed via the pressure altitude equation with different references, depending on the simulation case. In

one simulation case, the ISA standard MSL values are used as references. In the second simulation case, constantly changing pressure and temperature values are used as references.

The simulation scenario is the variation of an aircraft's altitude from 10894 m to the sea level approximately. The true altitude is assumed to coincide here to the (standard) pressure altitude in both simulation cases, while the barometric altimeters output and also the GPS altitude output are both assumed to deviate from the truth in a normally distributed way. This means that the geoid undulations and the difference between geometric and geopotential altitude are neglected.

In [15], finally, the (integer) values assumed for measurement noise variances for the GPS and the baroaltimeter altitude measurements are backed neither by error modeling procedures, nor by referencing other sources.

A confidence model for barometric altimeters is described in [42]. The authors define the barometric altimeter's error as the difference between true altitude and pressure altitude. The pressure altitude is computed using as references the pressures and temperatures recorded by meteorological stations. In [42], when computing the baroaltimeter's errors, in the cases in which the true altitude is given by GPS, the geoid undulations are compensated for, whereas the difference between the two altitude scales are not.

The authors then compute what would be the barometric altimeter's error at a specific location when computing altitude by using as references the meteorological data of a stations lying up to several hundreds of kilometers away.

The confidence model consists in a linear model between the standard deviation of barometric altimeter's errors and the distance from the stations.

In the simulation within [42], the standard deviation provided by the model relative to a barometric altimeter measurement at a given distance from a given station is then used as the confidence level for the baroaltimeter within a WAAS (Wide Area Augmentation System) estimation algorithm. In this, the baroaltimeter is treated as a virtual satellite with a known clock bias and located directly overhead at the user's location.

Time-correlated error sources are therefore not covered by this model. Also, the pressure measurements assumed in this work could be much different from the ones measured aboard an aircraft, which may be corrupted by flight dynamics effect, among others.

In [43] vertical protection levels for UAVs (Unmanned Aerial Vehicles) using GPS and baroaltimeters is proposed. Using experimental data, a statistical error bound of a barometric altimeter's measurement is defined. This error bound is then used within a WLS (weighted least square) RAIM for the baroaltimeter's integration with GPS.

The barometric altimeter's output was computed with the pressure altitude equation, using as references the pressure and temperature provided by the nearest weather station. More in detail the measurements were performed by keeping the measuring unit at a constant orthometric altitude of approximately 100 m, for 18 hours. The baroaltimeter's error is in that work bounded by a normal distribution.

It is highlighted that using as references the aforementioned weather data provided a

great improvement in the baroaltimeter's accuracy at estimating the true orthometric altitude. By deriving the overbounding model the difference between the geopotential and the geometric scales was not considered, probably because of the considerably low altitude AMSL.

Recapitulating, in the available literature, the differences between the altitude references together with the differences in the scales are rarely considered simultaneously. Moreover, the KF parameters used to model the barometric measurements are rarely mentioned and one assumes that traditional tuning approaches are followed. Additionally, simulations are often considered, which means that realistic errors are not necessarily always portrayed.

Finally, the available literature generally addresses the modeling of standard pressure altitude or pressure altitude. When corrected pressure altitude is considered, the corrections are not performed based on an interpolation of multi-level weather data, as it is instead done in this thesis, as will be described in Section 4.1.

This work aims at covering the empty spaces left by the available literature in this field. This is done by, first, assessing the accuracy of two different methods to obtain geodetic altitude from pressure measurements aboard an aircraft and, secondly, by seeking the corresponding error models. The latter ones have to be properly determined, quantified, and bounded, so that the integrity of the vertical channel estimation can be guaranteed and safe vertical navigation ensured.

4 Geodetic Altitude from Pressure Measurements

This chapter is devoted to the description of the procedures employed for the computation of accurate geodetic altitude from the available test flights' data, potentially combined with external weather data.

In this work, two methods for obtaining altitude information from, among others, pressure measurements are employed. In particular these two methods are applied to the central portions (see Section 5.2) of the nine test flights presented in Section 5.

In the first method, at any flight trajectories' point, a so-called weather-corrected pressure altitude is computed from the pressure measurements and weather data on isobar surfaces provided by the European Union's Copernicus Programme [17]. This is a geopotential altitude referenced to the MSL, which means that in order to obtain a geodetic altitude, a shift in reference must be accompanied by a scale conversion. This is shown in Figure 4.1 with a blue arrow.
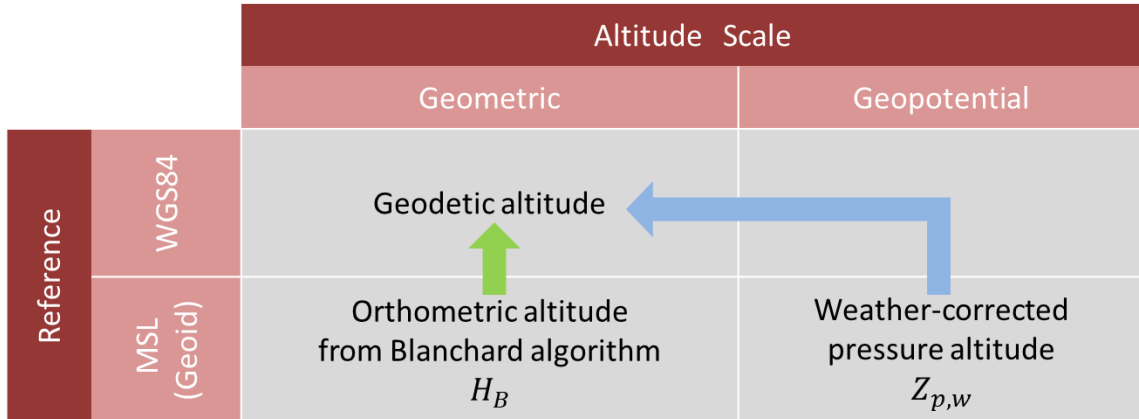
Figure 4.1: Altitudes Scheme

In the second method, described in Section 4.2, pressure, temperature, and aircraft's and wind velocity measurements are used at each trajectory's point to produce altitude information via the Blanchard algorithm.

Since the output of this algorithm is an orthometric altitude profile, i.e., a geometric altitude AMSL, geoid undulations along the trajectory need to be added to it to provide a geodetic altitude profile. This corresponds to shifting the reference from the MSL to

the reference ellipsoid, as it is shown in Figure 4.1 with a green arrow.

These two methods are schematically and yet more in detail depicted in Figure 4.2, where the computation of standard pressure altitude is also shown. The color code for the arrows is the same as in Figure 4.1.
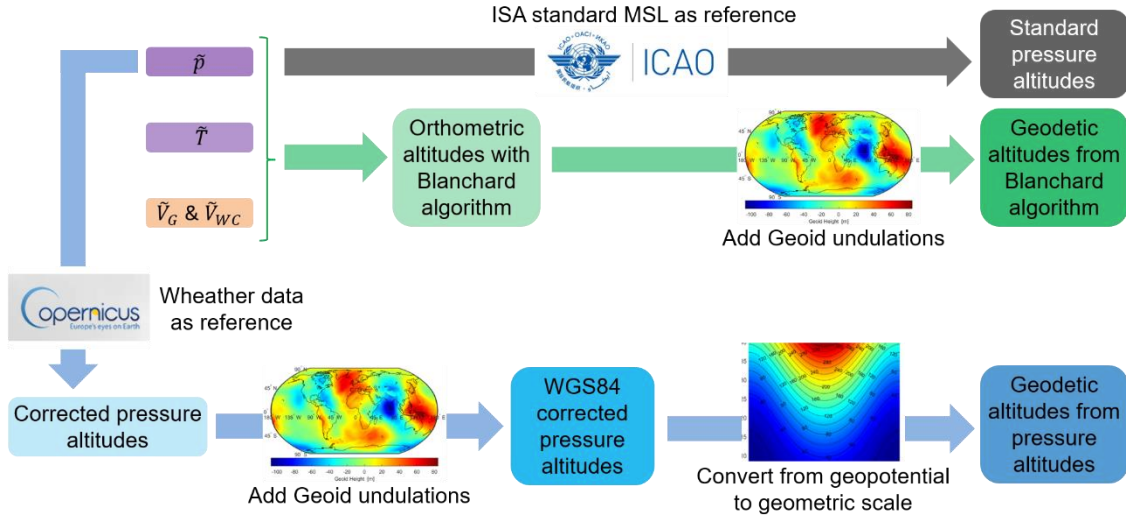
Figure 4.2: Methodology for computing geodetic altitudes from FMS measurements and weather data

4.1 Geodetic Altitude from ERA5 Weather-corrected Pressure Altitude

4.1.1 Weather-corrected Pressure Altitude

In this work, the phrase "weather-corrected pressure altitude" is used to refer to the aircraft's pressure altitude which can be obtained by entering into Equation (2.24)—as the reference values—the actual pressure and temperature at the aircraft's horizontal location and at the geopotential altitude AMSL they are referred to.

In particular, when the aircraft is estimated to be flying below 11 km of geopotential altitude AMSL, the second of the two expressions of Equation (2.24) is used and the actual pressure and temperature values at 11 km are used.

Equation (2.24) is repeated here with some slight formal changes in order to highlight the outputs and inputs of the correction procedure explained in the previous paragraphs of this section:

$$Z_{p,w} = \frac{T_{ref}}{\alpha} \left[1 - \left(\frac{\tilde{p}}{p_{ref}} \right)^{\frac{kR_{dry}}{g_0}} \right] + Z_{g,ref}^{msl} \quad , \qquad 0 < \hat{Z}_g^{msl} \le 11 \text{ km} \ ;$$

$$(4.1)$$

$$Z_{p,w} = 11\text{km} \ - \frac{T_{11km} R_{dry}}{g_0} \ln \left(\frac{\tilde{p}}{p_{11km}} \right) \quad , \qquad 11 \le \hat{Z}_g^{msl} < 20 \text{ km} \ ,$$

where $Z_{\text{p,w}}$ denotes the weather-corrected pressure altitude, $\tilde{p}$ is the airborne barometer pressure measurement, and $\hat{Z}_g^{msl}$ denotes the aircraft's estimated geopotential altitude AMSL.

That this pressure altitude computation is weather-corrected partially means that when $Z_{\text{p,w}}$ is used to approximate the aircraft's orthometric altitude, it does not show the errors that $Z_{\text{p,std}}$ shows due to the fact that is referenced to an isobar (the ISA MSL isobar) which can be relatively much detached from the MSL.

The further meaning of the "weather-corrected" attribute, is that the errors' magnitudes due to the temperature effect, introduced in Section 2.2.2, are reduced. Indeed, the Section 2.2.2 's example of using the actual MSL values as references during a flight is a special case of weather-corrected pressure altitude.

The actual weather quantities' values (or at least good estimates thereof) which may be used as references may for example be obtained from numerical weather predictions (NWP) or climate (also referred to as atmospheric or weather) reanalysis.

More in detail, weather data may be provided on global or local latitude-longitude grids and on various vertical levels. An interpolation between these grid points and potentially also between the levels may then be used to extract the estimates of the needed pressure and temperature values at the aircraft's horizontal locations and/or altitude or at 11 km.

Indeed, an interpolation of weather data is actually of crucial importance in the methodology of this work and is therefore presented in detail in Section 4.1.2.

A further correction may be achieved by considering the effects of humidity in pressure altitude computation. In order to take humidity into account, being this another weather quantity that may be obtained from NWP or climate reanalysis, one may refer to Equations from (2.17) to (2.19).

Just as Equation (2.24) is obtained from the differential Equation (2.16) by analytically solving it based on the ISA model for temperature, the following equation is obtained from Equation (2.17):

$$Z_g^{msl} = \frac{T_{V,ref}}{\alpha} \left[1 - \left(\frac{p}{p_{ref}} \right)^{\frac{kR_{dry}}{g_0}} \right] + Z_{g,ref}^{msl} \quad , \qquad 0 < Z_g^{msl} \le 11 \text{ km} \ ;$$

$$(4.2)$$

$$Z_g^{msl} = 11\text{km} \ - \frac{T_{V,11km} R_{dry}}{g_0} \ln \left(\frac{p}{p_{11km}} \right) \quad , \qquad 11 \le Z_g^{msl} < 20 \text{ km} \ .$$

The virtual temperature at the given reference altitude and at 11 km, $T_{V,\mathrm{ref}}$ and $T_{V,11\mathrm{km}}$, respectively, that appear in Equation (4.2), are obtained from T_{ref} and $T_{11\mathrm{km}}$, according to Equations (2.18) and (2.19).

In the same fashion Equation (2.24) has been rewritten as Equation (4.1), Equation (4.2) may be finally rewritten as

$$
Z_{p,w,h} = \frac{T_{V,ref}}{\alpha}\left[1 - \left(\frac{\tilde{p}}{p_{ref}}\right)^{\frac{kR_{dry}}{g_0}}\right] + Z_{g,ref}^{msl} \quad , \qquad 0 < \hat{Z}_g^{msl} \le 11 \text{ km } ;
$$

$$
Z_{p,w,h} = 11\mathrm{km} \ -\frac{T_{V,11km}R_{dry}}{g_0}\ln\left(\frac{\tilde{p}}{p_{11km}}\right) \quad , \qquad 11 \le \hat{Z}_g^{msl} < 20 \text{ km } ,
$$

(4.3)

whereby $Z_{p,w,h}$ denotes the weather-and-humidity-corrected pressure altitude.

4.1.2 Weather-correction with Interpolated Weather Data

Weather-corrected pressure altitude $Z_{p,w}$ is computed by inserting, as references, in the first expression of Equation (4.1) the pressure and temperature provided by weather data at the aircraft's latitude, longitude, and geopotential altitude AMSL. Additionally, weather-corrected pressure altitude at geopotential altitudes AMSL higher than 11 km, is computed with the second expression in Equation (4.1). In this second expression, the pressure and temperature provided by weather data at 11 km of geopotential altitude AMSL are needed.

In this work, weather data is obtained from Copernicus, the European Union's Earth observation programme, which provides various climate datasets. These are managed by the European Centre for Medium-Range Weather Forecasts (ECMWF) within the context of the Copernicus Climate Change Service (C3S).

In particular, weather data is extracted from the ECMWF ERA5 climate reanalysis on pressure levels. This provides data for numerous atmospheric quantities on 37 pressure levels from 1000 to 1 hPa, i.e., on isobar surfaces. Data is given at each UTC full hour since 12:00 a.m. of January 1, 1979, on a global regular latitude-longitude grid having a 0.25° resolution [17]. Figure 4.3 summarizes this in a schematic way.

This climate dataset can be therefore visualized as a four-dimensional (4D) grid. For each of the points of this 4D grid, among the various quantities, the temperature, the geopotential altitude AMSL and the specific humidity are reported.

In order to obtain the temperature and pressure at the current aircraft's location, multidimensional interpolation of the ERA5 data is necessary. In the present work it was performed with the true trajectory profile, being this obtained from the available test flight's data, as described in Section 5.1.
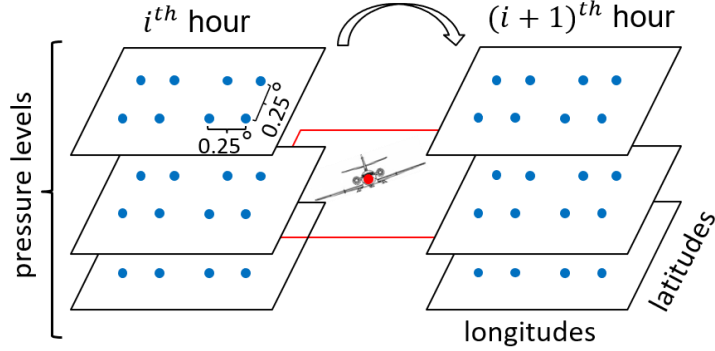
Figure 4.3: ERA5 weather data structure scheme and the aircraft's position at a certain location and time

The interpolation is performed linearly in the horizontal plane and in time, whereas there is a distinction for the interpolation along the vertical. Indeed, the interpolation is done linearly for temperature, whereas it is performed linearly in the logarithm of pressure, since it is known that pressure decreases approximately exponentially with increasing altitude [25, 44].

It was observed that, for the flight trajectories considered in this work (see Section 5.1), it was enough to consider only the 23 lowest pressure levels, i.e. the 23 pressure levels whose corresponding isobar surfaces are closer to the MSL surface. These levels range from 1000 to 200 hPa and the difference between adjacent levels is constant and equal to 25 hPa. Only below 100 hPa, the spacing between consecutive levels is not constant anymore and actually decreases progressively.

More in detail, at any flight trajectory' instant, the temperature and the geopotential altitude AMSL of each isobar are linearly interpolated to the trajectory's horizontal position and UTC time. This results in a two-dimensional (2D) matrix, both for temperature and for geopotential altitude AMSL, in which one dimension's length is equal to the number of trajectory time instants and the other dimension's length is 23.

For the interpolation in the horizontal plane, the latitude and longitude referenced to the WGS84 ellipsoid, have to be used. Indeed, as already mentioned in Section 2.1, in the horizontal plane, the ERA5 weather data is referenced with respect to the WGS84 [11, 12].

Regarding the details of the interpolation in the vertical channel, at any flight trajectory' instant, the above mentioned 2D temperature matrix, whose corresponding geopotential altitudes AMSL are contained in the other aforementioned 2D matrix, is linearly interpolated to the aircraft's geopotential altitude AMSL. This yields T_{ref}.

Since the second expression of Equation (4.1) requires pressure and temperature at $Z_{\mathrm{g}}^{\mathrm{msl}} = 11$ km, temperature is also interpolated to $Z_{\mathrm{g}}^{\mathrm{msl}} = 11$ km, yielding $T_{11\mathrm{km}}$.

Moreover, the natural logarithms of the 23 isobars' pressures, through the matrix of the geopotential altitudes AMSL, are linearly interpolated to the current aircraft's geopotential altitude AMSL. By evaluating the exponential function, with the base being Euler's number, the pressure at the current aircraft's position, i.e., p_{ref}, is

obtained. Similarly to what was said in the previous paragraphs about $T_{11\text{km}}$, pressure is also logarithmically interpolated to $Z_g^{\text{msl}} = 11$ km, yielding $p_{11\text{km}}$.

The interpolations are all performed with the MATLAB® function interpn.

It shall be noticed that the aircraft's geopotential altitude AMSL used for the interpolation is computed applying Equations (2.12) and (2.13). The geoid undulations are obtained from the EGM96 model, which provides data with a raster at a 15'×15' (latitude × longitude) resolution, through the MATLAB® function geoidheight. Although this function also allows to obtain geoid undulations from the newer and more accurate EGM2008 model, which has a higher resolution (2.5'×2.5') with respect to the EGM96, the EGM96 is chosen. This choice is due to the fact that the ERA5 data [17] is referenced in the vertical channel to the EGM96 Geoid [18].

With this interpolated weather data and pressure measurement, as said in the beginning of this section, Equation (4.1) yields an altitude $Z_{p,w}$ whose scale and reference are the geopotential one and the MSL, respectively.

To convert this altitude to a geodetic altitude two steps are necessary: one for the scale conversion and one for the reference shift.

First, Equation (2.13) should be reverted to obtain Z_g^{wgs84}. Secondly, this should be entered in Equation (2.12), which should then be reverted to obtain the geodetic altitude h. Anyway, since Equation (2.12) cannot be analytically solved for h, a numerical solution could be used. Since the variation of $Z_g^{wgs84}(L, h)$ with h is relatively small, another option to obtain h from $Z_g^{wgs84}(L, h)$ with a relatively small error but in a fast way could be to analytically compute $Z_g^{wgs84}(L, Z_g^{wgs84})$ with Equation (2.12) and to obtain an approximation h^* of h with

$$h \approx h^* = \left[Z_g^{wgs84} - Z_g^{wgs84}(L, Z_g^{wgs84}) \right] + Z_g^{wgs84} \ . \tag{4.4}$$

This yields satisfactory results because for the altitude ranges considered in this work

$$h - Z_g^{wgs84}(L, h) \approx Z_g^{wgs84} - Z_g^{wgs84}(L, Z_g^{wgs84}) \ . \tag{4.5}$$

Indeed, connsidering a latitude L of 47° and a geodetic altitude h of 11 km, which yield a $Z_g^{wgs84}(L, h)$ of 10.9827 km, and thus a difference $h - Z_g^{wgs84}(L, h)$ of 17.30 m, a difference $Z_g^{wgs84} - Z_g^{wgs84}(L, Z_g^{wgs84})$ of 17.246 m is obtained.

Nevertheless, in the present work, the difference $h - Z_g^{wgs84}(L, h)$ for all trajectories' points was computed from the GPS data and then added to the Z_g^{wgs84} obtained from the weather-corrected pressure altitude to finally obtain a geodetic altitude.

Since this difference is relevant in Section 8.1.2, a function is here introduced to refer to it in a faster way:

$$\Delta_{scale}(L, h) := h - Z_g^{wgs84}(L, h) \ . \tag{4.6}$$

To consider humidity in the pressure altitude computation, one may follow the procedure presented in the previous praragraphs of this section, with the difference of

using Equation (4.3) instead of Equation (4.1), to compuute $Z_{p,w,h}$.

Since Equation (4.3) also features humidity, this option requires to perform the additional step of of interpolating the specific humidity to the aircraft's latitude and longitude and at the aricraft's altitude or at 11 km of geopotential altitude AMSL.

The interpolation of humidity to obtain $q_{11\text{km}}$ and q_{ref}, is done in an analogous way to the interpolation of temperature, as this is described in the previous paragraphs of this section.

It was observed that the consideration of humidity, while increasing the computations' complexity, showed no apparent improvement in approximating the true geodetic altitude. For this reason, this geodetic altitude compuation option is neglected in the next sections of this thesis and was here mentioned for the sake of completeness.

4.2   Geodetic Altitude from Blanchard Altitude

As can be seen from Equation (2.29), in order to compute Blanchard altitude, i.e., orthometric altitude via the Blanchard algorithm, temperature and aircraft's and wind velocity measurements are needed in addition to pressure measurements. As explained in Section 5.1, static air temperature measurements are provided within the available test flight's data.

In order to compute the product $V_g V_{wc}$ within Equation (2.29) at each iteration, Equation (2.31) is used, which means that the north and east components of the aircraft velocity, i.e. v_{aN} and v_{aE}, respectively, need to be known. In this work, these components are obtained from the available test flight's data, as described in Section 5.3.

Apart from the aircraft's north and east velocity components, according to Equation (2.29), also the north and east velocity components of the wind—denoted by v_{wN} and v_{wE}—are needed. Like the aforementioned aircraft's velocity components, in this work, the required wind velocity components are obtained from the test flight's data. This is described in in Section 5.3 too.

Regarding the computation of local gravity within the algorithm according to Equation (2.30), this was based on the latitude values contained in the GPS post-processed data. In a real-time implementation, anyway, the latitude given by the IRS may be used instead, as this is in most cases provided at a higher rate with respect to the latitude from GNSS systems.

The use of measurements from the IRS, that is a navigation subsystem that does not need any external information to function, complies with one of the strengths of the Blanchard's algorithm. This consists in the fact that, unlike the weather-corrected pressure altitude method, the Blanchard algorithm does not need any external information to provide altitude information. Indeed, the quantities that are needed within this algorithm may all be provided by airborne measurements, such as the IRS ones.

The implementation of the Blanchard algorithm which was described in the previous paragraphs of this section is herein referred to as the Blanchard algorithm with FMS data.

A different implementation of the same algorithm is investigated within this work as

well. This is based on the use of the temperatures T_{ref} and pressures p_{ref} which are obtained via the interpolation of the ERA5 weather data. Furthermore, for this peculiar usage of the Blanchard algorithm, the required wind velocity components are obtained from the ERA5 dataset too. Indeed, the ERA5 climate reanalysis provides also the north and east wind velocity components on pressure levels. The interpolation of these quantities is therefore performed analogously to the interpolation of temperature and specific humidity, which is described in Section 4.1. This Blanchard algorithm implementation is herein referred to as the Blanchard algorithm with ERA5 data, in order to distinguish it from the Blanchard algorithm with FMS data.

In the Blanchard algorithm with ERA5 data, humidity can be taken into account too. The consideration of humidity in the Blanchard algorithm consists in a small modification—based on Equations (2.17) and (2.18)—of Equation (2.28) to:

$$ dH = -\frac{R_{dry}T_V}{gp}dp + \frac{V_g V_{wc}}{g}2\Omega \sin L \, dt \; , \tag{4.7} $$

where the virtual temperature T_V replaces the static air temperature T. Practically, this translated to the use of $T_{V,ref}$, which was introduced in Section 4.1.1, instead of T_{ref}.

5 Test Flights Data Preprocessing

Section 5.1 presents the test flights which provided the data this thesis's analyses are based on. In Section 5.2, the focus is on the procedure for reverse-engineering the pressure measurements which were carried out during the flights and used to provide the available pressure altitude data. The steps needed to produce the wind and aircraft's velocity components required by the Blanchard algorithm are described in Section 5.3.

5.1 Test Flights

The nine test flights which were analyzed in the present work were performed with DLR's Dassault Falcon 20-E5 in 2018 between the 9th and the 13th of July. The flights took place mostly in Bavaria, as can be seen in Figure 5.1, in which the trajectories' projections on the Earth's surface are shown for the sake of completeness.

Each flight is given an identifying code with the following format: DDX, where DD is the day of July the flight was performed. Regarding X, this is either "a" or "b", with the former denoting the chronologically first of the potentially two flights of the same day.

The start and end times of each flight are listed in Table 5.1. The geodetic altitude profiles of these flights are shown in Figure 5.2, where each flight is separated by the neighboring flights with black vertical dashed lines. On the x-axis the UTC time of the day each flight took place is shown.

Flight identification code	Start (UTC time)	End (UTC time)	Day
09a	05:59:48	09:20:17	9 July 2018
09b	10:45:35	13:00:43	9 July 2018
10a	05:52:07	07:54:06	10 July 2018
10b	10:14:44	13:16:40	10 July 2018
11a	08:05:56	10:30:21	11 July 2018
12a	05:35:46	08:40:01	12 July 2018
12b	12:20:06	13:48:28	12 July 2018
13a	05:01:09	08:26:51	13 July 2018
13b	10:11:16	12:28:33	13b July 2018

Table 5.1: Flights' durations

The data which was used to generate Figure 5.1 and Figure 5.2 is GPS post-

processed data which was provided by the DLR Flight Experiments (FX) Facility. It contains, among others, the GPS time and the aircraft's position, both in terms of cartesian components in the Earth-Centered-Earth-Fixed (ECEF) frame and in terms of curvilinear coordinates, i.e., latitude, longitude, and (geodetic) altitude.
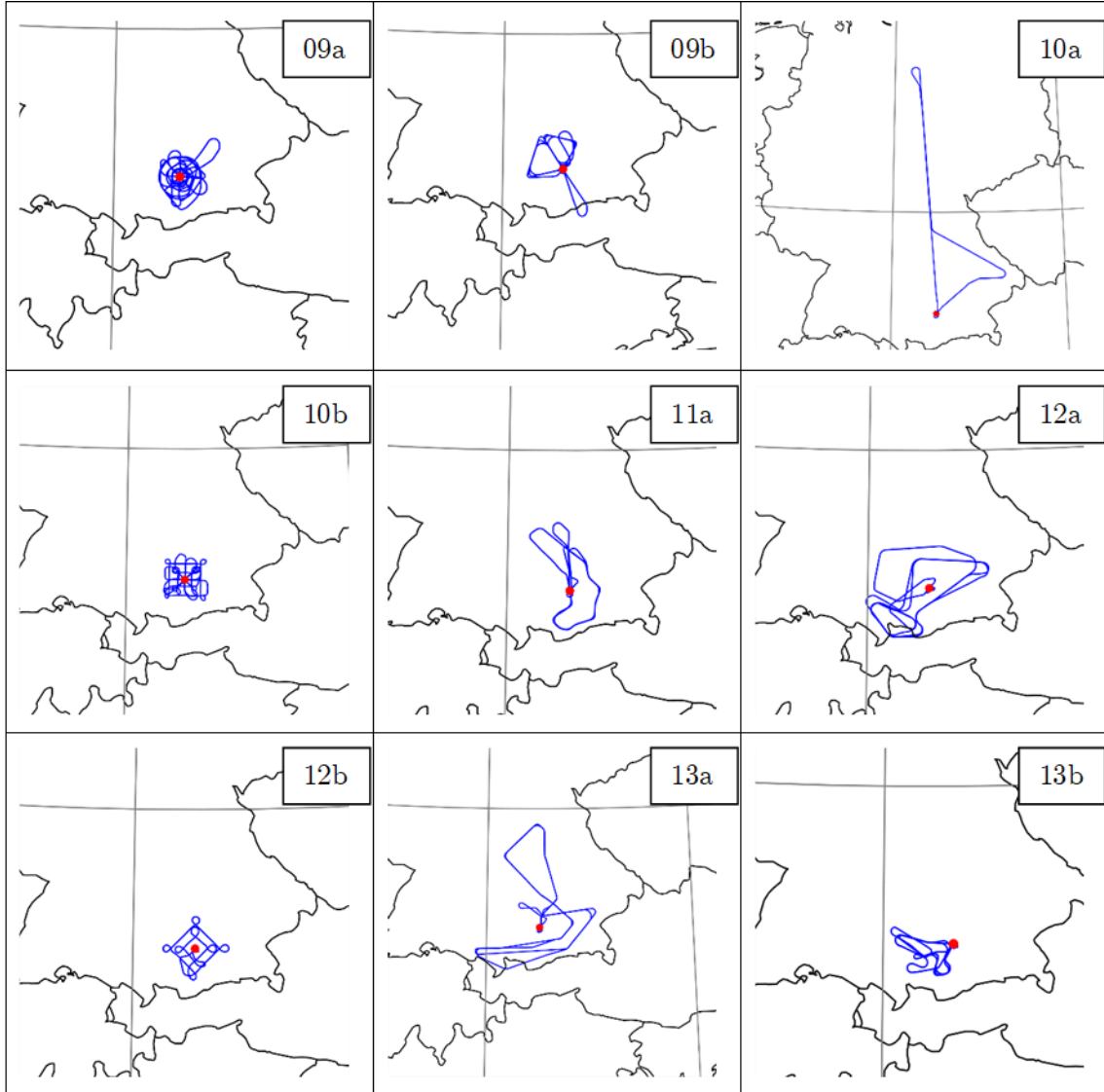
Figure 5.1: Test flights' trajectories' projections on the Earth's surface (blue) and Oberpfaffenhofen airport (red)

The FX facility also provided FMS (Flight Management System) data for each flight. This set of data contains, among others, the FMS time, i.e., UTC time in seconds after the midnight of the flight's day, the Inertial Reference System (IRS) data and the Air Data Computer (ADC) data. More in detail, the IRS (also known as Inertial Navigation System, shortened to INS) contains the aircraft's velocity components, attitude angles and in particular the pitch angle, which is quite relevant within this work, as will

42

be explained in Section 7.1.
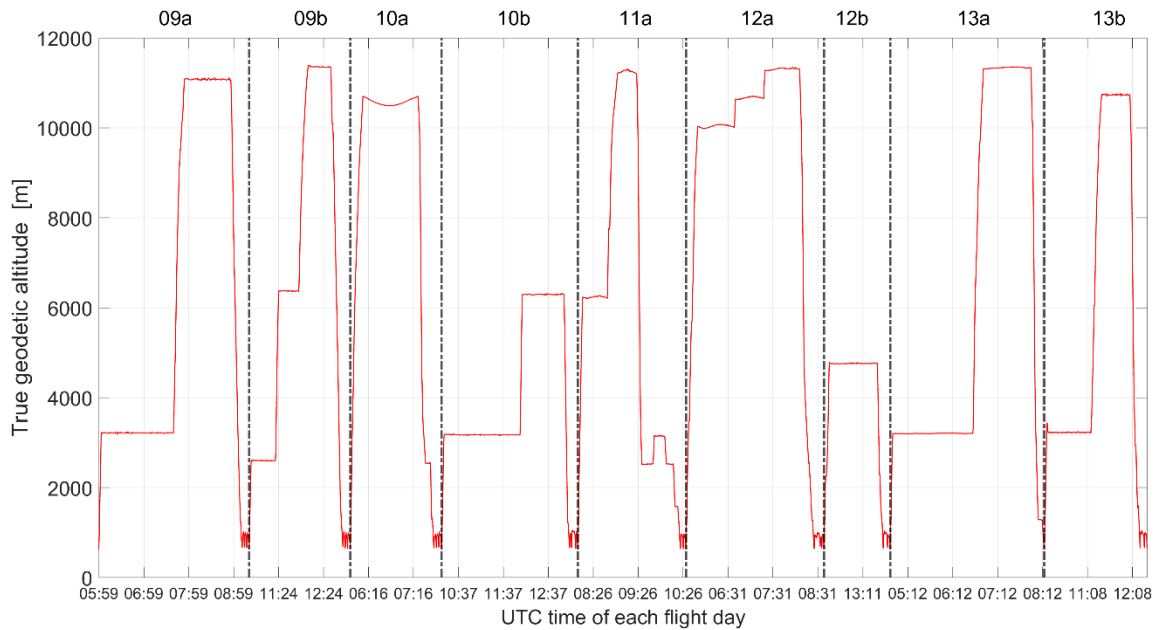
Figure 5.2: Test flights' altitude profiles

The ADC data contains, along with other quantities, the calibrated airspeed, the static air temperature, the true airspeed, the pressure altitude, and the Mach number. A further subset of the FMS data is the Flight Management Computer (FMC) data, which contains the wind angle and wind speed.

The static pressure measurements which were needed to compute the standard pressure altitude were performed by the static pressure ports shown in Figure 5.3.
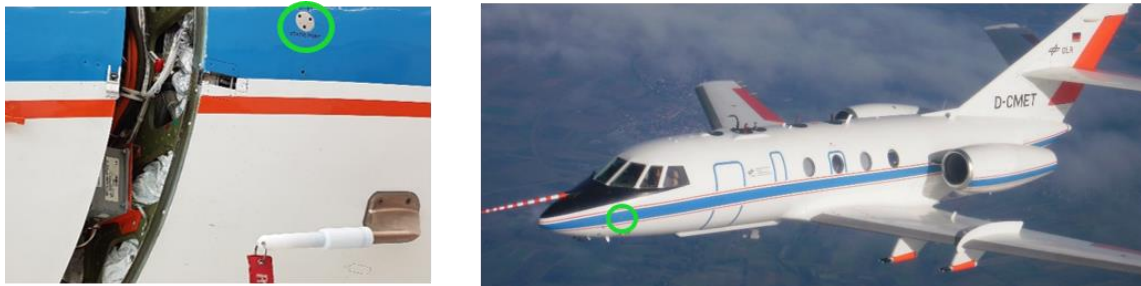
Figure 5.3: DLR's Dassault Falcon 20-E5's static pressure ports, circled in green

Since the GPS data is provided at a frequency of 5 Hz, it was linearly interpolated to match the 10 Hz frequency of the FMS data, in order to use as much data as possible within this work. A list of the quantities which were made available by the DLR FX Facility and which were relevant within the present work is given in Table 5.2.

Parameter	in FMS Data	in GPS post-processed data
North velocity component	X	
South velocity component	X	
Vertical velocity component	X	
Latitude	X	X
Longitude	X	X
Baro-inertial altitude	X	
Standard pressure altitude	X	
Geodetic altitude		X
Wind angle	X	
Wind speed	X	
Pitch angle	X	
UTC Time after midnight	X	
GPS Time		X
Calibrated air-speed (CAS)	X	
Static air temperature (SAT)	X	
Mach number	X	
True air-speed (TAS)	X	
Groundspeed	X	

Table 5.2: Summary of available data (X stands for available)

5.2 Pressure Measurements Retrieval

It may be assumed that the reported pressure altitude in the ADC data was computed according to the standard altitude equation, i.e., Equation (2.25). By reversing this, the pressure measurements may be retrieved. Anyway, first it needs to be made sure that no particular jumps appear in the pressure altitude during airport vicinity flight phases, since this jumps may indicate a pressure altitude correction of the kind described in Section 2.3.1.

By visualizing the three available altitude sets of data, i.e., GPS, IRS, and pressure altitude for any flight, it can be noticed that the IRS and pressure altitude appear to almost coincide at any time. This is shown in Figure 5.4 for flight "11a". However, when plotting in the same figure the deviation of these two altitudes from the GPS one, an offset between them during the initial and terminal flight phases can be seen, as it clearly shown in Figure 5.5. In this figure, the vertical dashed red lines contain the flight portion in which IRS and pressure altitude are almost the same. The same dashed lines are also shown in Figure 5.4.
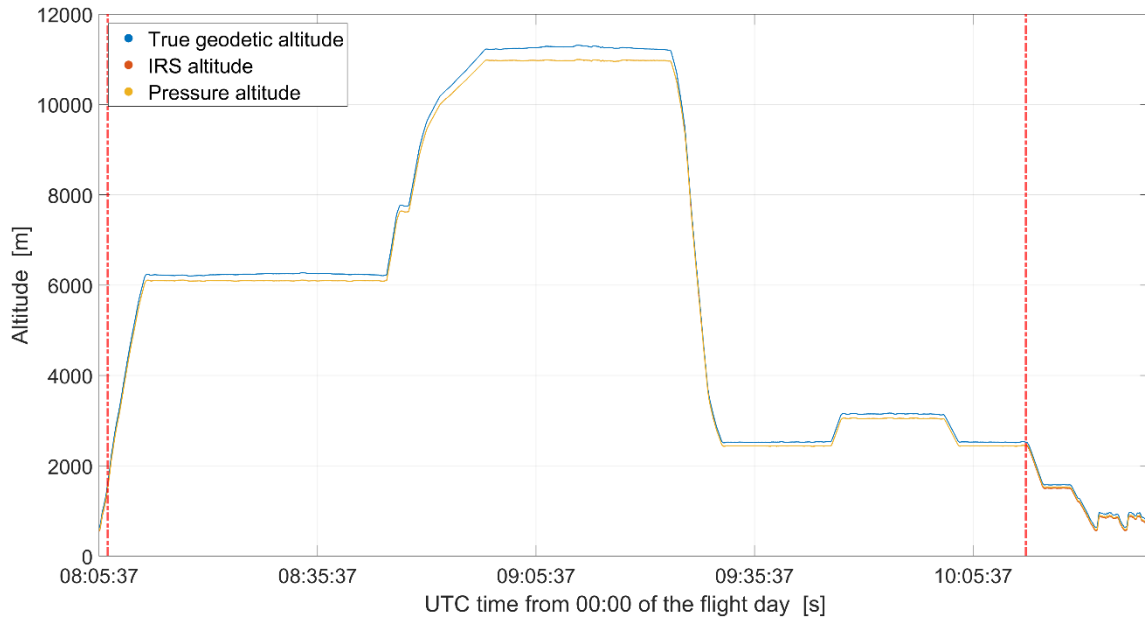
Figure 5.4: Flight "11a" 's GPS altitude and FMS altitudes
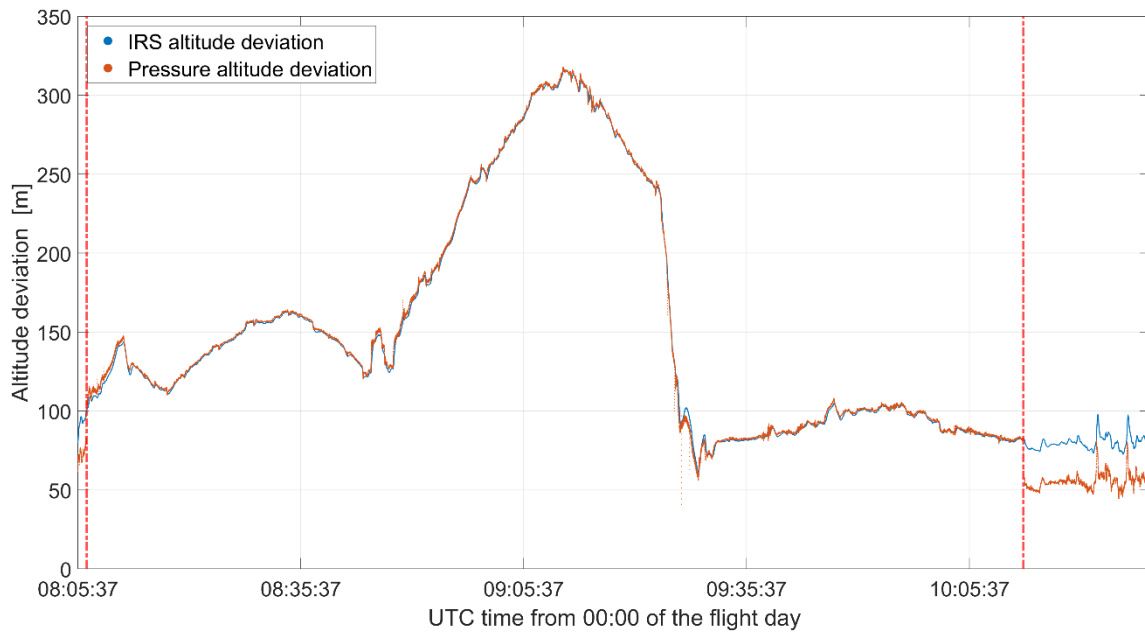
Figure 5.5: Flight "11a" 's FMS altitudes deviations from GPS altitude

The sudden "detachment" of the pressure altitude from the IRS altitude towards the end of the flight, as well as the sudden "attachment" short after take-off, allow to infer that at those time instants the setting for the pressure altitude computation has been changed from QNH to QNE and vice versa, respectively. The IRS altitude, instead, is thought to have been damped uninterruptedly through the standard pressure altitude throughout the whole flight, as it is described in Chapter 3. Unfortunately, the standard pressure altitude is not given in the available data in the time portions outside of the dashed red lines.

If the standard pressure altitude had been reported for the whole flight duration, one may compute the QNH baro-correction in pressure domain, BC_{QNH}, by computing ΔZ_{QNH} with Equation (2.27), inserting it into Equation (2.26) and inverting this. Anyway, this still may be done by considering the IRS altitude as the standard pressure altitude. The BC_{QNH} computed this way is shown in Figure 5.6, along with the standard MSL pressure, p_0.
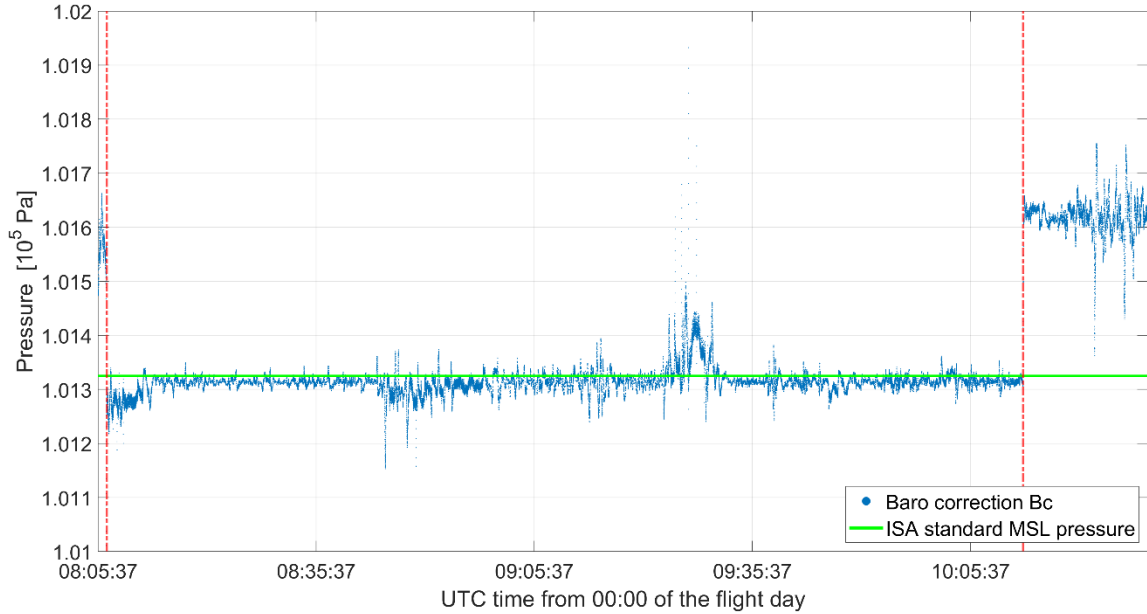
Figure 5.6: Flights "11a" 's guessed QNH baro-correction in pressure domain

The QNH baro-correction in pressure domain retrieved this way is not constant—it actually seems to be noisy—due to the fact that the IRS altitude does not really coincide with the actual standard pressure altitude. The actual BC_{QNH}, nevertheless, is thought to have been constant for at least long-time intervals, since METAR transmission often take place hourly [45, 46].

If the true BC_{QNH} were to be exactly known, and not just roughly estimated as previously described, it would allow for the retrieval of the actual pressure measurements performed by the aircraft's barometer in these portions of the flight outside the dashed red lines. Nevertheless, pressure measurements may be retrieved from the pressure altitude for the main portion of the flight, during which one can be confident that the reported pressure altitude corresponds to standard pressure altitude.

For the two remaining portions of the flight, an estimation of the mean value may be performed, in order to approximate the actual BC_{QNH} and therefore the actual pressure measurements during those portions. This would provide more data for low-altitude analyses but was not performed within this work and remains as an option for future usages of these test flight's data.

For these reasons, further analyses of this flight are done within its central—and longest—portion.

Apart from this way, pressure measurements may be also retrieved with a second

method, from the calibrated airspeed CAS and the Mach number, based on the theory presented . This is done by reverting Equation (A.4) to obtain impact pressure and inserting this in Equation (A.3), which, after being reverted, provides the static air pressure.

According to Equation (A.1), the Mach number may also be computed from the true airspeed, TAS, divided by the speed of sound, which in turn can be computed through Equation (A.2) with the static air temperature measurements provided within the FMS data. However, the Mach number computed this way is found not to coincide with the Mach number in the FMS data, as shown in Figure 5.7.
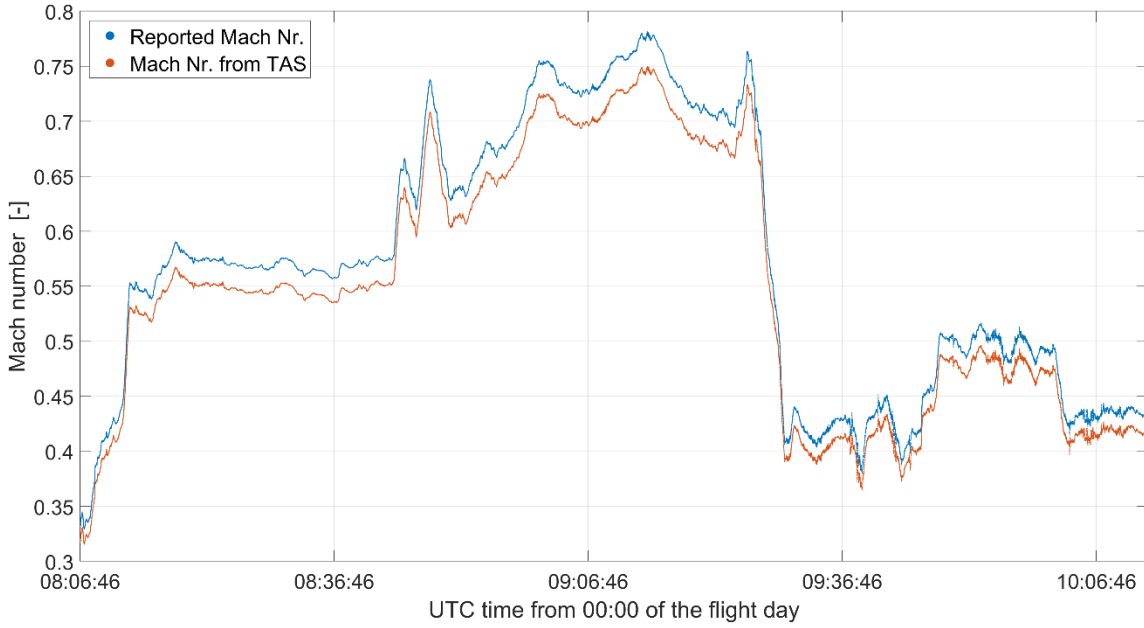
Figure 5.7: Flights "11a" 's reported and computed Mach number values, during the central flight portion

Therefore, depending on which Mach number values are used, this more articulated second method provides different pressures. Furthermore, as compared with the pressures obtained by reverting the pressure altitude equation, they appear to be much noisier, as shown in Figure 5.8.
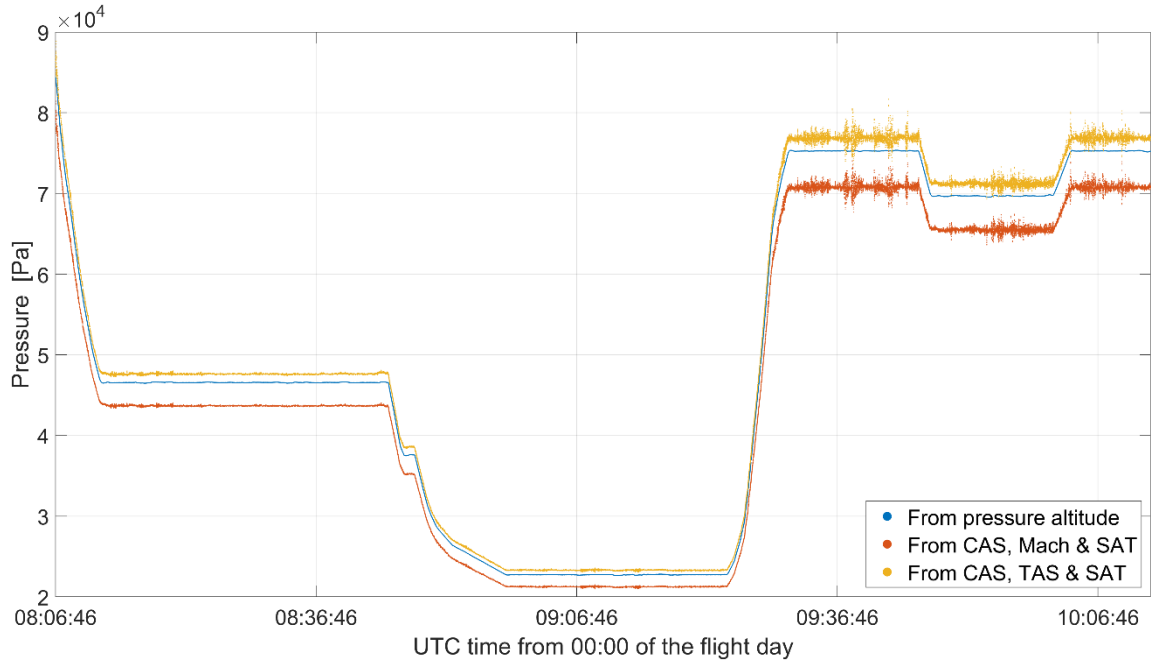
Figure 5.8: Flights "11a" 's differently retrieved pressure measurements, during the central flight portion

The findings of the analysis of flight "11a" about the pressure altitude detachment from the IRS altitude were found to comply with the analyses of all flights, although the detachment/attachment were found to happen at different altitudes, depending on the flight. Moreover, also the findings about this flight's Mach number differences and the differences in the retrieved pressures were found to comply with the analyses of all flights, as shown in Figure 5.9 and Figure 5.10, respectively.

For this reason, it was chosen to focus on each flight's central portion and to consider the pressures obtained from the pressure altitudes on that portion as the actual pressure measurements.
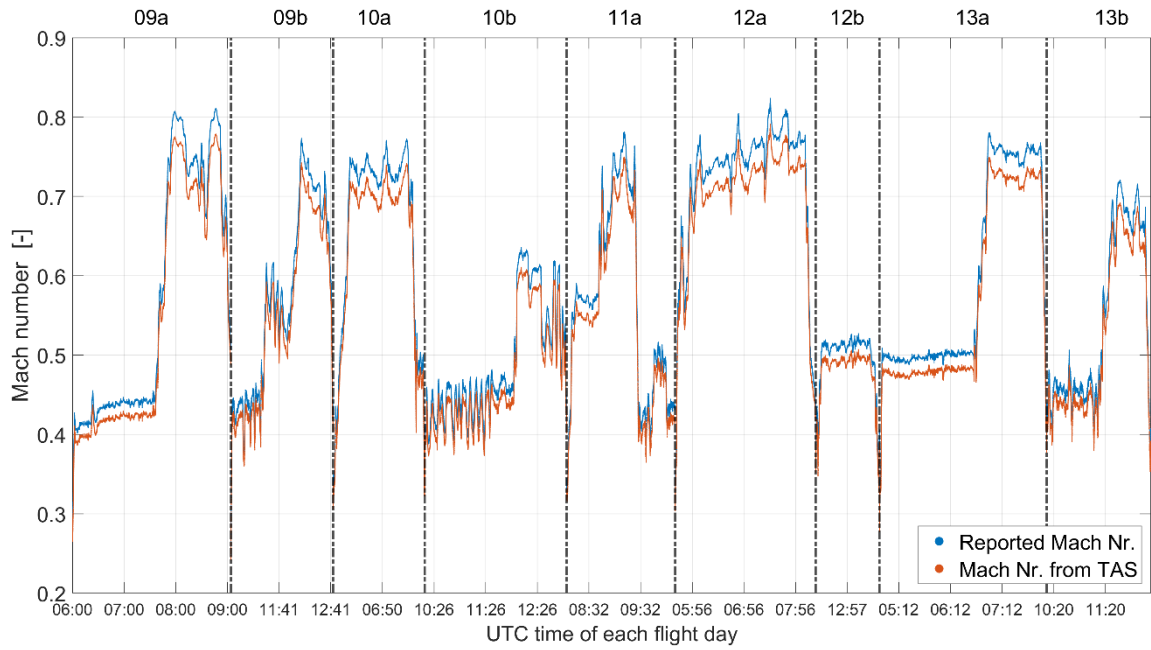
Figure 5.9: Reported and computed Mach number values, during each flight's central portion
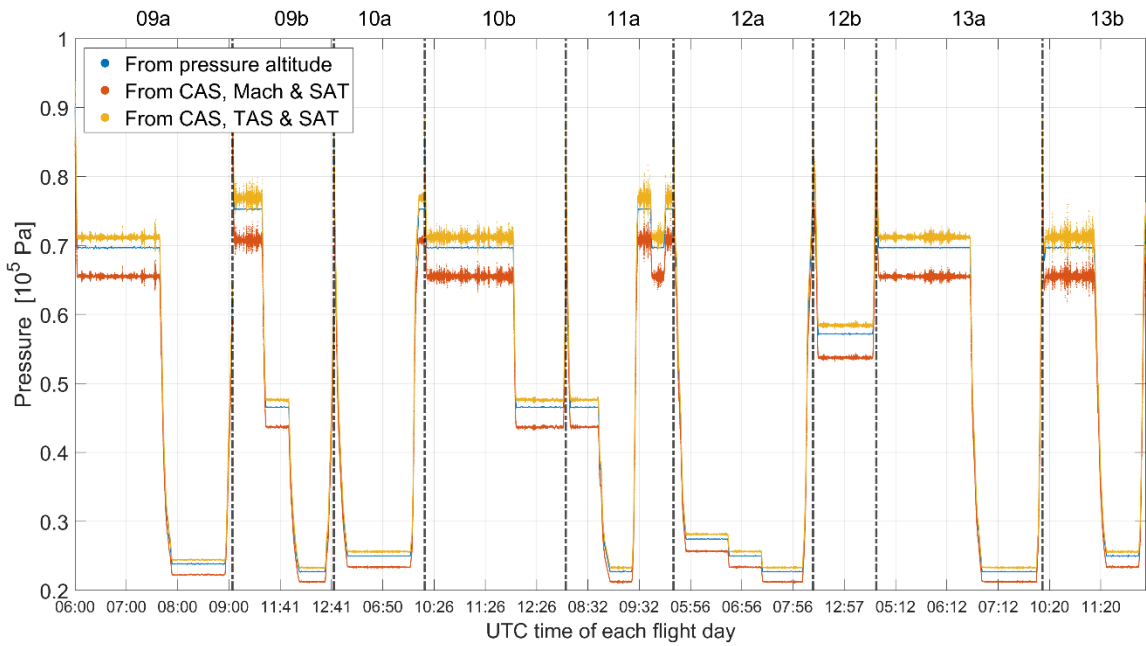
Figure 5.10: Differently retrieved pressure measurements, during each flight's central portion

5.3 Wind and Aircraft's Velocity Components Computation from Available Data

The north and east aircraft velocity components, together with the downward-pointing velocity component along the vertical to the ellipsoid, v_{aD}, build up the 3D vector expressing the velocity with reference to the ECEF-frame and resolved along the axes of the current NED frame:

$$\mathbf{v}_{eb}^n = \begin{pmatrix} v_{aN} \\ v_{aE} \\ v_{aD} \end{pmatrix}. \tag{5.1}$$

A North-East-Down (NED) frame—denoted by the superscript n—is a local navigation frame, which means its origin always coincides the position of the navigating vehicle. As its name suggests, the axes of an NED frame are aligned with the topographic directions, i.e., the north, east and downward directions, at the origin's location. More in particular, in practical applications, the frame may be centered in a peculiar point of the navigating vehicle or of a component of the navigation system [9].

In the IRS data, v_{aN} and v_{aE} are reported. Anyway, in this work, the north and east components of aircraft's velocity were derived from the GPS position data too. First, the ECEF-referenced velocity resolved along the ECEF axes, denoted by $\mathbf{v}_{ea}^e$, was computed by numerically differentiating the aircraft's cartesian GPS position, denoted by $\mathbf{r}_{ea}^e$, through a symmetric difference quotient scheme. This means that the ECEF-referenced velocity vector at the k-th time instant—in which case it is denoted by $\mathbf{v}_{ea,j}^e$—is computed with

$$\mathbf{v}_{ea,j}^e \approx \frac{\mathbf{r}_{ea,j+1}^e - \mathbf{r}_{ea,j-1}^e}{2\Delta t} \ , \qquad j = 2, 3, ..., N-1 \ , \tag{5.2}$$

where Δt denotes the time interval between two consecutive time instants and N denotes the total number of instants. The velocity vector at the first and last time instant, $\mathbf{v}_{ea,1}^e$ and $\mathbf{v}_{ea,N}^e$ were chosen to coincide with $\mathbf{v}_{ea,2}^e$ and $\mathbf{v}_{ea,N-1}^e$, respectively.

From $\mathbf{v}_{ea}^e$, $\mathbf{v}_{ea}^n$ was computed with

$$\mathbf{v}_{ea,j}^n = \mathbf{C}_{e,j}^n \mathbf{v}_{ea,j}^e \quad j = 1, 2, ..., N \ , \tag{5.3}$$

where the coordinate transformation matrix is [9]

$$\mathbf{C}_e^n = \begin{pmatrix} -\sin L \cos \lambda & -\sin L \sin \lambda & \cos L \\ -\sin \lambda & \cos \lambda & 0 \\ -\cos L \cos \lambda & -\cos L \sin \lambda & -\sin L \end{pmatrix}. \tag{5.4}$$

The north and east velocity components from the GPS position numerical differentiation showed to be relatively highly in accordance with their already available IRS counterparts. Anyway, because of the differentiation and because of the general low frequency of the available data, $\mathbf{v}_{ea}^e$ and thus $\mathbf{v}_{ea}^n$ from the GPS position data were found to be too noisy.

In order to prevent a smoothing procedure to have unpredictable effects on Blanchard altitude, in this work it was chosen to employ the v_{aN} and v_{aE} components which are available in the IRS data as the ultimate ones. However, Blanchard altitude computed with the IRS velocity components showed practically no difference with respect to the Blanchard altitude computed with the velocity components obtained from the GPS position.

The north and east wind velocity components were computed based on the wind speed V_w and wind angle ψ_w, provided within the FMC data. The wind angle, which increases clockwise from the North-pointing axis when viewed from above, is the meteorological wind direction, that is the direction from which the wind blows [40].

The two sought wind velocity components can be computed from the horizontal wind speed V_{wh} with the following expressions [40]:

$$v_{wN} = -V_{wh} \cos \psi_w \quad , $$
$$v_{wE} = -V_{wh} \sin \psi_w \quad , $$

(5.5)

which reflect the relationships shown in Figure 5.11.
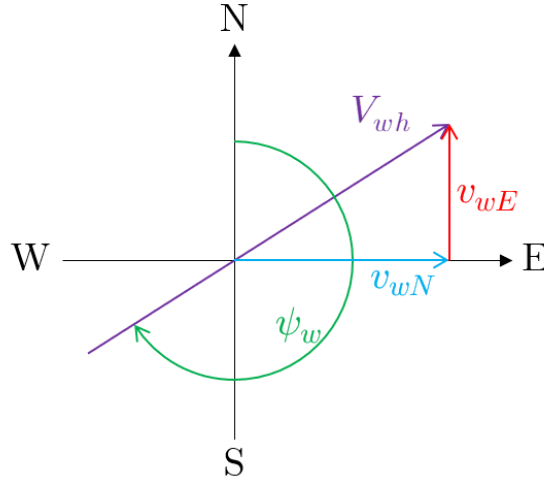
Figure 5.11: Horizontal wind velocity components

Assuming that the given the wind speed V_w coincides with the horizontal wind speed V_{wh} allowed therefore for a straightforward computation of v_{wN} and v_{wE}. This assumption had to be mentioned, since it is unclear whether the given wind speed really is just the horizontal speed or it also includes the vertical wind velocity component. Even in the case that the given wind speed is the modulus of the 3D wind vector, one may still assume that the wind speed almost coincides with the horizontal wind speed most of the time. This is due to the fact that the vertical wind velocity component is much lower than the two horizontal ones [47, 48].

6 Geodetic Altitude Computation Results

Section 6.1 presents the results of the methodology described in Section 4.1 for the computation of geodetic altitude from weather-corrected pressure altitude applied on the nine different test flights presented in Chapter 5.

In Section 6.2, the results of the methodology described in Section 4.2 for the computation of geodetic altitude from Blanchard altitude applied to the same flights are presented

As anticipated in Section 5.2, the results of the two methodologies refer to the central portion of each flight, i.e., in the portion where one can be confident that the retrieved pressure measurements coincide with the actual pressure measurements.

6.1 Geodetic Altitude from ERA5 Weather-corrected Pressure Altitude

In Figure 6.1, the deviation from the true geodetic altitude of the pressure altitude reported in the FMS data is shown in black. The deviation of the weather-corrected pressure altitude is shown in light blue in the same figure. The color code of Figure 6.1, as well as of the other figures in this section, is in accordance with the color code adopted in Figure 4.2 for the different blocks representing each a different kind of altitude.

It is clear that the geodetic altitude form the Blanchard algorithm approximates with a higher accuracy the true geodetic altitude than the standard pressure altitude.

By comparing the standard pressure's deviations with the true geodetic altitude profiles—shown in Figure 6.2—it can be seen that these deviations increase with increasing flight altitude, generally. Such a trend can also be seen in the weather-corrected pressure altitude deviations. In Figure 6.1 a peculiar shape of the deviations of the standard pressure altitude, which can be noticed partially also in the deviations of the other altitude, can be seen. A reason for this is given in the next paragraph.

As said in Section 2.2.2, vertical aircraft guidance is based on flight levels, which means that aircrafts at cruise altitudes fly on isobar surfaces. These can be more or less detached from surfaces of constant geodetic altitude. In flight 09a, e.g., the detachment of the isobar corresponding to the Flight Level at the highest cruise altitude is approximately constant along that flight portion, as can be seen in Figure 6.1. In flight 10a, instead, the isobar surface during the cruise had a varying offset with respect to the true geodetic altitude along the flight. This is likely to be due to the fact that flight 10a

is the one in which the aircraft reached the maximal horizontal distance from the airport, as can be seen in Figure 5.1. This in turn, means that this flight is the one during which the aircraft had the highest chances of flying across regions of different pressure vertical distribution.
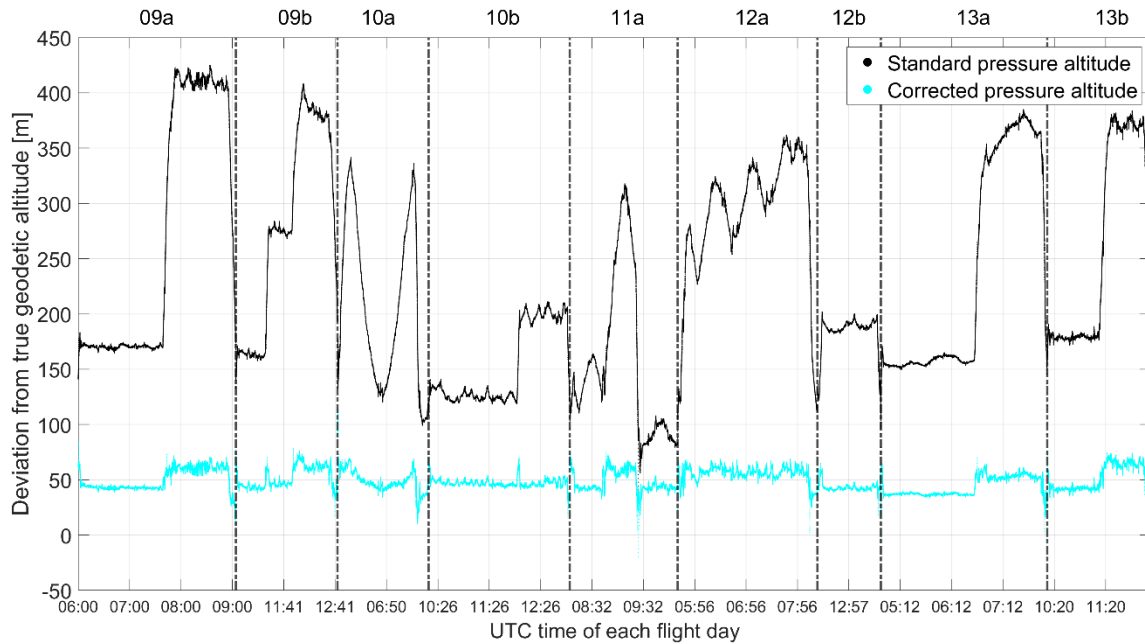
Figure 6.1: Deviation from GPS altitude of the weather-corrected and the standard pressure altitudes, during each flight's central portion
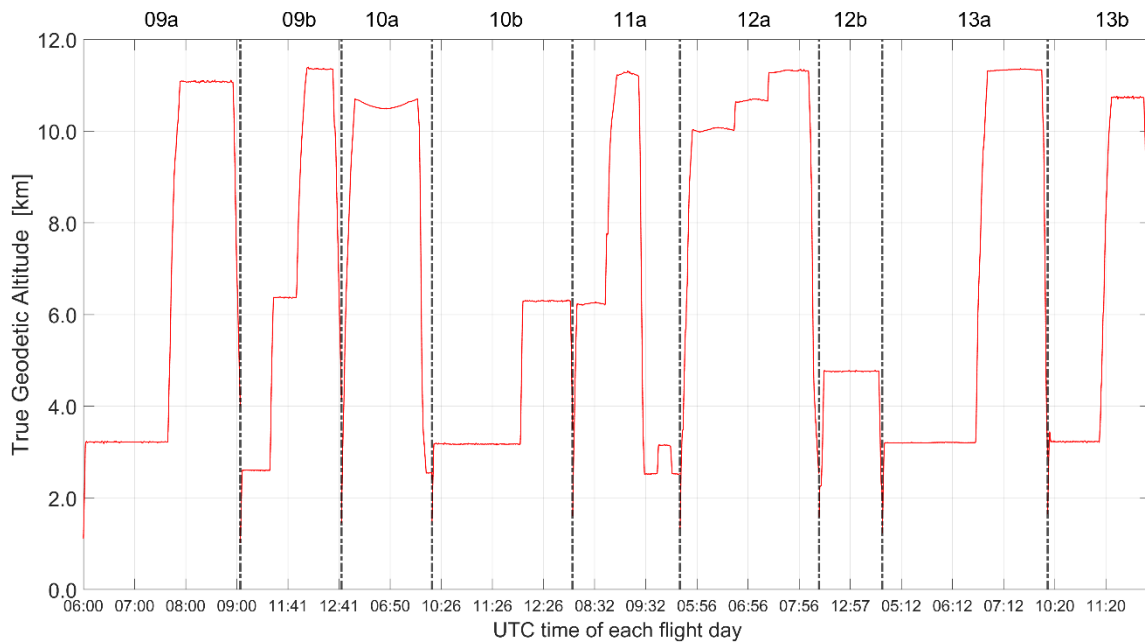
Figure 6.2: Test flights' altitude profiles, during the central flight portions

Proceeding along the blue arrow in Figure 4.1 and Figure 4.2, the consideration of

the geoid undulations, which consists in a shift of the reference to the WGS84 ellipsoid, enables a further improvement in the approximation of the true geodetic altitude. This can be seen in Figure 6.3, where the deviation of weather-corrected pressure altitude referenced to the WGS8e ellipsoid is shown in blue. The deviation still shows some level of modulation with the true geodetic altitude itself.
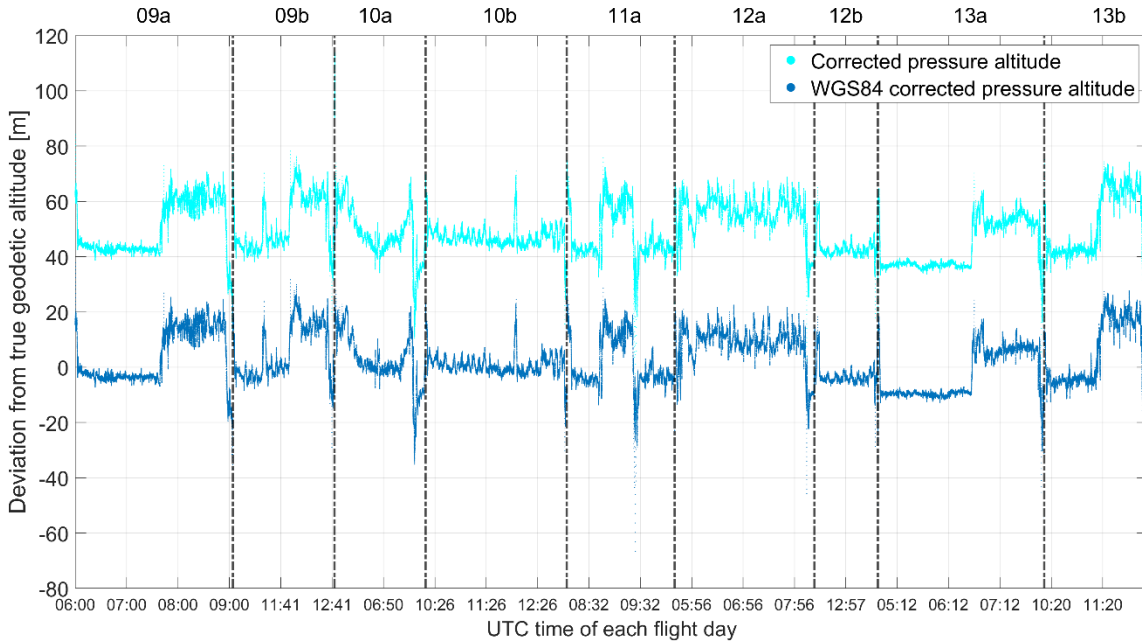
Figure 6.3: Deviation from GPS altitude of the weather-corrected pressure altitude, with and without the reference shift to the WGS84 surface, during each flight's central portion

By applying the next step of the methodology represented by the blue arrow, i.e., the conversion of the altitude scale, the deviations are further reduced, generally. This is shown in Figure 6.4. Here, the deviation of weather-corrected pressure altitude referenced to the WGS8e ellipsoid and in the geometric scale is shown in dark blue.

Being the weather-corrected pressure altitude referenced to the WGS8e ellipsoid and in the geometric scale nothing but the geodetic altitude from the weather-corrected pressure altitude, its deviation from the true geodetic altitude may now be referred to as errors in the geodetic altitude.

These errors show a lower level of modulation in comparison with the deviations of the previous figures of this section.
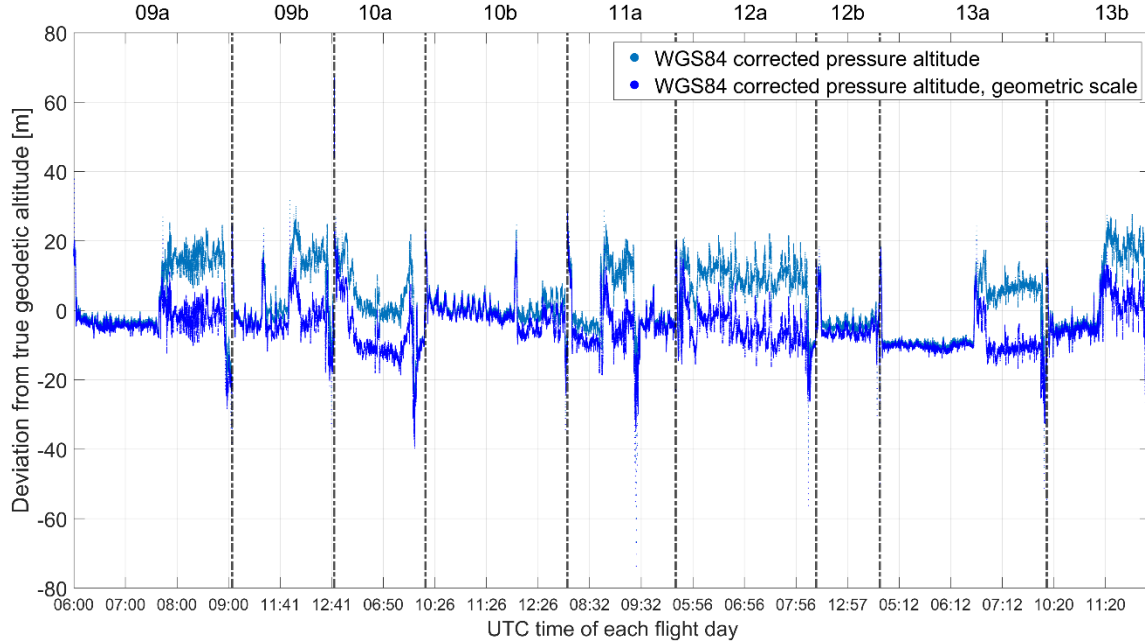
Figure 6.4: Deviation from GPS altitude of the WGS84-referred weather-corrected pressure altitude, before and after the scale conversion, during each flight's central portion

6.2   Geodetic Altitude from Blanchard Altitude

In this work, the Blanchard altitude was computed at each time instant in which the needed quantities are to be found in or computed from the available test flights' data. The errors in the geodetic altitude obtained from the Blanchard altitude with FMS data are shown in green in Figure 6.5. In the same figure, the deviation of the standard pressure altitude is shown in black. The color code is here in accordance with the color code adopted in Figure 4.2.

The geodetic altitude from the Blanchard algorithm appears to be more accurate in the approximation of the true geodetic altitude. Anyway, in some flights (flights 12a and 13a, especially) a drifting tendency of the errors in the geodetic altitude obtained via the Blanchard algorithm can be noticed. These drifts were expected, because of the iterative nature of the Blanchard algorithm, as described in Section 4.2.

The second term of the Blanchard algorithm's equation, i.e., the one involving the velocity measurements, is herein referred to as the wind term. To show its effect on the altitude computation, Figure 6.6 is presented.

56
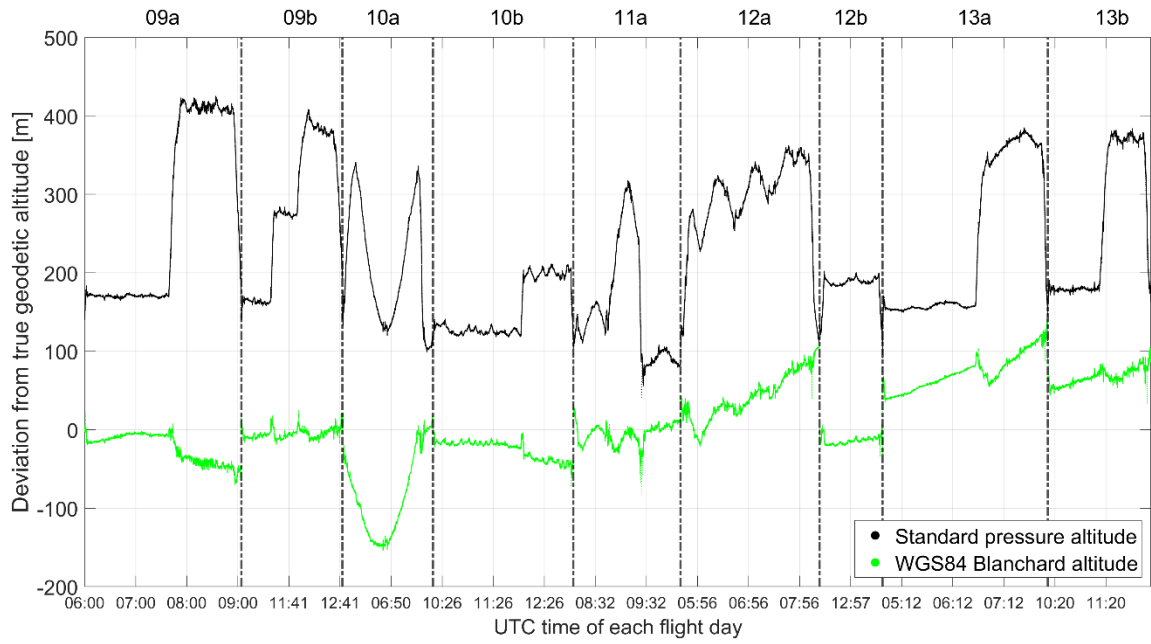
Figure 6.5: Deviation from GPS altitude of the geodetic altitude from "Blanchard altitude" and the standard pressure altitude, during each flight's central portion

In Figure 6.6, the errors in the geodetic altitude obtained from the Blanchard algorithm without the wind term are shown in magenta. In this case, the errors appear larger in some flights' portions and smaller in other.
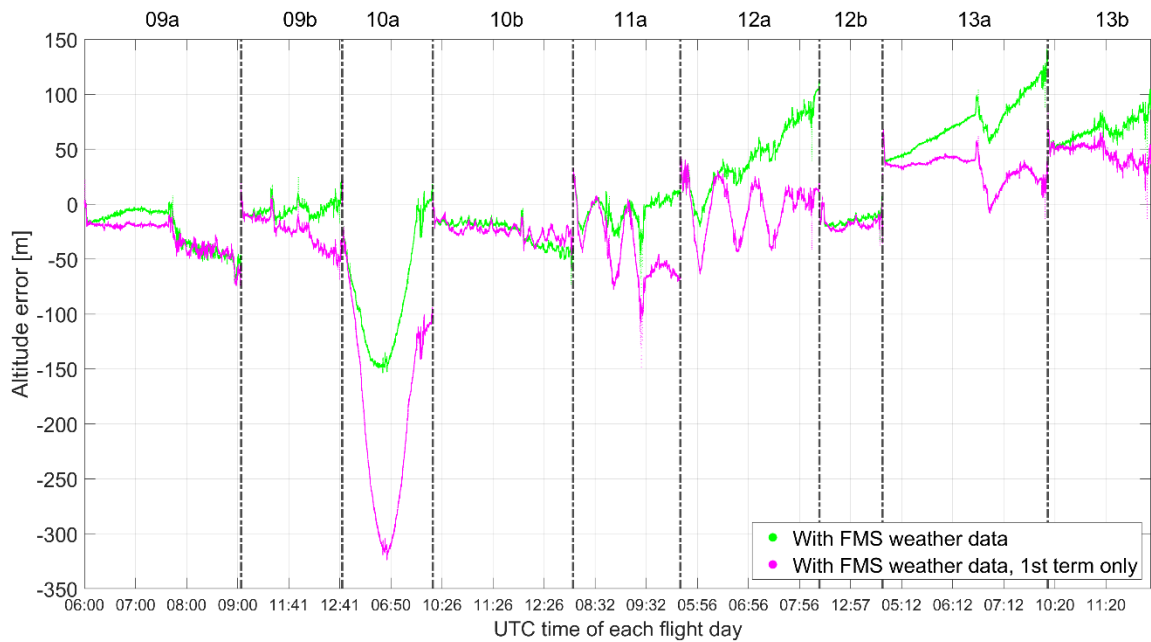
Figure 6.6: Deviation from GPS altitude of geodetic altitude from "Blanchard altitude, with and without the wind-term during each flight's central portion

57

Figure 6.7 shows the errors in the geodetic altitude from the Blanchard altitude obtained using as pressure, temperature, and wind velocity measurements the pressure, virtual temperatures and wind velocity obtained from the ERA5 weather data. As in Figure 6.6, in Figure 6.7, the errors in the geodetic altitude obtained with and without the wind term are plotted in green and magenta, respectively. In both cases the obtained geodetic altitudes with the ERA5 weather data approximate the true geodetic altitude in a more accurate way with respect to their counterparts obtained with the FMS measurements.
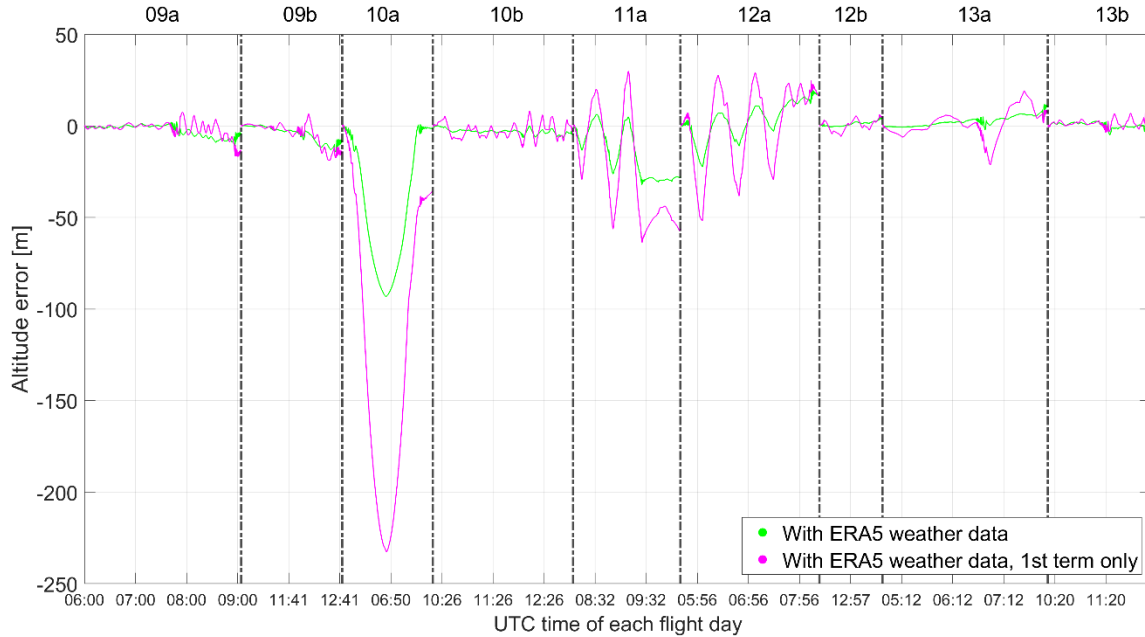
Figure 6.7: Deviation from GPS altitude of geodetic altitude from "Blanchard altitude" using ERA5 data and considering humidity, with and without the wind-term, during each flight's central portion

Figure 6.7 shows that when using ERA5 weather data the consideration of the wind term within the Blanchard algorithm yields better results in terms of accuracy with respect to the true geodetic altitude. This, along with the generally better performance of the Blanchard algorithm with ERA5 data than with FMS measurements, may indicate that the ERA5 data is more accurate than the FMS measurements.

The use of ERA5 data also allows to use the specific humidity, that is not provided in the FMS measurements, to compute the virtual temperature that is then used within the Blanchard algorithm. When not considering the effect of humidity, the accuracy achieved by the Blanchard algorithm with the ERA5 data is lower, as shown in Figure 6.8.

In Figure 6.9, the deviations from the true geodetic altitude of the three different altitude outputs of the flow diagram in Figure 4.2 are shown. These are the standard pressure altitude (in black), the geodetic altitude obtained from the Blanchard algorithm using the FMS measurements (in green), and the geodetic altitude from the weather-corrected pressure altitude (in blue). The color code corresponds to the one of

Figure 4.2. It is clear that the overall best option for approximating the true geodetic altitude is the third option. This is therefore the only geodetic altitude computation option that is considered in the remaining chapters of this thesis.
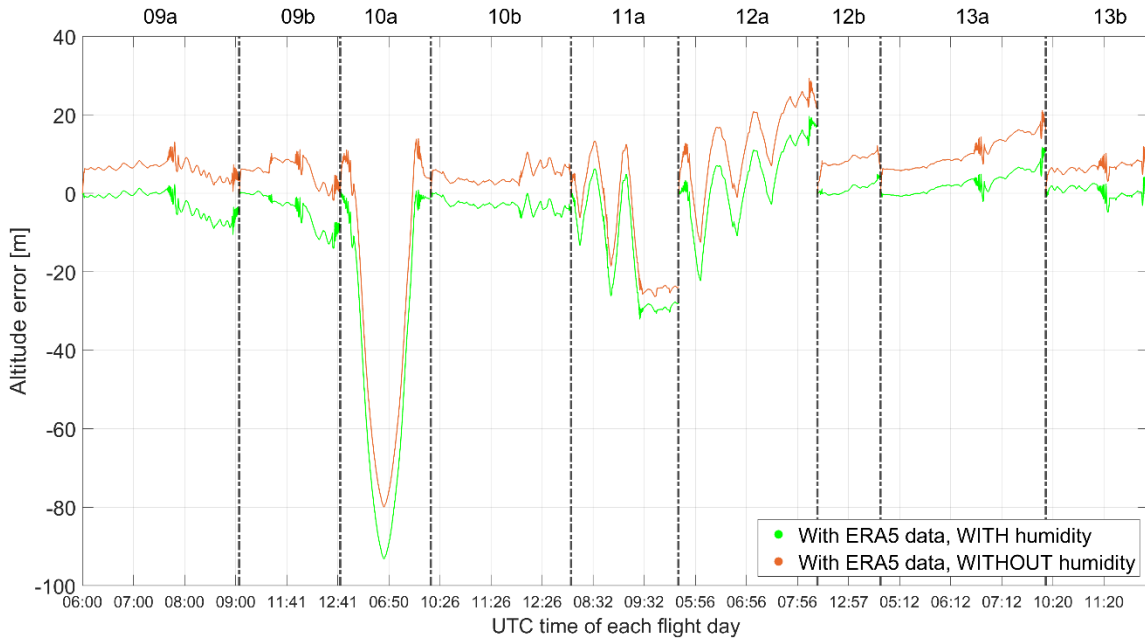
Figure 6.8: Deviation from GPS altitude of geodetic altitude from "Blanchard altitude" using ERA5 data, with and without the consideration of humidity, during each flight's central portion
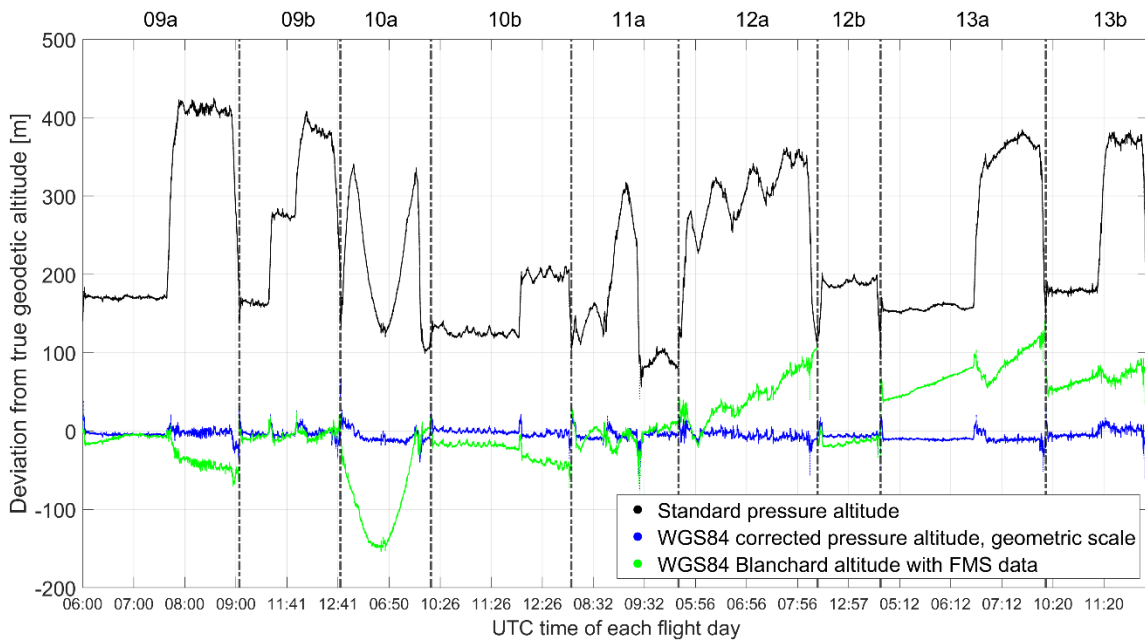
Figure 6.9: Comparison of the deviations from the GPS altitude, during each flight's central portion

7 Modeling of Weather-corrected Pressure Altitude Errors for Snapshot Algorithms

This chapter describes the procedure employed for the modeling of the best geodetic altitude computation method, i.e., the one based on weather-corrected pressure altitude, for geodetic altitude navigation snapshot algorithms.

First, in Section 7.1, an empirical model is derived to compensate for the effects induced by the aircraft's pitch attitude on the errors in the geodetic altitude from weather-corrected pressure altitude.

Section 7.2 focuses on the required modeling of the residual altitude errors for Snapshot algorithms.

The results of the procedure presented in this chapter are presented and discussed in Section 7.3.

7.1 Mitigation of the Aircraft Dynamics Effects on the Altitude Errors

The errors in the geodetic altitude from the Blanchard algorithm, that is denoted by h_B, may be defined as

$$E_B = h - h_B \ , \tag{7.1}$$

where h is the true geodetic altitude, that is the altitude reported in the post-processed GPS data. Analogously, the errors in the geodetic altitude from the weather-corrected pressure altitude, that is denoted by h_w, are defined as

$$E_w = h - h_w \ . \tag{7.2}$$

Peculiar relationships of E_B and E_w with respect to many different flight mechanics quantities were visually looked for. Among these quantities, there are some which were to be found in the available flight data and others which were computed based on the former ones and/or on weather data. These quantities are: the NED velocity components; the bank, pitch, and yaw angles; the angle of attack and the angle of sideslip; altitude; Mach number and true airspeed.

The errors in the geodetic altitude from the Blanchard algorithm were not found to be visually correlated to any of the aforementioned quantities. In contrast, E_w showed

an approximately linear relationship with respect to the pitch angle. The inflow direction into the pressure ports, shown in, may be responsible for this.

A linear model was found through the MATLAB® function robustfit, which produces robust multiple linear regressions, by using the bisquare (also known as biweight) fitting weight function. In particular, the outputs of the MATLAB® function robustfit are the two paremeters needed for the definition of the linear model, i.e. its offset B and the slope A, defined such that

$$y = A\,\theta + B\,.$$ (7.3)

where θ is the aircraft's pitch angle.

To evaluate the performance of this linear regression, its results were compared with the outputs of linear regressions using other weight functions, such as the Cauchy's, the Andrews's, the Welsch's weight functions, and others. All of these options produced almost the same results.

Having a model, expressed by Equation (7.3), for the pitch-induced effects on h_w, this can be used to obtain a generally more accurate geodetic altitude. This altitude, denoted by $h_{w,\theta}$, is referred to as the pitch-compensated geodetic altitude from weather-corrected pressure altitude. Another, still long, name which in this thesis is used to refer to this altitude is geodetic altitude from pitch-compensated, weather-corrected pressure altitude. This other name does not reflect that the pitch compensation is done in the geodetic altitude domain, instead in the pressure altitude one. Anyway, this name is sometimes used in this thesis to first highlight the fact that this altitude is a geodetic one.

This so-called pitch-compensation is applied as follows

$$h_{w,\theta} = h + y.$$ (7.4)

As it will be shown in Section 7.3, the pitch-compensation is able to reduce the deviation from the true geodetic altitude.

7.2 Residual Errors' Modeling for Snapshot Algorithms

In a hypothetical integration of the considered geodetic altitude measurements, i.e., $h_{w,\theta}$, within a snapshot (i.e., single-epoch) algorithm, an overbounding distribution of the residual errors would be needed. This distribution may be a gaussian distribution, for instance.

In this work, based on [49], two different overbounding gaussian distributions are first obtained. One of them bounds the residual errors' distribution on the distributions' left-hand side and the other bounds the right-hand side. The computation of the two overbounding gaussian distributions' parameters is performed via the MATLAB® Toolset which was used by the authors of [49] and which is available at [50].

By selecting the mean with the largest absolute value and the largest standard deviation among the mean values and the standard deviations of the two overbounding

gaussian distributions, a third overbounding gaussian distribution is obtained. This is the gaussian distribution which overbounds the whole residual errors' distribution.

7.3 Results of the Residual Errors' Mitigation and Modeling

The distribution of the errors in the geodetic altitude with respect to the pitch attitude angle is shown in Figure 7.1 for each of the nine different investigated flights. The distribution appears to be approximately linear. The corresponding linear model obtained via linear regression is shown in Figure 7.2.

The two parameters defining the model obtained by using the bisquare fitting weight function are found to be $A \cong 140$ m rad$^{-1} \cong 2.44$ m deg^{-1} and $B \cong -14.5$ m.
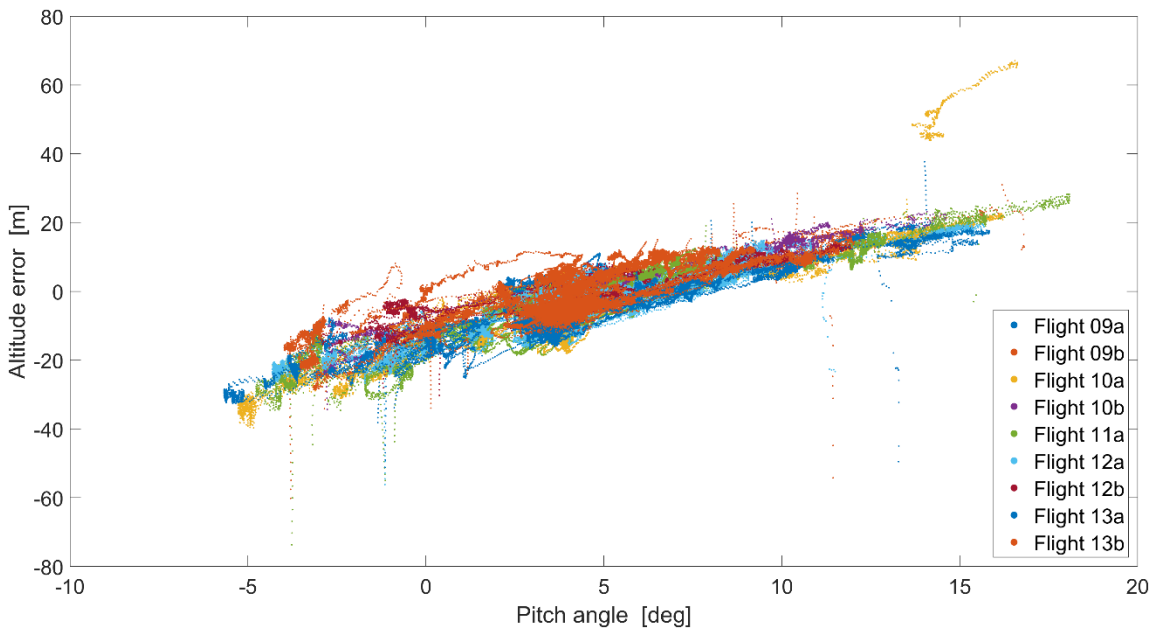
Figure 7.1: Distribution of the errors of the geodetic altitude from the weather-corrected pressure altitude versus the pitch angle, during each flight's central portion

This almost linear relationship between the altitude errors and the pitch attitude is reflected in an approximately linear relationship between the pitch attitude and the deviation of the barometric pressure and the ERA5 interpolated pressure. This is shown in Figure 7.3. The corresponding linear model is shown in this figure for the sake of completeness.
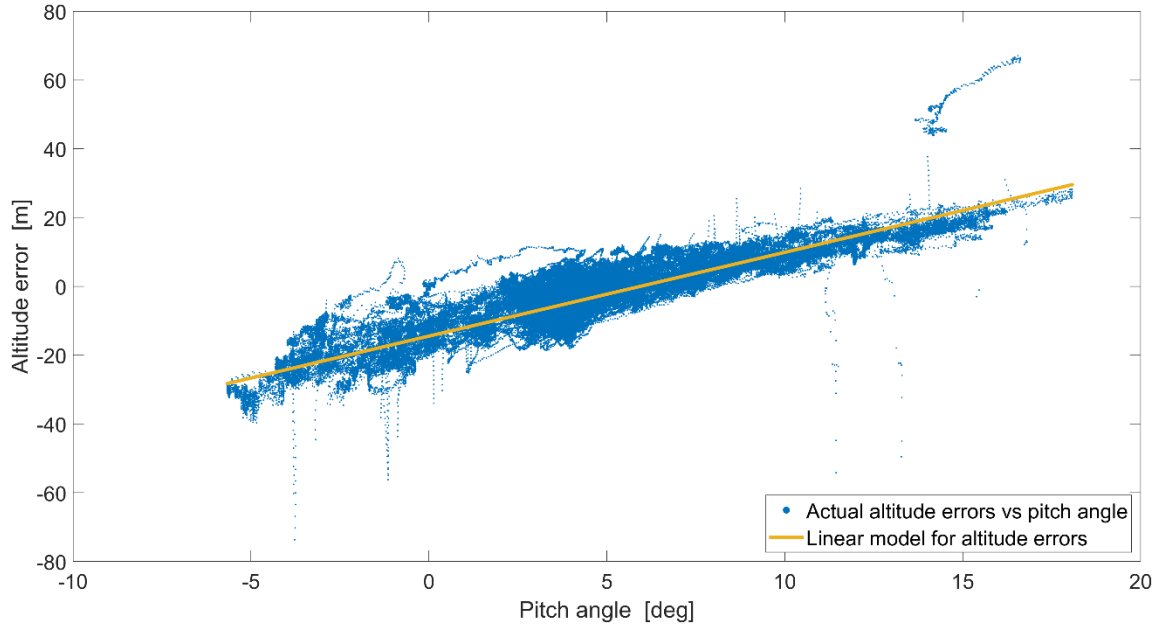
Figure 7.2: Linear model for the errors of the geodetic altitude from the weather-corrected pressure altitude versus the pitch angle, during each flight's central portion
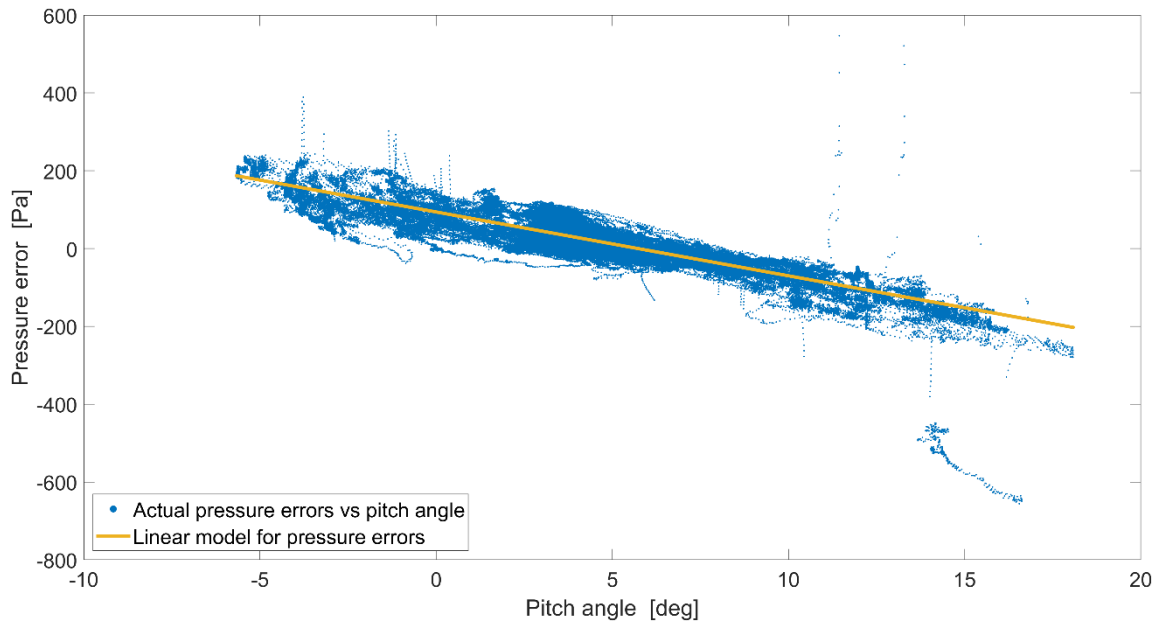
Figure 7.3: Linear model for the deviation of the barometric pressure and the interpolated ERA5 pressure versus the pitch angle, during each flight's central portion

After applying, via Equation (7.4), the compensation for the errors induced by the pitch attitude, the residual errors are found to be generally shifted closer to the zero and the magnitudes of their spikes are found to be generally lower, as shown in Figure 7.4. The number itself of the spikes is visually shown to be decreased.
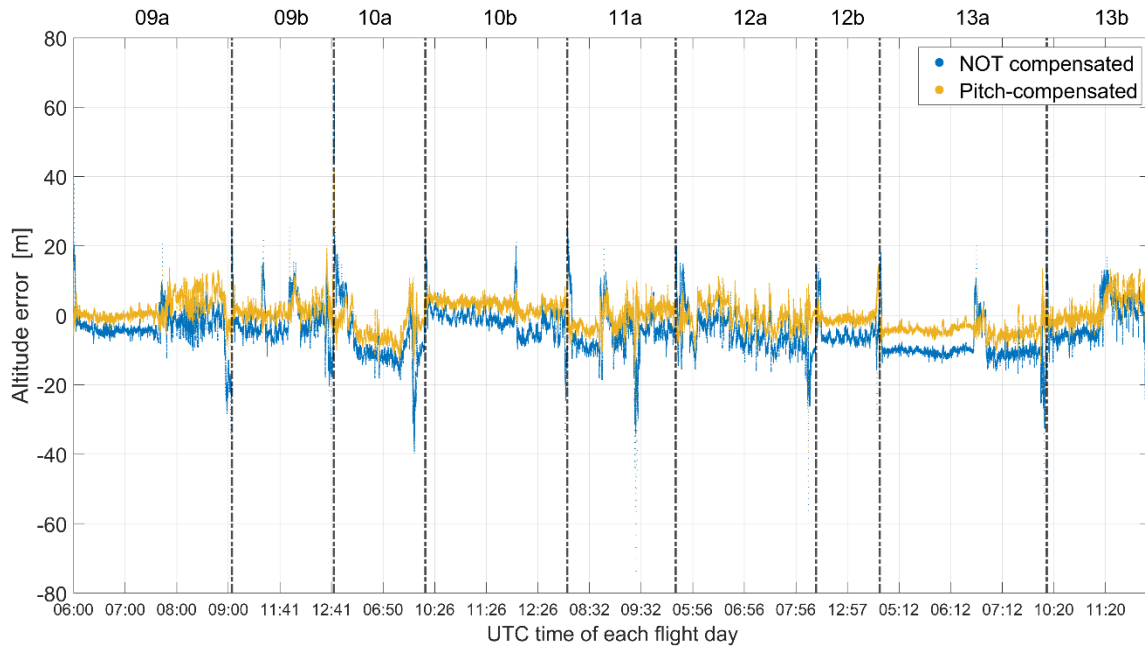
Figure 7.4: Altitude errors, with and without pitch-compensation, for all flights, during the central flight portions

The statements in the previous paragraph regarding the improvement in the errors' distribution is further reflected by Figure 7.5, in which the histograms of the errors before and after the so-called pitch-commendation are shown.
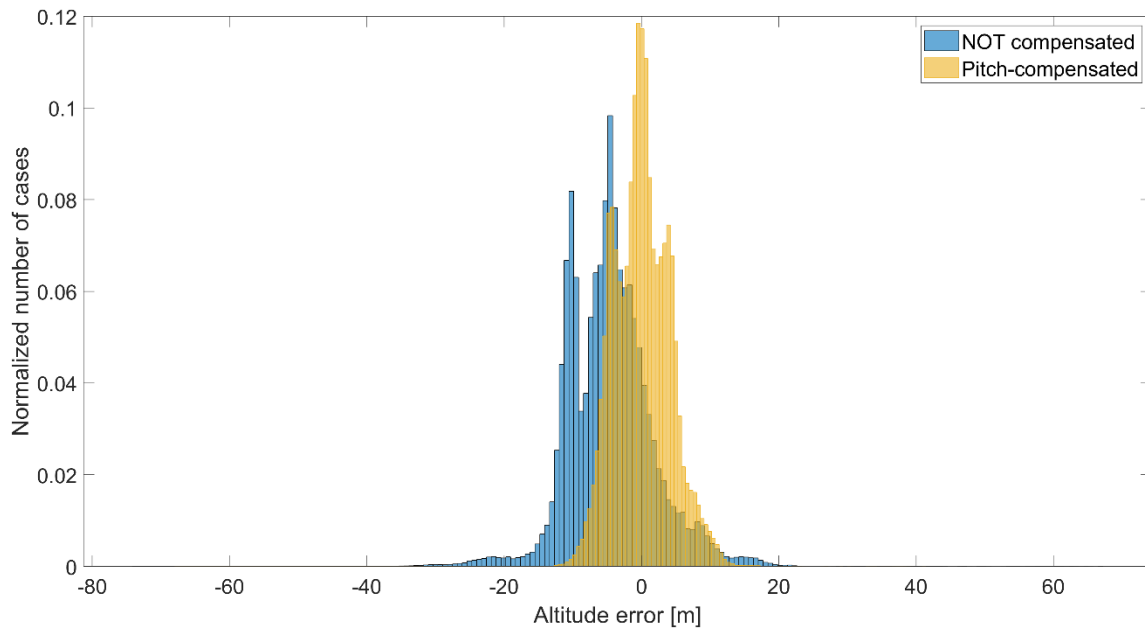
Figure 7.5: Altitude errors' distribution, with and without pitch-compensation, for all flights, during the central flight portions

The mean and the standard deviation of the errors in geodetic altitudes after the

pitch-compensation are 0.1 and 4.1 m. Their counterparts before the pitch-compensation are -4.6 and 6.4 m, instead.

The altitude errors after the application of the linear model compensation are referred to as the residual (altitude) errors. The cumulative density functions (CDFs) of the right-hand side part of the residual errors' distribution and the related overbounding gaussian distribution are shown in Figure 7.6. The gaussian distribution shows to be actually overbounding the errors' distribution for quantile values larger than zero.
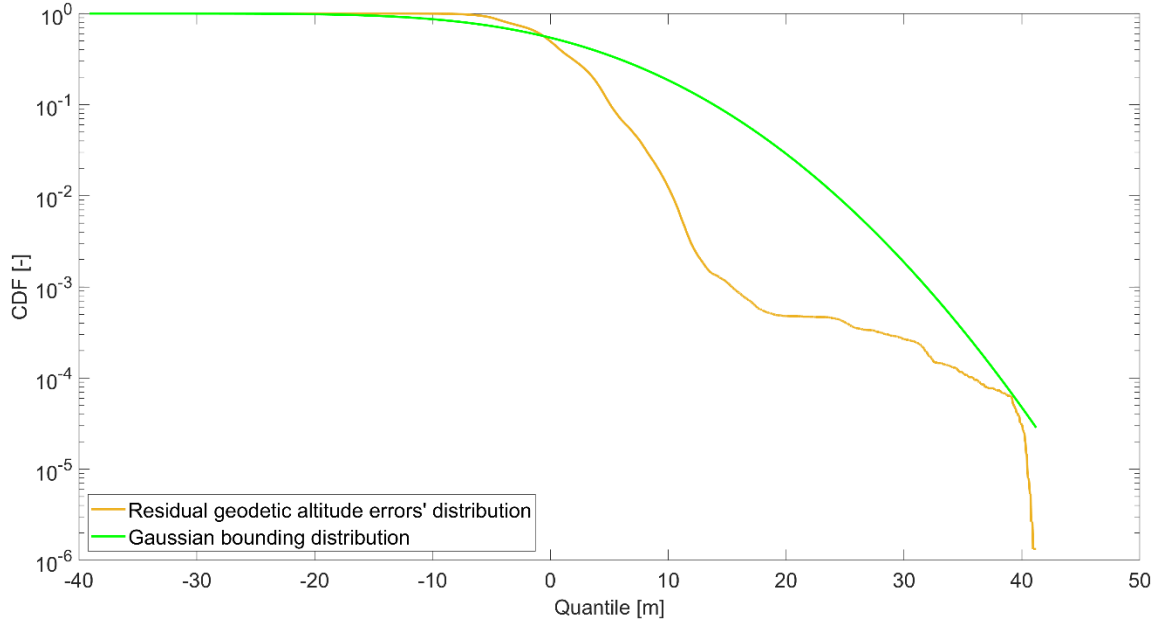
Figure 7.6: CDF of the right-hand side part of the errors' distribution and of the related overbounding gaussian distribution, for all flights, during the central flight portions

The counterpart of Figure 7.6, i.e., the CDF bounding on the left-hand side, is shown in Figure 7.7.

The parameters defining the two bounding standard deviations are summarized in Table 7.1. The single overbounding gaussian distribution is then the one defined by a mean of 1.0717 m and standard deviation of 14.9362 m, respectively.

Parameter	Right-hand side	Left-hand side
Mean [m]	1.0717	-0.527
Standard Deviation [m]	9.9738	14.9362

Table 7.1: Mean and standard Deviation of the two gaussian distributions bounding the tow hand sides of the residual errors' distribution
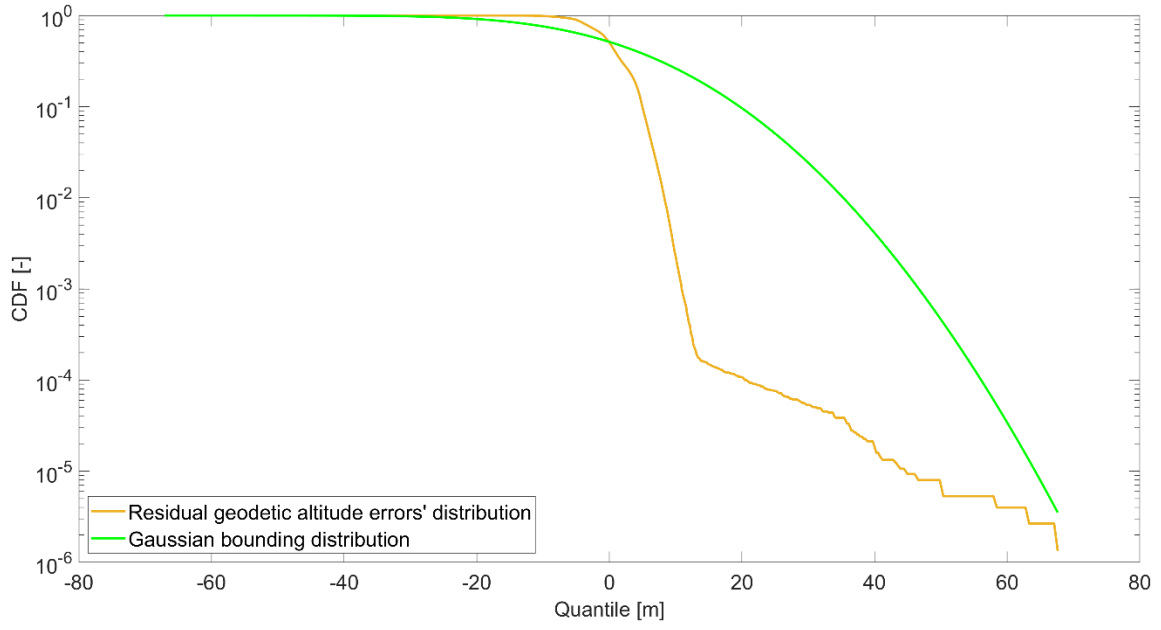
Figure 7.7: CDF of the left-hand side part of the errors' distribution and of the related overbounding gaussian distribution, for all flights, during the central flight portions

8 Modeling of Weather-corrected Pressure Altitude Errors for Sequential Algorithms

In this chapter, an exemplary sequential estimator for the integration of the geodetic altitude from the weather-corrected pressure altitude with INS&GNSS is presented. Throughout this chapter, the geodetic altitude after the pitch-compensation, described in Chapter 7, is considered.

It shall be noted that no estimator algorithm has been implemented within this work. This example is given in order to highlight what would be a viable error modeling of the considered geodetic altitude measurements for sequential estimators. This may also be useful for sequential estimators of different kinds that may be designed and implemented in future work. The error modeling is described in Section 8.1.1.

The measurement model and measurement noise variance related to these geodetic altitude measurements' integration are shown to be depending on the external weather data in Sections 8.1.2 and 8.1.3.

The results of the procedures presented in this chapter are illustrated and discussed in Sections 8.2 to 8.4.

8.1 Error Model Considerations Needed for the Integration in a Sequential Estimator

The computed altitude which is the best at approximating the true geodetic altitude is the pitch-compensated geodetic altitude obtained from weather-corrected pressure altitude $h_{w,\theta}$. This section describes the methodology for its integration within a loosely-coupled (LC) Kalman Filter for vertical positioning. For the sake of shortness, in this section, the aforementioned computed altitude is simply referred to as the processed baroaltimeter altitude and is denoted by h_b, i.e.

$$h_b = h_{w,\theta} \ .$$
(8.1)

The LC KF-based estimation algorithm within which the processed baroaltimeter altitude could be integrated may be of the kind described in Section B.3, whereby various navigation aiding subsystems, e.g., GNSS, enter their own computed navigation solution component to the estimator, in an error-state implementation.

The aiding subsystem that comprises the barometric altimeter is supposed to provide

the estimator with the processed baroaltimeter altitude. It is therefore assumed that a computer within this subsystem applies all the required transformations to convert pressure measurements into the processed barometric altitude before this subsystem's output enters the estimator. In particular, before actually entering the KF algorithm, the INS altitude is subtracted from the processed baroaltimeter altitude, as it described in Section B.3 for a generic altimeter.

A flow diagram representing such a navigation system aboard an airplane is shown in Figure 8.1, in which the aiding subsystems, as well as the INS, are enclosed in blue rectangles with rounded corners.
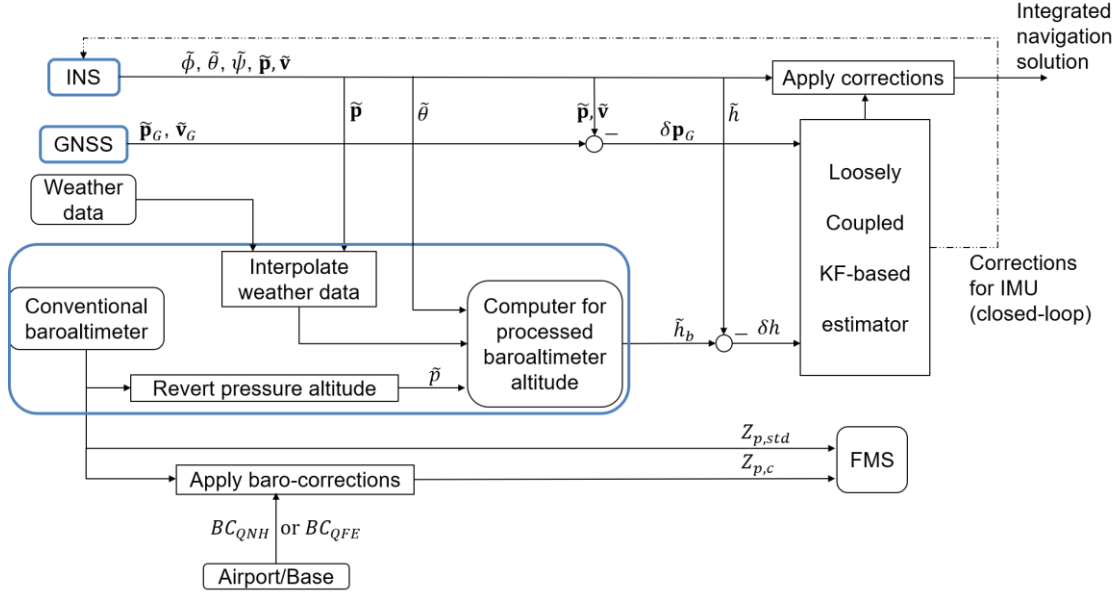
Figure 8.1: Potential flow diagram for processed baroaltimeter altitude integration

In this figure, the processed baroaltimeter altitude is denoted by $\tilde{h}_b$, while the INS navigation solution is denoted by $\tilde{h}$. The attitude angles, i.e., bank, pitch and yaw angles are denoted by ϕ, θ and ψ, respectively. The vectors $\mathbf{p}$ and $\mathbf{v}$ denote position and velocity instead, which additionally feature the subscript G in the case they are output by the GNSS aiding subsystem. In this figure, also the standard and the baro-corrected pressure altitude are shown. They enter the FMS in order to be used for vertical separation between airplanes.

As can be seen from this figure, in this hypothetical integration, the interpolation of weather data in order to provide references for the weather-corrected pressure altitude computation is done with the position delivered by the INS. The position is also used within the barometric altimeter subsystem's computer for assessing the geoid undulations and the difference between the geometric and geopotential altitude scales. This computer also takes as input the pitch angle to apply the pitch-compensation.

Anyway, this figure only represents an example of possible integration in real time. In the present work, post-processed GPS data has been used for the interpolation of the

weather data and computation of the geoid undulation, as well as of the difference between geometric and geopotential altitude scales during past flights. Accordingly, the weather data which is interpolated is obtained from a climate reanalysis and not from and a weather forecast, as it should be in a real-time implementation.

The present example represents an integration which could be used to increase the accuracy to which a trajectory may be reconstructed in a post-processing.

Within this context, the residual deviation of the processed baroaltimeter altitude is modeled as an augmented state. This is described in Section 8.1.1, based on Section B.3.

In Section 8.1.2, the measurement model for the integration of processed baroaltimeter altitude is explained. A computation of the associated measurement noise variance is then proposed in Section 8.1.3.

8.1.1 Dynamic Modeling of the Residual Errors as System Noise

The errors in the processed baroaltimeter altitude h_b may be integrated in a KF-based estimator as the sum of a bias term and another dynamic bias term with a time-discrete first-order GMP. A similar modeling is to be found in [41], as described in Section 3.2.

In order to do so, first, the mean error of the baroaltimeter altitude is computed and considered as the fixed bias, for each one of the investigated test flights. The PSD of the errors about the mean error is then plotted, for each flight. By visualizing the PSD of all flights in the same axes, an overbounding GMP may be found, as it is shown in Section 8.2.

An example of a discrete-time stationary first-order GMP overbounding a time-correlated process in the PSD domain is shown in Figure 8.2. Theory about this kind of GMPs is given in Appendix C.

By looking at Equation (C.5), it can be seen that for such a GMP, the PSD reaches its highest value, denoted by S_{max}, at $\omega \to 0$, or, equivalently, at $f \to 0$. This can also be observed from the red curve in Figure 8.2. Choosing a value for τ, and therefore for α, Equation (C.5) may be reverted, with $\omega = 0$, to obtain the standard deviation σ for the overbounding GMP from the maximum PSD of the actual process S_{max}:

$$\sigma = \sqrt{\frac{S_{max}(1-\alpha)}{(1+\alpha)\Delta t}} \tag{8.2}$$

With the chosen value of τ and the thereby computed σ, the PSD of the looked for GMP for a certain frequency range may be computed with Equation (C.5). By plotting this PSD in the same axes of the PSD plot of the actual process, it can be assessed whether or not the found GMP does effectively overbound the actual process. If not, the value of τ shall be changed and the newly resulting σ computed, till an overbounding GMP is found. This is therefore an iterative procedure.
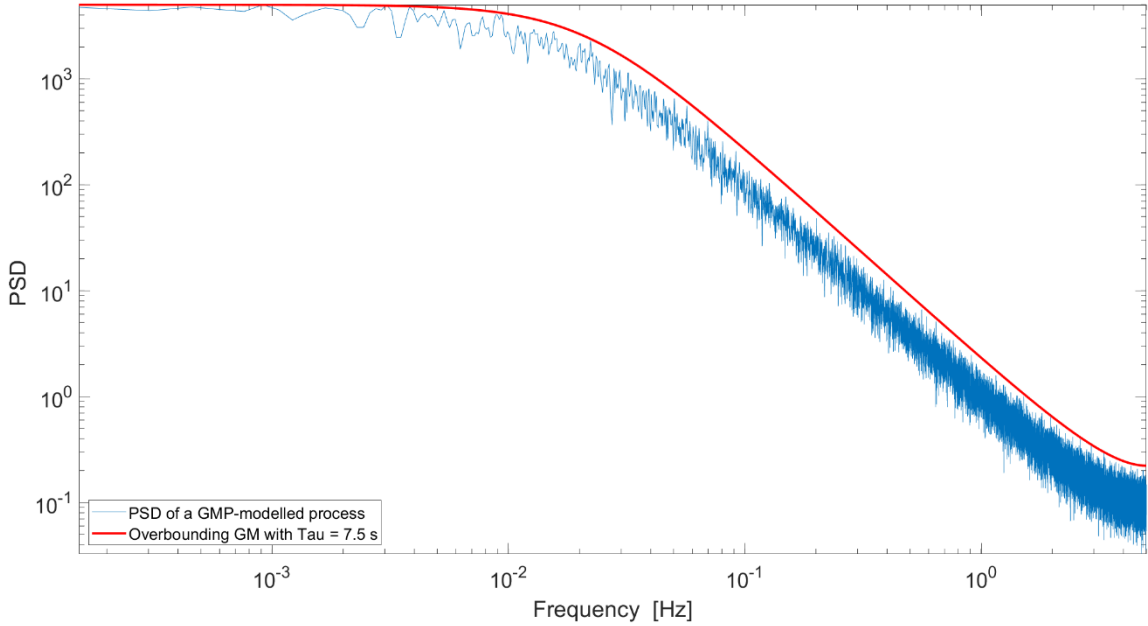
Figure 8.2: Example of PSD overbounding of a time-correlated process with a GMP

When this procedure was applied to the processed baroaltimeter altitude errors of each investigated flights, an overbounding GMP for all flights was sought by considering as S_{max} the maximum PSD among all flights.

High peaks in the PSD at low frequencies for all flights were found at common frequencies, which are thought to be related to aircraft dynamics effects. These peaks disappear when evaluating the PSD on the altitude plateaus of each flight.

By altitude plateau, a flight portion where the given altitudes, i.e., the pressure altitude and the GPS one, are approximately constant. It may be therefore inferred that the aforementioned peaks are due to some effects taking place during phases of altitude variations.

For this reason, it was chosen to consider only these portions and to apply the aforementioned procedure to these portions.

As a result, this modeling of the processed baroaltimeter altitude may be applied only on flight portions where altitude is approximately constant, such as in cruise flight.

The results of this procedure are shown in Section 8.2.

8.1.2 Measurement Model

The measurement model of processed baroaltimeter altitude within a LC KF-based estimator is formulated based on Equation (B.28) and on the example presented in Section B.3. Assuming an error-state KF-based estimator, with the state vector being

$$\mathbf{x} = \begin{pmatrix} \mathbf{x}_{INS} \\ \mathbf{x}_b \\ \vdots \end{pmatrix}, \quad \mathbf{x}_{INS} = \begin{pmatrix} \delta L \\ \delta \lambda \\ \delta h \\ \vdots \end{pmatrix}, \tag{8.3}$$

the measurement matrix partition related to the baroaltimeter aiding subsystem would be of the following kind

$$H_{b,j} = \left(\frac{\partial z_b}{\partial \delta L} \quad \frac{\partial z_b}{\partial \delta \lambda} \quad \frac{\partial z_b}{\partial \delta h} \quad \frac{\partial z_b}{\partial \mathbf{x}_b} \quad \mathbf{0} \right)_{\mathbf{x} = \widehat{\mathbf{x}}_j^-} . \tag{8.4}$$

As described in the previous section, the augmented states of the baroaltimeter subsystem, which are denoted by $\mathbf{x}_b$, may be a static bias $b_{b,s}$ and a dynamic bias $b_{b,d}$, whereby the latter may be assumed to have a first-order stationary GMP structure:

$$\mathbf{x}_b = \begin{pmatrix} b_{b,s} \\ b_{b,d} \end{pmatrix} . \tag{8.5}$$

Analogously to the example of Section 2.7.3, the KF measurement from the baroaltimeter subsystem is

$$z_b = \tilde{h}_b - \tilde{h} . \tag{8.6}$$

Due to the fact that $\tilde{h}_b$ is nothing else but $\tilde{h}_{w,\theta}$ and considering the conversion from pressure altitude to geodetic altitude described in Section 4.1 and the pitch-compensation of Section 7.1, it follows that

$$\tilde{h}_b = \frac{T_{ref}}{\alpha} \left[1 - \left(\frac{\tilde{p}}{p_{ref}} \right)^{\frac{kR_{dry}}{g_0}} \right] + Z_{g,ref}^{msl} + \Delta_{scale}(L, h) +$$
$$+ Z_g^{wgs84}(L, N(L, \lambda)) + A \, \theta + B + b_{b,s} + b_{b,d} ,$$

$$\text{if } 0 < \hat{Z}_g^{msl} \le 11 \text{ km} ;$$

$$\tag{8.7}$$

$$\tilde{h}_b = 11\text{km} - \frac{T_{11km} R_{dry}}{g_0} \ln \left(\frac{\tilde{p}}{p_{11km}} \right) + \Delta_{scale}(L, h) +$$
$$+ Z_g^{wgs84}(L, N(L, \lambda)) + A \, \theta + B + b_{b,s} + b_{b,d} ,$$

$$\text{if } 11 \le \hat{Z}_g^{msl} < 20 \text{ km} .$$

Then, since

$$h = Z_{g,ref}^{msl} + Z_g^{wgs84}(L, N(L, \lambda)) + \Delta_{scale}(L, h) , \tag{8.8}$$

the first of the expressions of Equation (8.7) can be rewritten as

$$\tilde{h}_b = \frac{T_{ref}}{\alpha} \left[1 - \left(\frac{\tilde{p}}{p_{ref}} \right)^{\frac{kR_{dry}}{g_0}} \right] + h + A \, \theta + B + b_{b,s} + b_{b,d} ,$$

$$\text{if } 0 < \hat{Z}_g^{msl} \le 11 \text{ km} ;$$

$$\tag{8.9}$$

Considering that T_{ref}, as well as Z_{ref}, T_{11km} and Z_{11km} all depend on the position and taking Equation (8.9) into account, Equation (8.6) can be further developed to

$$z_b = \frac{T_{ref}(L, \lambda, h)}{\alpha} \left[1 - \left(\frac{\tilde{p}}{p_{ref}(L, \lambda, h)} \right)^{\frac{kR_{dry}}{g_0}} \right] +$$

$$+ h + A\,\theta + B + b_{b,s} + b_{b,d} - \tilde{h},$$

$$\text{if } 0 < \hat{Z}_g^{msl} \leq 11 \text{ km} \; ;$$

$$(8.10)$$

$$z_b = 11\text{km} - \frac{T_{11km}(L, \lambda, h)R_{dry}}{g_0} \ln\left(\frac{\tilde{p}}{p_{11km}(L, \lambda, h)} \right) + \Delta_{scale}(L, h) +$$

$$+ Z_g^{wgs84}\big(L, N(L, \lambda)\big) + A\,\theta + B + b_{b,s} + b_{b,d} - \tilde{h} \; ,$$

$$11 \leq \hat{Z}_g^{msl} < 20 \text{ km} \; .$$

Considering Equations (B.30) and (8.8), Equation (8.29) may be further rewritten as

$$z_b = \frac{T_{ref}\big(\tilde{L} - \delta L, \tilde{\lambda} - \delta\lambda, \tilde{h} - \delta h\big)}{\alpha}$$

$$\left[1 - \left(\frac{\tilde{p}}{p_{ref}\big(\tilde{L} - \delta L, \tilde{\lambda} - \delta\lambda, \tilde{h} - \delta h\big)} \right)^{\frac{kR_{dry}}{g_0}} \right] +$$

$$+ A\,\theta + B + b_{b,s} + b_{b,d} - \delta h \; ,$$

$$\text{if } 0 < \hat{Z}_g^{msl} \leq 11 \text{ km} \; ;$$

$$(8.11)$$

$$z_b = 11\text{km} - \frac{T_{11km}\big(\tilde{L} - \delta L, \tilde{\lambda} - \delta\lambda, \tilde{h} - \delta h\big)R_{dry}}{g_0}$$

$$\ln\left(\frac{\tilde{p}}{p_{11km}\big(\tilde{L} - \delta L, \tilde{\lambda} - \delta\lambda, \tilde{h} - \delta h\big)} \right) - \tilde{Z}_g^{wgs84} +$$

$$+ A\,\theta + B + b_{b,s} + b_{b,d} \; ,$$

$$\text{if } 11 \leq \hat{Z}_g^{msl} < 20 \text{ km} \; .$$

The first of the derivatives in Equation (8.4) can therefore be computed with the chain rule as

$$\frac{\partial z_b}{\partial \delta L} = \frac{\partial z_b}{\partial T_{ref}} \frac{\partial T_{ref}}{\partial \delta L} + \frac{\partial z_b}{\partial p_{ref}} \frac{\partial p_{ref}}{\partial \delta L} \quad , \quad 0 < \hat{Z}_g^{msl} \leq 11 \text{ km} \; ;$$

$$(8.12)$$

$$\frac{\partial z_b}{\partial \delta L} = \frac{\partial z_b}{\partial T_{11km}} \frac{\partial T_{11km}}{\partial \delta L} + \frac{\partial z_b}{\partial p_{11km}} \frac{\partial p_{11km}}{\partial \delta L} \quad , \quad 11 \leq \hat{Z}_g^{msl} < 20 \text{ km} \; .$$

In an analogous way can the second of the derivatives in Equation (8.4) be computed. The third derivative, instead, is something more articulated:

$$\frac{\partial z_b}{\partial \delta h} = \frac{\partial z_b}{\partial T_{ref}}\frac{\partial T_{ref}}{\partial \delta h} + \frac{\partial z_b}{\partial p_{ref}}\frac{\partial p_{ref}}{\partial \delta h} - 1 \; ,$$
$$\text{if} \;\; 0 < \hat{Z}_g^{msl} \leq 11 \text{ km} \; ;$$

$$\frac{\partial z_b}{\partial \delta h} = \frac{\partial z_b}{\partial T_{11km}}\frac{\partial T_{11km}}{\partial \delta h} + \frac{\partial z_b}{\partial p_{11km}}\frac{\partial p_{11km}}{\partial \delta h} + \frac{\partial z_b}{\partial \tilde{Z}_g^{wgs84}}\frac{\partial \tilde{Z}_g^{wgs84}}{\partial \delta h} \; ,$$
$$\text{if} \;\; 11 \leq \hat{Z}_g^{msl} < 20 \text{ km} \; .$$

(8.13)

The third term on the right side of the second expression of Equation (8.13) may be approximated to

$$\frac{\partial z_b}{\partial \tilde{Z}_g^{wgs84}}\frac{\partial \tilde{Z}_g^{wgs84}}{\partial \delta h} = -\frac{\partial z_b}{\partial \tilde{Z}_g^{wgs84}}\frac{\partial \tilde{Z}_g^{wgs84}}{\partial h} = -(-1)\frac{\partial \tilde{Z}_g^{wgs84}}{\partial h} \approx -(-1)1 = 1 \qquad (8.14)$$

In Equation (8.12) (or (8.13)) the derivatives expressing the dependency of z_b on T_{ref}, p_{ref}, T_{11km} and p_{11km} can be easily computed based on the fact that

$$\frac{\partial z_b}{\partial \zeta} = \frac{\partial \tilde{h}_b}{\partial \zeta} = \frac{\partial Z_{p,w}}{\partial \zeta} \; , \qquad \zeta = \{T_{ref}, p_{ref}, T_{11km} , p_{11km}\} \; , \qquad (8.15)$$

where

$$\frac{\partial Z_{p,w}}{\partial T_{ref}} = \frac{1}{\alpha}\left[1 - \left(\frac{\tilde{p}}{p_{ref}}\right)^{\frac{R_{dry}\alpha}{g_0}}\right] \; ,$$

(8.16)

$$\frac{\partial Z_{p,w}}{\partial p_{ref}} = \frac{T_{ref}R_{dry}}{\tilde{p}\; g_0}\left(\frac{\tilde{p}}{p_{ref}}\right)^{\frac{R_{dry}\alpha}{g_0}+1} \; ,$$

and

$$\frac{\partial Z_{p,w}}{\partial T_{11km}} = -\frac{R_{dry}}{g_0}\; \ln\left(\frac{\tilde{p}}{p_{11km}}\right) \; ,$$

(8.17)

$$\frac{\partial Z_{p,w}}{\partial p_{11km}} = \frac{T_{11km}R_{dry}}{p_{11km}\; g_0} \qquad\qquad .$$

What is left is then to compute $\partial \zeta/\partial \delta L$, $\partial \zeta/\partial \delta \lambda$ and $\partial \zeta/\partial \delta h$, with $\zeta = \{T_{ref}, p_{ref}, T_{11km} , p_{11km}\}$, whereby it can be noticed that

$$\frac{\partial \zeta}{\partial \delta \chi} = -\frac{\partial \zeta}{\partial \chi}, \quad \chi = \{L, \lambda , h\} \; . \qquad (8.18)$$

The WGS84 spatial gradients of $T_{ref}, p_{ref}, T_{11km}$ and p_{11km} need therefore to be computed. Since, as described in Section 4.1, these quantities are obtained by interpolating weather datasets, their derivatives cannot be computed analytically. Instead, they

are computed through multidimensional interpolation as well.

This articulated procedure is described in the following paragraphs.

8.1.2.1 Computation of the ERA5 Weather Data Spatial Gradients

As anticipated, the gradients at a given point (and time) of a flight trajectory are computed based on multidimensional interpolation, similar to the one described in Section 4.1.

Before being able to interpolate, anyway, it is necessary to produce four-dimensional (4D) arrays for the gradients themselves. The structure of these 4D arrays needs to be similar to the structure of the arrays provided by the ERA5 dataset for temperature and geopotential altitude, as these are described in Section 4.1.

In particular, the arrays to be built based on the ERA5 weather data are six, with one for each of the following quantities: $\partial p_{ERA}/\partial L$, $\partial p_{ERA}/\partial \lambda$, $\partial p_{ERA}/\partial h$, $\partial T_{ERA}/\partial L$, $\partial T_{ERA}/\partial \lambda$, $\partial T_{ERA}/\partial h$, where p_{ERA} and T_{ERA} denote the pressures and temperature contained in the ERA5 data. These allow for the computation of the three-dimensional spatial gradients of T_{ref} and p_{ref}.

As explained in Section 4.1, in the ERA5 dataset on pressure levels, the temperature T_{ERA} and the geopotential altitude AMSL are given, indeed, on pressure levels. Thus, in order to numerically compute the $\partial p_{ERA}/\partial L$ and the $\partial p_{ERA}/\partial \lambda$ arrays, a 4D array for pressure on altitude levels must be built.

These height levels have been chosen to be 23 global surfaces of constant geopotential altitude AMSL, ranging from 0 to 11500 m. The number 23 was chosen as this is also the umber of the considered pressure levels in in Section 4.1. This choice was taken also because it simplified the algorithm needed for the gradients' interpolation, which is described in the following paragraphs.

A 4D array is generated in which, for each of the 23 altitude levels, the corresponding geopotential altitudes AMSL of that level around the world are given. The entries of these 4D arrays are the same for each hour, since geopotential altitude AMSL depends only on latitude, longitude, and altitude.

Analogously, a 4D array is generated for the pressure levels, in which, for each of the 23 pressure levels, the pressure of that level at the given hour is assigned to all the entries. This way—for each of the discrete latitudes, longitudes, and UTC hours of these 4D arrays—based on the geopotential altitudes AMSL given in the ERA5 dataset on pressure levels, the pressure can be logarithmically interpolated to the isoaltitude surfaces. This interpolation yields the needed 4D array for pressure on altitude levels, which is denoted by $p_{ERA,Z}$.

Again, as said in Section 4.1, this multidimensional interpolation, as well as the other ones which are described in the next paragraphs, are all done with the MATLAB® function interpn.

It shall be noted that this newly defined 4D array is actually not the ideal choice to then produce the $\partial p_{ERA}/\partial L$ and the $\partial p_{ERA}/\partial \lambda$ arrays, because for that we would like to have pressures on surfaces of constant geodetic altitude. Anyway, given the already

relatively high complexity and computational effort of the used algorithm, the presented method was assumed to be accurate enough for the present work.

In the following paragraphs, n_L, n_λ denote the number of discrete latitudes and longitudes on the regular global grid of the ERA5 dataset, described in Section 4.1. The number of UTC hours for which (the hourly) data is given in the 4D arrays extracted from the ERA5 data store is denoted by n_{hours}.

To numerically compute the 4D array $\partial p_{ERA}/\partial L$ the following is done:

$$\left.\frac{\partial p_{ERA}}{\partial L}\right|_{\lambda_r,h_s,hour_t} = \frac{\text{diff}\left(p_{ERA,Z}\big|_{\lambda_r,h_s,hour_t}\right)}{0.25°\pi/180} \ , \tag{8.19}$$

$$r = \{1,..,n_\lambda\}, \qquad s = \{1,..,23\}, \qquad t = \{1,..,n_{hours}\} \ .$$

In this section, being $\mathbf{u} = [u_1,...,u_i,...,u_N]^T$ a generic vector, the function diff is defined as the function that performs the following operation:

$$\text{diff}(\mathbf{u}) = [u_2 - u_1,...,u_i - u_{i-1},...,u_N - u_{N-1}]^T. \tag{8.20}$$

Analogously, for $\partial p_{ERA}/\partial\lambda$

$$\left.\frac{\partial p_{ERA}}{\partial\lambda}\right|_{L_u,h_s,hour_t} = \frac{\text{diff}\left(p_{ERA,Z}\big|_{L_u,h_s,hour_t}\right)}{0.25°\pi/180} \ , \tag{8.21}$$

$$u = \{1,..,n_L\}, \qquad s = \{1,..,23\}, \qquad t = \{1,..,n_{hours}\} \ .$$

By using the notation PL to refer to the considered ERA5 23 pressure levels, the 4D array $\partial p_{ERA}/\partial h$ is computed with

$$\left.\frac{\partial p_{ERA}}{\partial h}\right|_{L_u,\lambda_r,hour_t} = \frac{\text{diff}(PL)}{\text{diff}\left(Z_{ERA}\big|_{L_u,\lambda_r,hour_t}\right)} \ , \tag{8.22}$$

$$u = \{1,..,n_L\}, \qquad r = \{1,..,n_\lambda\}, \qquad t = \{1,..,n_{hours}\} \ ,$$

where Z_{ERA} denotes the ERA5 4D array of geopotential altitudes AMSL on the 23 pressure levels.

To compute the gradients of the ERA5 temperature, the step of interpolating temperature on isoaltitude surfaces is not necessary and the 4D arrays of the gradients are computed as follows:

$$\left.\frac{\partial T_{ERA}}{\partial L}\right|_{\lambda_r,PL_v,hour_t} = \frac{\text{diff}\left(T_{ERA}\big|_{\lambda_r,PL_v,hour_t}\right)}{0.25°\pi/180} \ , \tag{8.23}$$

$$r = \{1,..,n_\lambda\}, \qquad v = \{1,..,23\}, \qquad t = \{1,..,n_{hours}\} \ ,$$

$$\frac{\partial T_{ERA}}{\partial \lambda}\bigg|_{L_u,PL_v,hour_t} = \frac{\text{diff}\big(T_{ERA}|_{L_u,PL_v,hour_t}\big)}{0.25°\pi/180} \, ,$$

(8.24)

$$u = \{1,..,n_L\}, \qquad v = \{1,..,23\}, \qquad t = \{1,..,n_{hours}\} \, ,$$

and,

$$\frac{\partial T_{ERA}}{\partial h}\bigg|_{L_u,\lambda_r,hour_t} = \frac{\text{diff}\big(T_{ERA}|_{L_u,\lambda_r,hour_t}\big)}{\text{diff}\big(Z_{ERA}|_{L_u,\lambda_r,hour_t}\big)} \, ,$$

(8.25)

$$u = \{1,..,n_L\}, \qquad r = \{1,..,n_\lambda\}, \qquad t = \{1,..,n_{hours}\} \, .$$

Having now the six required 4D arrays, the interpolations to the flight trajectories' time, latitude, longitude, and altitude is possible. In other words, the three-dimensional spatial gradients of T_{ref} and p_{ref} can be computed.

Regarding the computation of the spatial gradients of T_{11km} and p_{11km}, it is assumed that their derivatives with respect the geodetic altitude, h, is zero. This is actually not necessarily true, since T_{11km} and p_{11km} are defined as the temperature and pressure at $Z_g^{msl} = 11$ km and not at $h = 11$ km. This approximation reduces the problem to compute the horizontal spatial gradients of T_{11km} and p_{11km}, i.e., their derivatives with respect to latitude and longitude.

The ERA5 pressure and temperature, i.e., the 4D arrays p_{ERA} and T_{ERA} are used to interpolate the pressure and temperature to $Z_g^{msl} = 11$ km for all the considered hours and on the global surface. This interpolation is similar to the one described in the previous paragraphs to obtain the 4D array for pressure on altitude levels, which was denoted by $p_{ERA,Z}$. The difference is that, instead of interpolating the pressure and temperature to many different altitude levels, they are now interpolate to just one altitude level, i.e., $Z_g^{msl} = 11$ km. The arrays obtained with this interpolation are therefore tridimensional and are denoted as $p_{ERA,11km}$ and $T_{ERA,11km}$.

To obtain the 3D array of the derivative of $T_{ERA,11km}$ with respect to latitude, the procedure represented by Equation (8.26) is followed.

$$\frac{\partial T_{ERA,11km}}{\partial L}\bigg|_{\lambda_r,hour_t} = \frac{\text{diff}\big(T_{ERA,11km}|_{\lambda_r,hour_t}\big)}{0.25°\pi/180} \, ,$$

(8.26)

$$r = \{1,..,n_\lambda\},, \qquad t = \{1,..,n_{hours}\} \, .$$

Analogously, for the 3D array of the derivative of $T_{ERA,11km}$ with respect to latitude the procedure represented by Equation (8.29) is followed.

$$\frac{\partial T_{ERA,11km}}{\partial \lambda}\bigg|_{L_u,hour_t} = \frac{\text{diff}\big(T_{ERA,11km}|_{L_u,hour_t}\big)}{0.25°\pi/180} \, ,$$

(8.27)

$$u = \{1,..,n_L\}, \qquad t = \{1,..,n_{hours}\} \, .$$

The procedure to obtain the 3D arrays of the derivatives of $p_{ERA,11km}$ with respect to latitude and longitude is similar to the one related to $T_{ERA,11km}$.

Having these four 3D arrays—$\partial p_{ERA,11km}/\partial L$, $\partial p_{ERA,11km}/\partial \lambda$, $\partial T_{ERA,11km}/\partial L$, $\partial T_{ERA,11km}/\partial \lambda$—a final interpolation to the trajectory's latitude, longitude and time yields the two-dimensional spatial gradients of T_{11km} and p_{11km}.

8.1.3 ERA5 Weather Data Uncertainty Propagation

The ERA5 climate reanalysis employs weather observations where possible. Based on such observations, this climate reanalysis uses a Numerical Weather Prediction (NWP) model to produce the estimates of meteorological quantities in the past in a temporally and spatially continuous way. The data is then given at 4D grid points, as described in Section 4.1. Like in a weather forecast, this method results in uncertainties in the data [17, 18].

More in detail, these uncertainties mostly take into account the physical parametrizations of the NWP model, the sea surface temperature and random uncertainties in the measurements. Moreover, the resulting uncertainties do not consider systematic model errors and are uncorrelated [17, 18].

Uncertainty estimates in the quantities provided in the ERA5 climate reanalysis on pressure levels are produced through a 10-member Ensemble of Data Assimilations (EDA) system [17, 18].

These uncertainty estimates are then provided in the ERA5 climate reanalysis on the same pressure levels, but with a different time resolution and a different spatial resolution on the horizontal plane. Indeed, the global regular latitude-longitude grid, on which the uncertainties are provided every three UTC hours, has a resolution of 0.5° [17, 18].

The reason for lower resolution is that ECMWF does not afford from a computational point of view to run EDAs with the same resolution of the ERA5 weather data production system. Nevertheless, ECMWF affirms that a higher resolution EDA would probably not provide enough supplementary information for the higher computational costs to be justified [17, 18].

In [18] it is recommended not to take the uncertainties values at face value, although they are declared useful to provide a relative uncertainties' estimate in terms of temporal and spatial distribution. That said, still in [18], ECMWF's authors state that this lower resolution dataset can be used for ERA5 uncertainty estimation.

In this work, the uncertainty in the weather data is propagated to the pressure altitude domain to produce an uncertainty in the processed baroaltimeter altitude. This uncertainty may then be used as the value for the corresponding measurement noise covariance matrix, which in this case degenerates into a scalar, as described in Section B.3.

In the same way ERA 5 temperature was interpolated—as described in Section 4.1—the uncertainty in ERA5 temperature is interpolated to the flight trajectories' time, latitude, and longitude and at the trajectories' altitude or at $Z_g^{\mathrm{msl}} = 11$ km to yield $\sigma_{T,ref}$ and $\sigma_{T,11km}$.

Uncertainty in pressure is obtained in a something more articulated way. The uncertainty in the ERA5 geopotential altitude AMSL is interpolated in the time and the horizontal space domains to produce a 2D matrix with the same dimensions of the ones described in Section 4.1. This matrix is referred to as the matrix of the geopotential altitudes AMSL uncertainties and contains the uncertainty in this quantity at each point along the trectory and at each of the 23 pressure levels.

One may then sum or deduct this matrix to or from the 2D matrix of the geopotential altitudes AMSL described in Section 4.1. Both options of considering the uncertainties in the ERA5 geopotential altitudes AMSL may then be used within a logarithmic interpolation analogous to the one described in Section 4.1.

The result of this interpolation is then an uncertainty-affected pressure along the flight trajectories. The absolute value of the difference between the pressure and the uncertainty-affected pressure along the flight trajectories is then assumed to be the pressure uncertainty.

The aforementioned option of deducting the matrix of the geopotential altitudes AMSL uncertainties from the corresponding matrix of geopotential altitudes AMSL was found to produce slightly higher (up to 3.7 %) pressure uncertainties with respect to the option of adding the two matrices. Because of this work's interest in a worst-case scenario, the first option is the one which was chosen for uncertainty propagation. The output of the procedure described in this paragraph is then the pressure uncertainty along the flight trajectories and is denoted by $\sigma_{p,ref}$.

Analogously to what said in the previous paragraph and in Section 4.1, by logarithmically interpolating the pressure levels to $Z_g^{\text{msl}} = 11$ km, then the pressure uncertainty along the flight trajectories but at $Z_g^{\text{msl}} = 11$ km is obtained and is denoted by $\sigma_{p,11km}$. For this interpolation, the difference between the matrix of the geopotential altitudes AMSL uncertainties and the matrix of the geopotential altitudes AMSL is used too.

Having described how the uncertainties for the ERA5 temperature and pressure $\sigma_{T,ref}$, $\sigma_{T,11km}$, $\sigma_{p,ref}$ and $\sigma_{p,11km}$, assumed as standard deviations, are obtained, the remaining part of this section focuses on their propgation.

Considering Equation (4.1), the propagated uncertainty in $Z_{p,w}$, denoted by σ_{Zpw}, is computed as

$$\sigma_{Zpw} = \sqrt{\left(\frac{\partial Z_{p,w}}{\partial T_{ref}}\sigma_{T,ref}\right)^2 + \left(\frac{\partial Z_{p,w}}{\partial p_{ref}}\sigma_{p,ref}\right)^2 + 2\frac{\partial Z_{p,w}}{\partial T_{ref}}\frac{\partial Z_{p,w}}{\partial p_{ref}}\sigma_{Tp,ref}} \quad ,$$

$$\text{if} \ \ 0 < \hat{Z}_g^{msl} \le 11 \ \text{km} \ \ ;$$

$$\sigma_{Zpw} =$$
$$= \sqrt{\left(\frac{\partial Z_{p,w}}{\partial T_{11km}}\sigma_{T,11km}\right)^2 + \left(\frac{\partial Z_{p,w}}{\partial p_{11km}}\sigma_{p,11km}\right)^2 + 2\frac{\partial Z_{p,w}}{\partial T_{11km}}\frac{\partial Z_{p,w}}{\partial p_{11km}}\sigma_{Tp,11km}} \ , \tag{8.28}$$

$$\text{if} \ \ 11 \le \hat{Z}_g^{msl} < 20 \ \text{km} \ \ ;$$

with

$$\sigma_{Tp,ref} = \rho_{ref} \; \sigma_{p,ref} \; \sigma_{T,ref} \qquad , \qquad (8.29)$$
$$\sigma_{Tp,11km} = \rho_{11km} \; \sigma_{p,11km} \; \sigma_{T,11km} \quad ,$$

where ρ_{ref} denotes the correlation coefficient between T_{ref} and p_{ref} and, analogously, ρ_{11km} denotes the correlation coefficient between T_{11km} and p_{11km}. These correlation coefficients are computed with the MATLAB® function corrcoef. The partial derivatives in Equation (8.28) are computed with Equations (8.16) and (8.17).

The uncertainty σ_{Zpw} in the weather-corrected pressure altitude $Z_{p,w}$ is in this work used as the measurement noise standard deviation. Equivalently, σ_{Zpw} is used as the square root of the only element of the measurement noise covariance matrix associated to the baroaltimeter navigation subsystem.

8.2 Results of the Residual Errors Dynamic Modeling

The altitude errors about the mean error, for each flight, are shown in Figure 8.3. The PSDs of these errors are shown in Figure 8.4
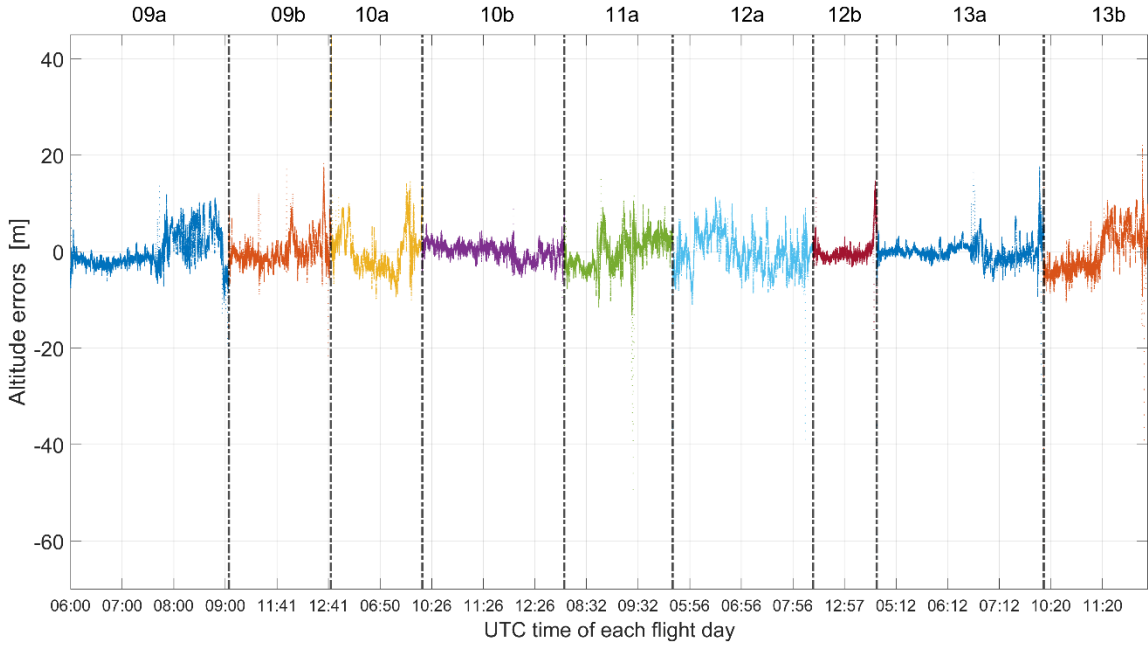
Figure 8.3: Altitude errors minus the mean error of each flight, during the central flight portions

81
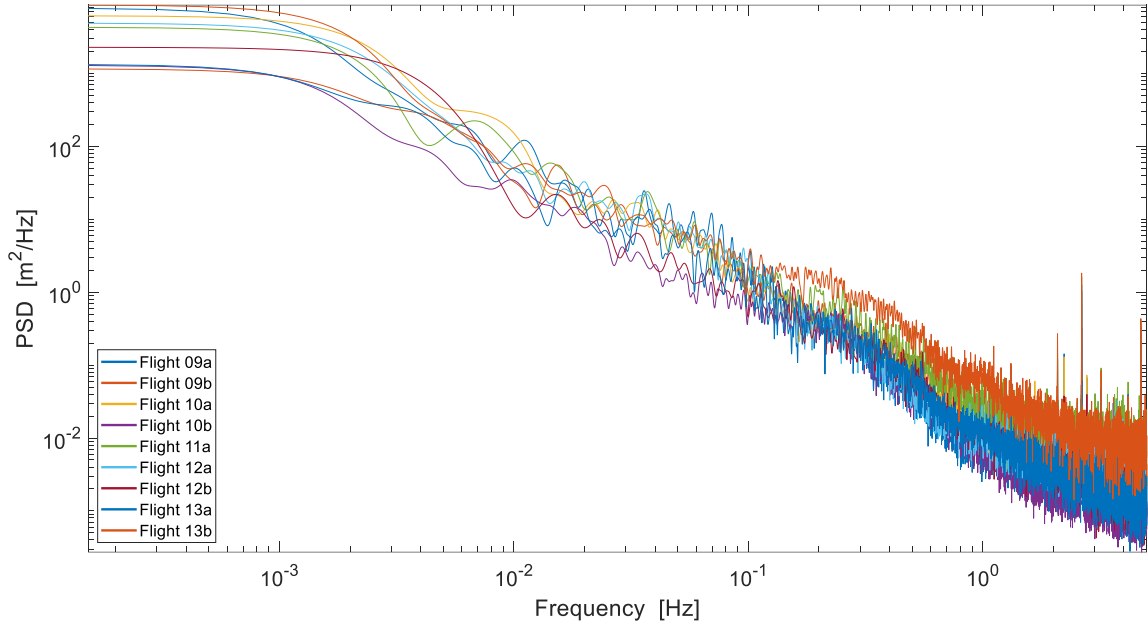
Figure 8.4: Power Spectral Density of the altitude errors minus the mean error of each flight, during the central flight portions

In Figure 8.4, the PSD spikes, which are mentioned in Section 8.1.1, can be noticed. Because of the PSD spikes, as anticipated in Section 8.1.1, the PSDs are analyzed only on the altitude plateaus, which are 22 The standard pressure altitude and the true geodetic altitude during these flight portions are shown in Figure 8.5 and Figure 8.6, respectively.
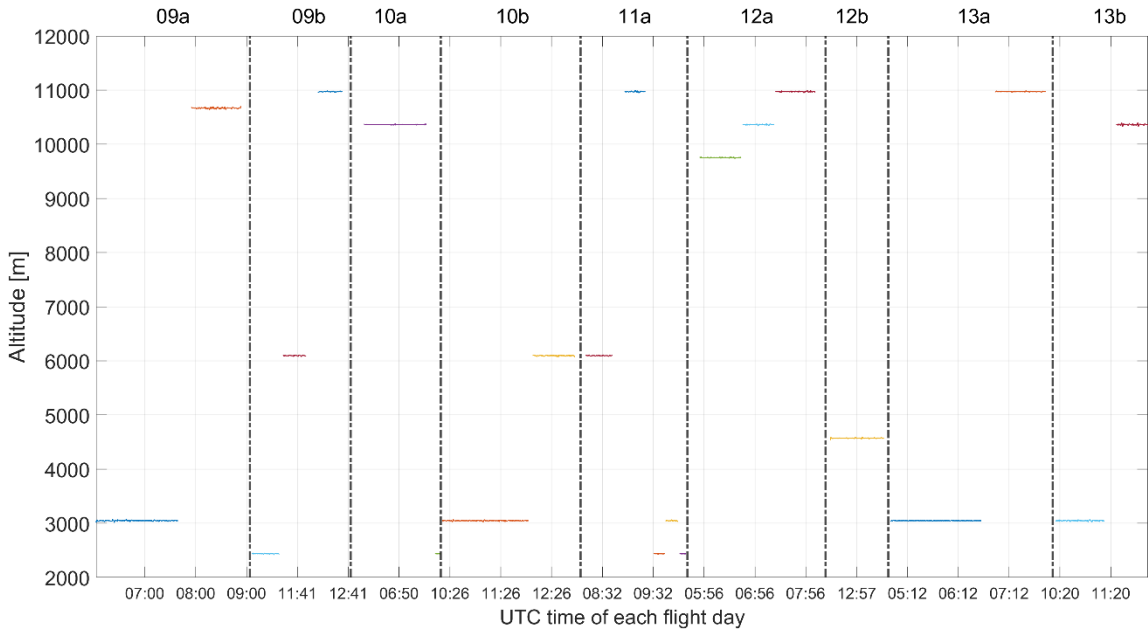
Figure 8.5: Standard pressure altitude on the altitude plateaus within the central flight portions
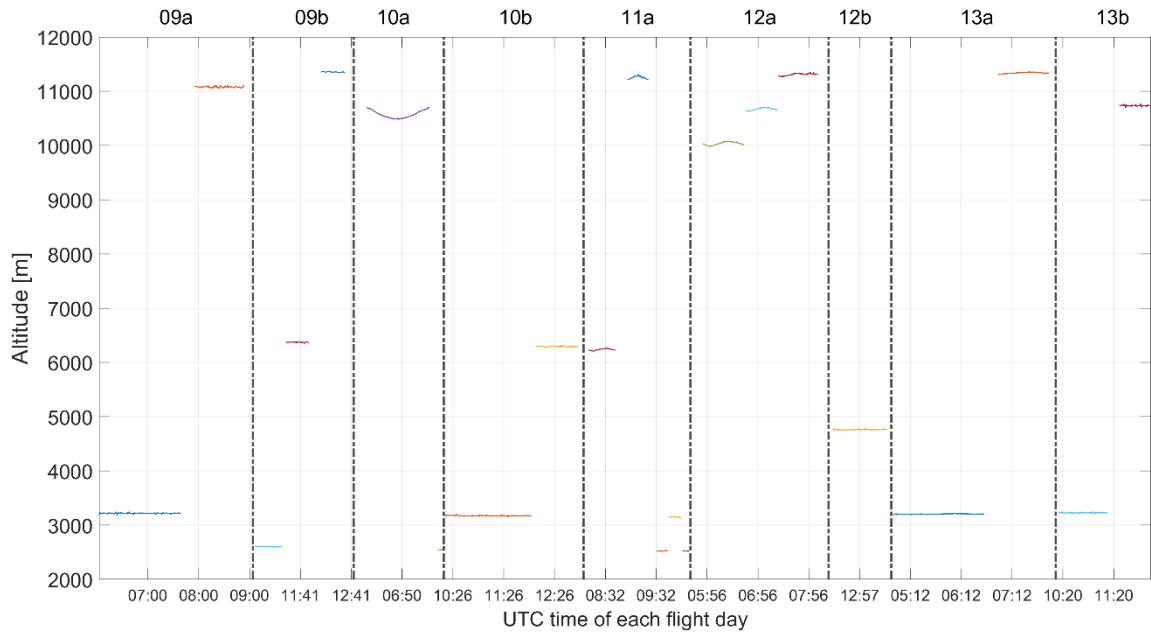
Figure 8.6: GPS altitude on the altitude plateaus within the central flight portions

As can be seen from these Figure 8.5 and Figure 8.6, flight 10a shows a peculiar geodetic altitude development along its main plateau, i.e., the one shown in violet. The reason for this stems from what is written about this flight in Section 6.1.

The residual errors on the altitude plateaus are shown in Figure 8.7. Their counterparts about the mean error on each plateau are shown in Figure 8.8.
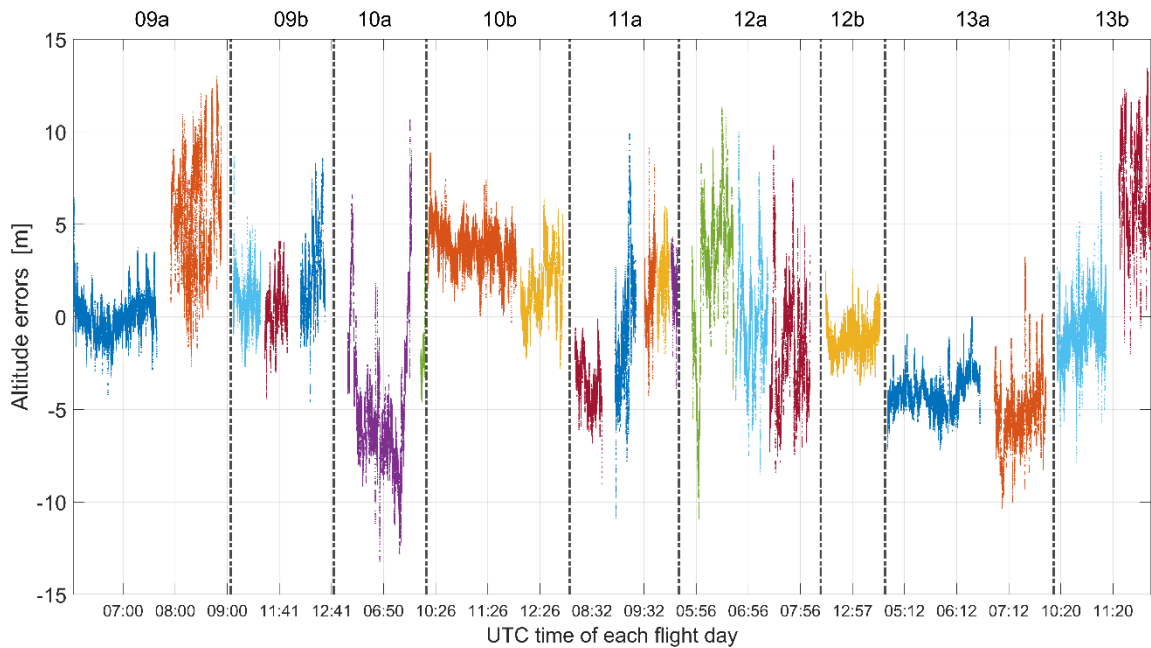
Figure 8.7: Altitude errors on the altitude plateaus within the central flight portions
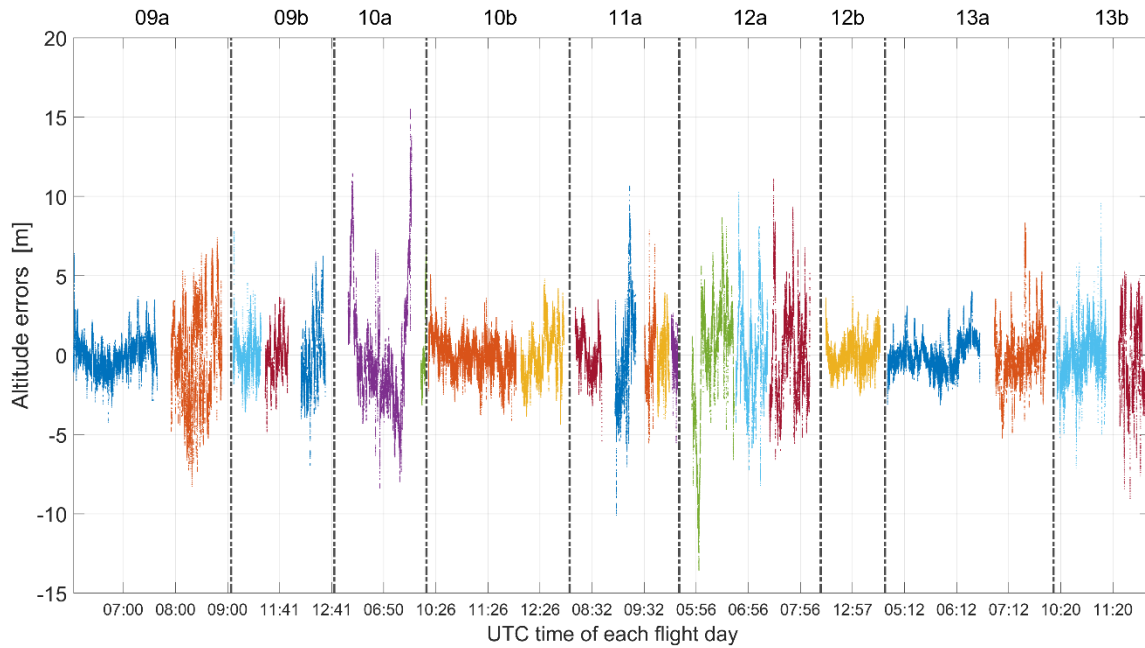
Figure 8.8: Altitude errors minus the mean error of each altitude plateau within the central flight portions

The mean errors on the plateaus range from approximately -4.83 to 7.05 m.

The PSDs of the residual errors about their mean values on the altitude plateaus are shown in Figure 8.9, in which no particularly high peak in the high-frequency-region can be seen in the PSDs. This allows for a relatively tight bound via a first-order GMP.
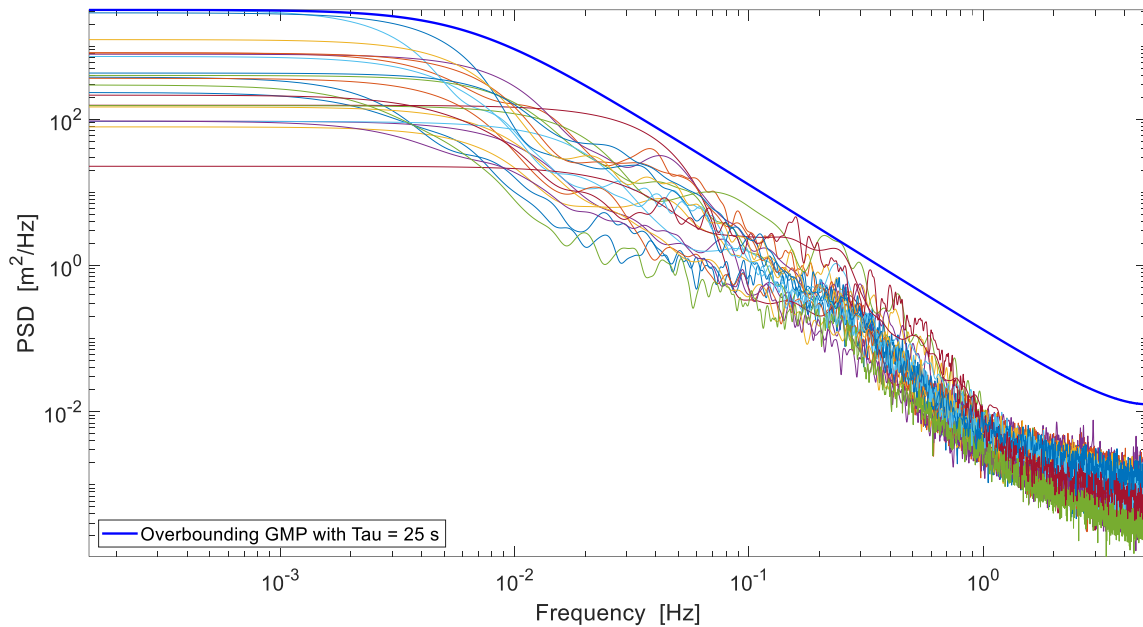
Figure 8.9: Power Spectral Density of the altitude errors minus the mean error of each altitude plateau within the central flight portions

The overbounding GMP is found to be defined by a time constant $\tau \cong 25$ s and q standard deviation $\sigma \cong 7.96$ m.

8.3   Spatial Gradients of the ERA5 Weather Data

The spatial gradient of the ERA5 pressure along the investigated flights' trajectories is shown in Figure 8.10. In particular, the derivative of pressure with respect to geopotential altitude AMSL is shown in the upper plot in this figure. The derivative with respect to latitude and longitude are shown in the middle and lower plots, respectively.

By comparing the variation of pressure with altitude with the true geodetic altitude profiles depicted in Figure 6.2, a clear correlation between these two quantities may be noticed. Regarding the peculiar shape of the curve representing the derivative of pressure with latitude, this may be explained with what is written about this flight in Section 6.1.

Figure 8.11 shows the spatial gradient of the ERA5 temperature along the investigated flights' trajectories. Considering the upper plot in this figure, it can be seen that the values of the temperature derivative with respect to the geopotential altitude AMSL appear to be quite in accordance with the value that the ISA assigns to this derivative for geopotential altitudes AMSL between 0 and 11 km. This value is the temperature lapse rate, introduced in Section 2.2.1 and equal to 6.5 K km^{-1}, taken with sign minus.
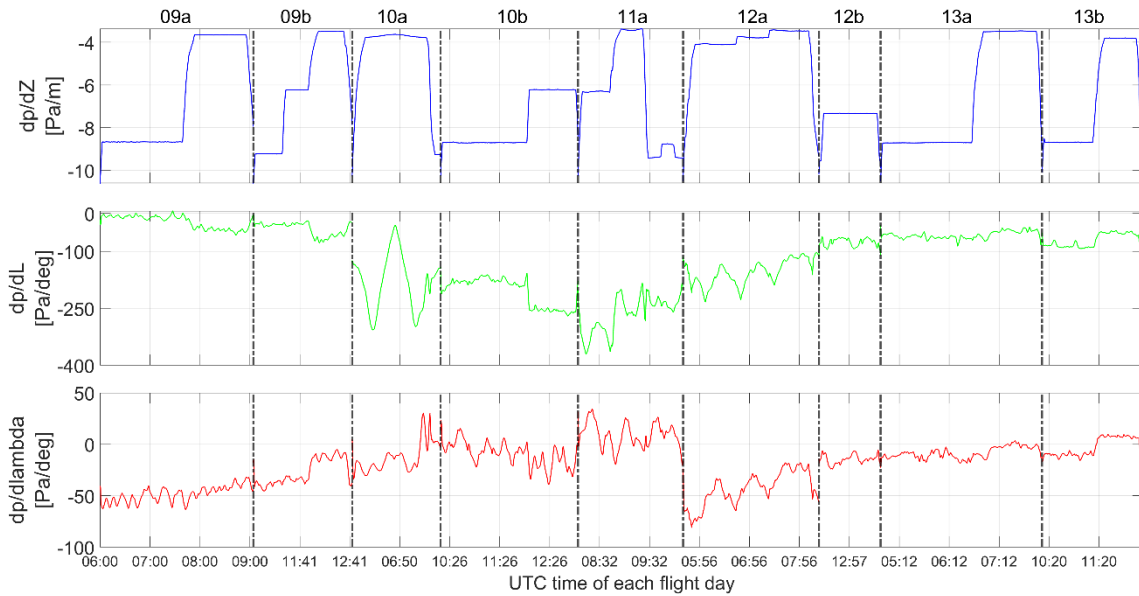
Figure 8.10: Spatial gradient of the ERA5 pressure, interpolated to the test flights' trajectories, during the central flight portions

By comparing the aforementioned plot with the true geodetic altitude profiles depicted in Figure 6.2, it can be seen that, generally, the absolute value of temperature variation with altitude decreases with increasing altitude. This is actually shown not to be the case for flights 09a and 12b.
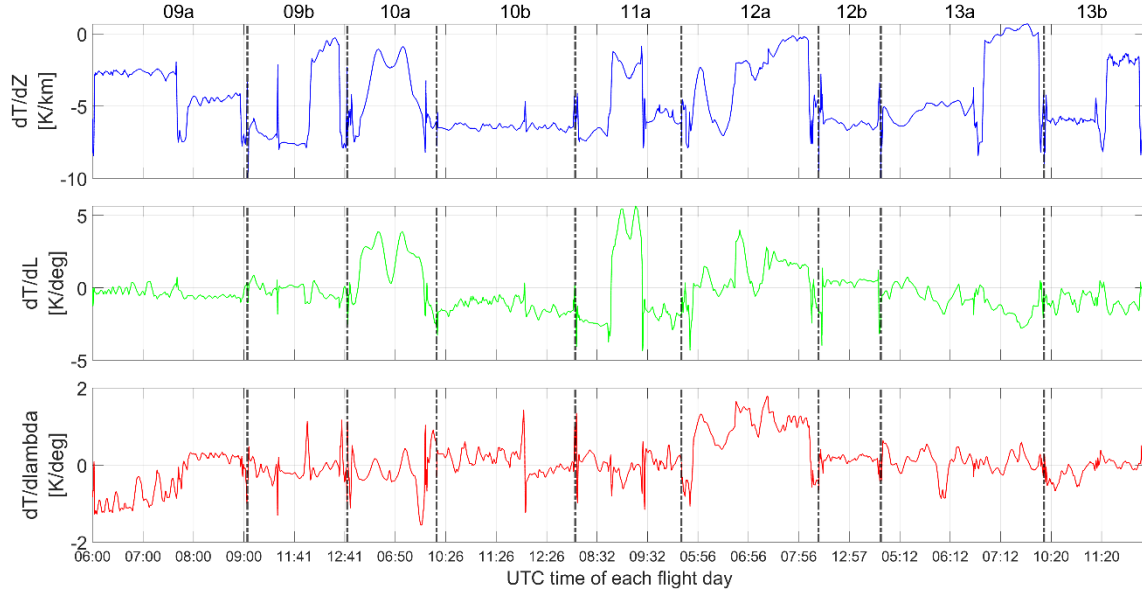
Figure 8.11: Spatial gradient of the ERA5 temperature, interpolated to the test flights' trajectories, during the central flight portions

This tendency for the other flights is in accordance with what the ISA implies. Indeed, according to the ISA, after decreasing linearly with altitude until $Z_g^{msl} = 11$ km, the atmospheric temperature keeps the constant value of 216.65 K until $Z_g^{msl} = 20$ km. Since the actual temperature profile is unlikely to be so unsteady, it may be inferred that the magnitude of the temperature derivative's with respect to altitude gradually decreases when approaching geopotential altitudes close to 11 km.

The derivatives of the ERA5 pressure at $Z_g^{msl} = 11$ km with respect to latitude and longitude along the test flights' trajectories are shown in the upper and lower plot, respectfully, of Figure 8.12.
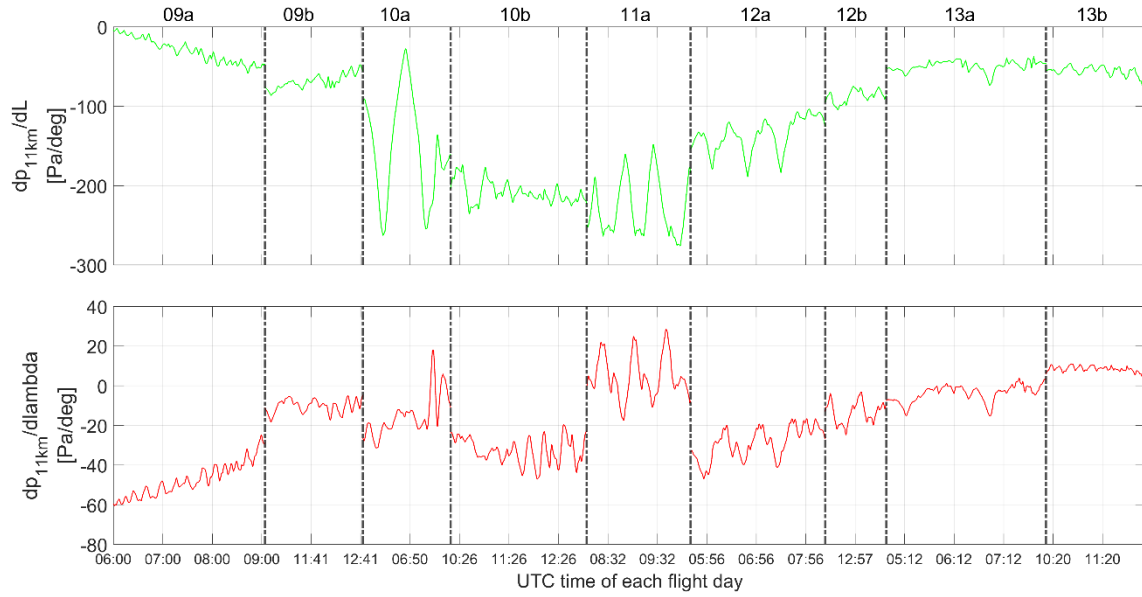
Figure 8.12: Derivatives of the ERA5 pressure at Z_g^{msl}=11km with respect to latitude and longitude, interpolated to the horizontal projections of the test flights' trajectories, during the central flight portions

Analogously to Figure 8.12, the derivatives of the ERA5 temperature at $Z_g^{msl} = 11$ km with respect to latitude and longitude along the test flights' trajectories are shown in Figure 8.13.
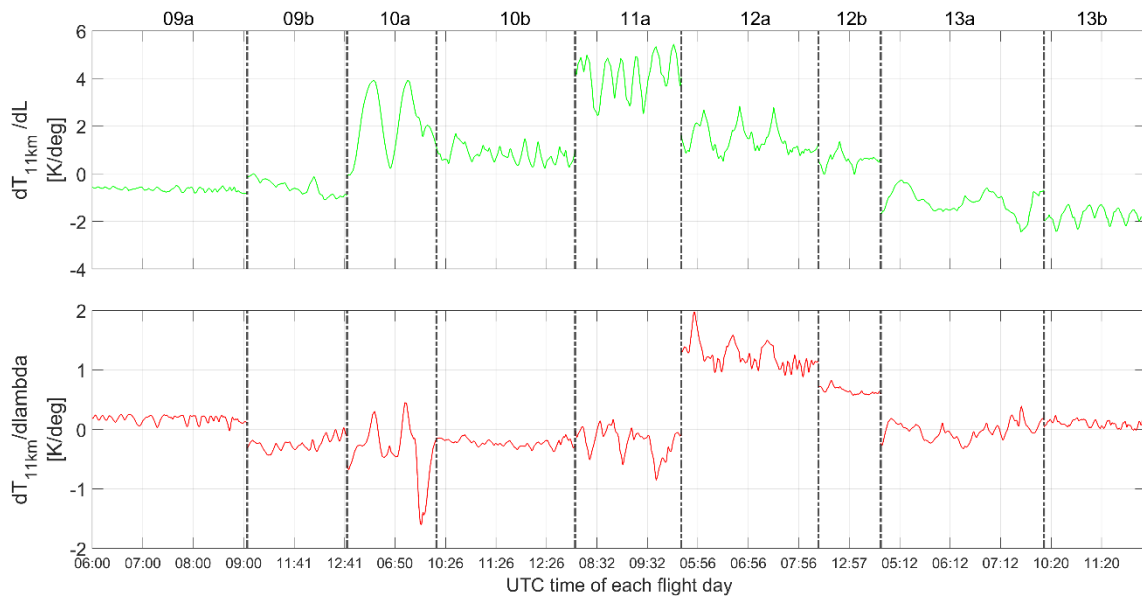
Figure 8.13: Derivatives of the ERA5 temperature at Z_g^{msl}=11km with respect to latitude and longitude, interpolated to the horizontal projections of the test flights' trajectories, during the central flight portions

8.4   Results of ERA5 Uncertainty Propagation

The uncertaintites in the ERA5 pressure and temperature along the trajectories of the considered flights are shown in the upper and lower plots, respectfully, of Figure 8.14.
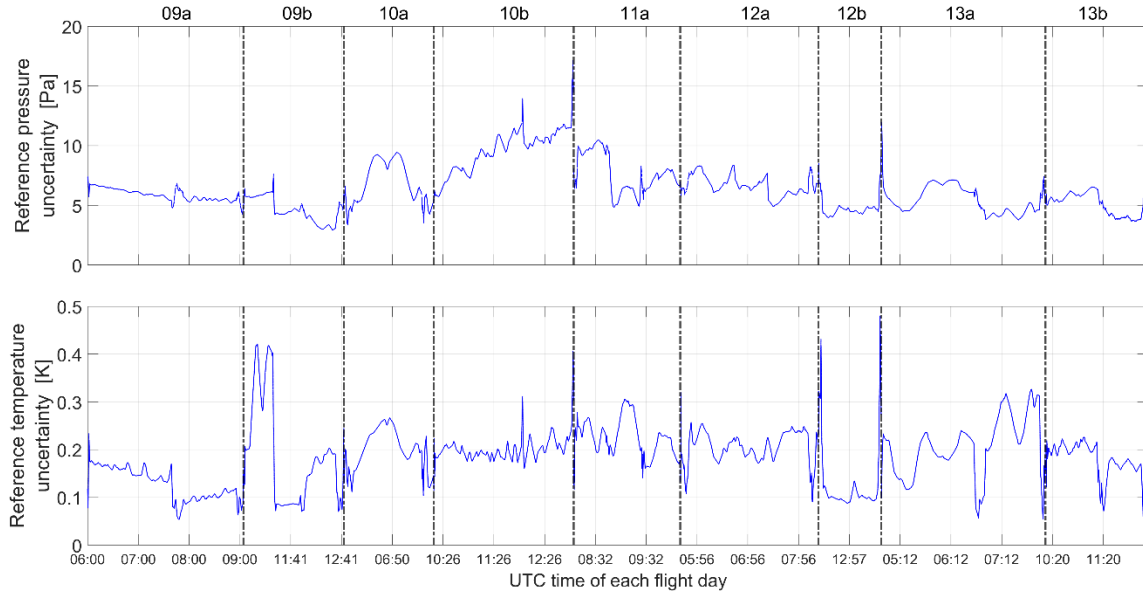
Figure 8.14: Uncertainties in the ERA5 pressure and temperature, interpolated to the test flights' trajectories, during the central flight portions

Analogously to Figure 8.14, the uncertaintites in the ERA5 pressure and temperature at Z_g^{msl}=11km along the test flights' trajectories are shown in Figure 8.15.
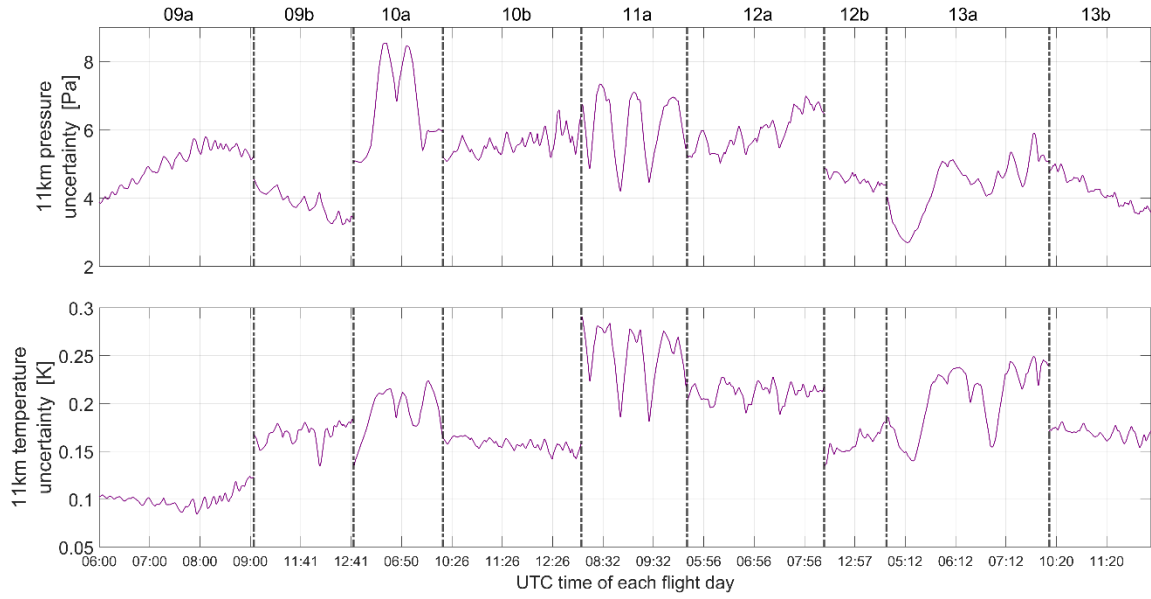
Figure 8.15: Uncertainties in the ERA5 pressure and temperature at Z_g^{msl}=11km, interpolated to the horizontal projections of the test flights' trajectories, during the central flight portions

The propagation of this uncertainty in the pressure altitude domain along the flight trajectories, that is performed through Equation (8.28), is shown in Figure 8.16.
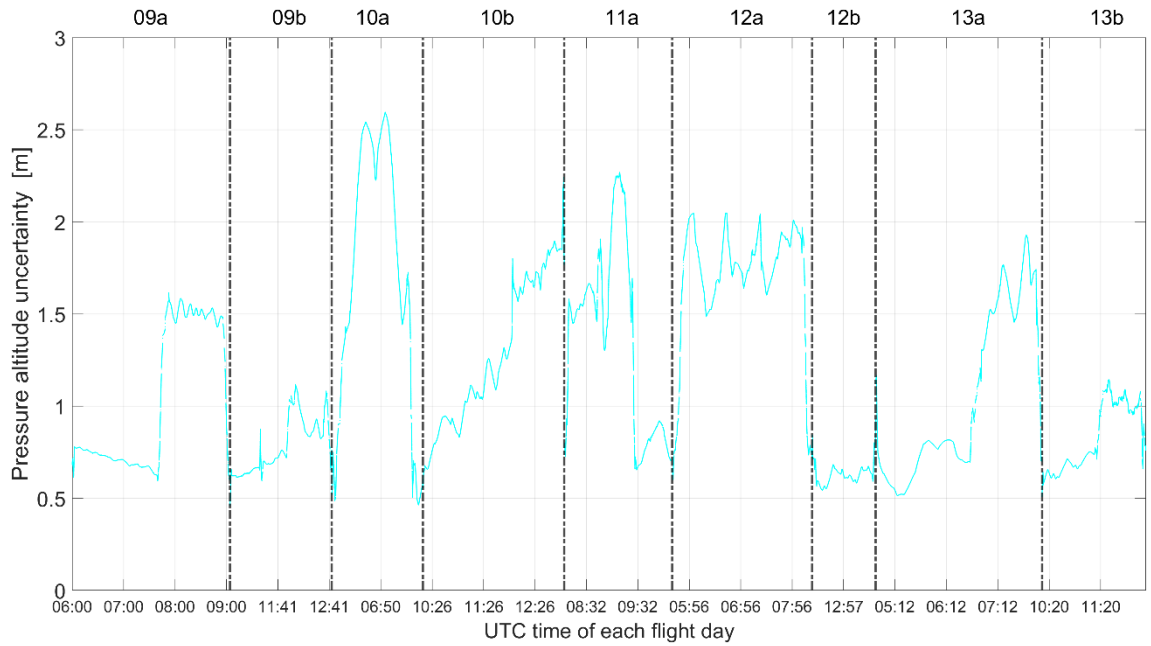
Figure 8.16: Propagated weather-corrected pressure altitude uncertainty during the central flight portions

89

9   Conclusions

This work assesses the accuracy in the approximation of true geodetic altitude that is achieved by two different methods of obtaining geodetic altitude from, among others, airborne pressure measurements.

One of these two geodetic altitude computation methods relies on the Blanchard algorithm for orthometric altitude computation. The consideration of the geoid undulations allows for a conversion from orthometric altitude to geodetic altitude.

The second method is based on the pressure altitude equation, in which external weather data is entered as reference. This pressure altitude is in this thesis referred to as the weather-corrected pressure altitude. Weather data is extracted from the ECMWF ERA5 climate reanalysis [17] via a multidimensional interpolation, i.e., by interpolating in the horizontal and vertical space domains and in the time domain. The interpolation is done through the true trajectory, which was provided by post-processed GPS data.

The consideration of the geoid undulations and the difference between the geopotential and geometric altitude scales enables a conversion from the weather-corrected pressure altitude to geodetic altitude.

This work shows that the geodetic altitude obtained from the weather-corrected pressure altitude is more accurate in comparison with the geodetic altitude obtained from the Blanchard algorithm. Only the former is therefore considered in the sections of the thesis which deal with the error modelling of the geodetic altitude measurements.

This thesis derives a linear model relating the errors in the geodetic altitude obtained with the weather-corrected pressure altitude to the aircraft pitch attitude angle. This allows to reduce the absolute value of the mean error in the geodetic altitude measurements, as well as the errors' standard deviation. Indeed, the mean and the standard deviation of the residual errors in geodetic altitudes after the so-called pitch-compensation are 0.1 and 4.1 m. Their counterparts before the pitch-compensation are -4.6 and 6.4 m, instead.

A gaussian distribution overbounding the residual geodetic altitude errors' distribution is found. This may be suitable for integrated navigation applications based on snapshot algorithms in which these geodetic altitude measurements could be incorporated.

A first-order GMP is herein derived to model the residual geodetic altitude errors on the altitude plateaus, i.e., on the flight portions during which the altitude is approximately constant. This model may be employed when incorporating these geodetic altitude measurements in integrated navigation systems based on sequential estimators. Such a navigation systems is provided as an example in this thesis. Within this example

it is also shown how the weather data would be considered in the measurement model and measurement noise standard deviation.

Apart from the aforementioned GPS post-processed data, the analyses of this thesis are based on measurements recorded by the Flight Management System during more than 20 flight hours performed with the Dassault Falcon 20-E5 aircraft within a DLR flight tests campaign. The fact that the investigated flights covered a broad spectrum of altitudes allowed to properly address the impact of altitude within the presented methodology and derived error model parameters.

10 Outlook

As explained in Section 5.2, because of the unavailability of the actual pressure measurements carried out during the investigated flights, the analyses performed within this thesis are based on retrieved pressure measurements.

This means that the original pressure measurements may be actually more or less different with respect to these retrieved ones. Some smoothing and some corrections may indeed have been performed during the flights before the raw pressure measurements were entered to the ADC to compute the standard pressure altitudes. This may of course have had some unexpected effects on the results of this work's analyses. In order to avoid these effects, future investigations should be carried out based on the actual pressure measurements. This would require a new structuring of the DLR software storing real-time airborne measurements.

The weather data that was employed within this work is obtained from the ERA5 climate reanalysis on pressure levels, as described in Section 4.1. Improvements in the approximation of the true geodetic altitude may be achieved by using ERA5 weather reanalysis on model (a.k.a. hybrid) levels [25].

The model levels are defined in such a way that, the closer to the Earth's surface, the more they follow the orography. Conversely, the farther away from the Earth's surface, the more they represent isobar surfaces. The ERA5 reanalysis is given on (up to) 137 model levels and there are 64 levels from a 1013.25 hPa to approximately 200 hPa. This means that, in comparison to the 23 pressure levels from 1000 to 200 hPa, the resolution in the vertical channel is higher than in the ERA5 on pressure levels.

In this work, the obtained geodetic altitude measurements are compared to the GPS post-processed altitude to assess their accuracies. In doing so, the lever arm between the GPS antenna and the pressure ports is ignored. Therefore, an improvement in the accuracy assessment may be made possible by considering this lever arm.

The gaussian distribution described in Chapter 7 for the overbounding of the residual geodetic altitude errors may in future be employed for incorporating the corresponding geodetic altitude measurements in integrated navigation systems based on Snapshot algorithms. This would allow to assess the robustness of this bounding. In case this was guaranteed, a tighter bounding error model may be found with, e.g., unimodal distributions.

Analogously, the efficacy of the dynamic error modeling based on a first-order GMP

described in Chapter 8 may be tested within an integrated navigation system based on a sequential estimator. This may be, for example, similar to the example proposed in Chapter 8.

Further research may be needed to find the reason for the low-frequency peaks in the PSDs of the residual geodetic altitude errors during climbing and descending flight phases, which are shown in Chapter 8. This may then ultimately allow for an efficient modeling of the residual errors in these flight phases too.

Error models similar to the ones derived for the geodetic altitude obtained from the weather-corrected pressure altitude may in future be derived for the geodetic altitude obtained from the Blanchard algorithm too.

A. Further ADC Equations

The equations for standard pressure altitude and the ones for baro-correction, i.e., Equations from (2.25) to (2.27), are typically implemented within Air Data Computers (ADC), that are software component of Air Data Systems (ADS) [51].

This appendix presents some of the other equations which are traditionally part of ADCs that are relevant in this work. Since these equations are, as said, relevant and yet not so crucial as the equations related to the various concepts related to altitude, these equations will not be demonstrated.

The Mach number, M, is defined as the ratio between the aircraft's true airspeed, TAS, that is the modulus of the velocity vector with respect to the wind vector, and the speed of sound c_s [51]:

$$M = \frac{TAS}{c_s} \, ,$$ (A.1)

In turn, the speed of sound in the air, for normal conditions of pressure and temperature, is related to temperature through [51]

$$c_s = \sqrt{1.4 \ R_{dry} T} \, .$$ (A.2)

The subsonic Mach equation relates the Mach number to impact pressure, q_c, and static air pressure p—that in this thesis as well as commonly is simply called air pressure—as

$$\frac{q_c}{p} + 1 = \left(1 + \frac{M}{5}\right)^{7/2} \, ,$$ (A.3)

whereby impact pressure, that in an ADS is usually measured with a differential pressure transducer, is the difference between total and static air pressure [51].

Calibrated is a further quantity typically computed by ADCs according to the following equation:

$$CAS = c_{s0} \ \sqrt{5\left[\left(\frac{q_c}{p} + 1\right)^{2/7} - 1\right]} \, ,$$ (A.4)

where c_{s0} is the standard MSL speed of sound, meaning the speed of sound obtained by inserting the ISA standard MSL into Equation (A.2).

B. Kalman Filtering

In this appendix, the working principles of Kalman filtering, and in particular of a Loosely-coupled Kalman Filter, are presented.

Kalman filtering is employed in navigation for integration (or fusion) of various navigation subsystems and calibration of INS [9]. The Kalman filter was developed by R. E. Kaman for time-discrete linear systems [52]. This version of the Kalman filter is herein referred to as the conventional one and it is described in Section B.1.

Due to the fact that in navigation the systems are often non-linear, Section B.2 focuses on one of the Kalman filter versions capable of handling such systems [9], i.e., the Extended Kalman filter (EKF).

In Section B.3, a KF with an error-state implementation and a Loosely-Coupled architecture is presented.

B.1   Conventional Kalman Filter

The Kalman filter components can be grouped in five main blocks: the algorithm itself, the measurement model, the measurements and covariances associated to them, the system model, the system states and their covariances [9].

The state vector $\mathbf{x}$ contains the system states, which estimated by the Kalman filter algorithm. The covariance matrix $\mathbf{P}$—described in Section B.1.2—contains the covariances associated to the state vector's estimates. Section B.1.1 is devoted to the system model, which describes how the system states evolve with time.

In Section B.1.4, the measurement vector $\mathbf{z}$, which is the collection of simultaneous measurements of some system properties, is presented. The measurement model—presented in Section B.1.3—describes the dependency of this vector on the state vector $\mathbf{x}$ [9]. The measurement vector is affected by measurement noise too. In Kalman filtering, this noise is assumed to be white and its distribution is often assumed to be gaussian, with a given variance [9]. The covariances associated to the various measurement noise components appear in the measurement noise covariance matrix $\mathbf{R}$, as described in Section B.1.4.

The system model is affected by noise too, in the sense that such noise embodies unknown states' fluctuations which make the states differ over time from their system model-based predictions. This has the consequence that the states' variances need to be increased over elapsed time to take into account these unknown variations. Regarding the measurement noise, in Kalman filtering system noise is assumed to be of white na-

ture and it is generally modeled to be gaussian [9]. Such assumptions are a remarkable limitation of Kalman filtering, as they do not find a general justification, and are yet necessary.

Section B.1.5 is devoted to the Kalman filter algorithm, which via the measurement vector and the system and measurement model attains optimal states' estimates. Indeed, it can be shown that the Kalman filter provides optimal estimation performance, i.e., that the sum of the mean-square errors in all states' estimates is minimal [52]. This is true whenever the system is linear and the measurement as well as the system noise are white and gaussian.

In order to compensate for the limitations stemming from these assumptions and thus to overbound the real system's behavior, enough noise must be modeled [9].

An Kalman filter algorithm's iteration may be divide into two phases: the propagation phase and the measurement update. In the former, the states and the error covariance matrix are forwarded in time according to the system model, while in the latter, they are corrected by the measurements.

These main Kalman filter components of are presented in a mathematical way in turn in the next sections.

B.1.1 System Model

According to the Kalman filter assumptions, the time derivatives of the state vector $\mathbf{x}$ is a linear functions of the state vector itself and of the white system noise vector $\mathbf{w}_s$:

$$\dot{\mathbf{x}}(t) = \mathbf{F}(t)\mathbf{x}(t) \ + \mathbf{G}(t)\mathbf{w}_s(t) \ \ , \tag{B.1}$$

where $\mathbf{F}(t)$ and $\mathbf{G}(t)$ are the system matrix and the system noise distribution matrix at time t, respectively [9]. Each of the elements of $\mathbf{w}_s$ represents an independent random noise source whose distribution is additionally assumed to be of the zero-mean symmetric kind, such as the Gaussian distribution [9]. The application of the expectation operator $\mathrm{E}(\bullet)$ to Equation (B.1) yields [9]

$$\mathrm{E}\big(\dot{\mathbf{x}}(t)\big) = \frac{\partial}{\partial t}\hat{\mathbf{x}}(t) = \mathbf{F}(t)\hat{\mathbf{x}}(t) \ \ , \tag{B.2}$$

with the caret ^ denoting the estimate. The expectation of $\mathbf{w}_s(t)$ is zero, owing to the fact that the system noise sources are assumed to have a zero mean.

It can be shown that the approximated solution of the differential Equation (B.2), assuming $\mathbf{F}$ to be constant over the interval τ_s, provides the state vector estimate at time t in dependency of the state vector estimate at a time $t - \tau_s$ [9]:

$$\hat{\mathbf{x}}(t) \approx \exp(\mathbf{F}(t)\tau_s)\,\hat{\mathbf{x}}(t - \tau_s) \ . \tag{B.3}$$

In the case of a time-invariant system model, the approximation is exact. The discrete Kalman filter models the current states' estimates as linearly dependent on their previous values:

$$\hat{\mathbf{x}}_j^- = \mathbf{\Phi}_{j-1}\hat{\mathbf{x}}_{j-1}^+ \tag{B.4}$$

with

$$\begin{aligned}
\hat{\mathbf{x}}_j &:= \hat{\mathbf{x}}(t_j) \\
\hat{\mathbf{x}}_{j-1} &:= \hat{\mathbf{x}}(t_j - \tau_s) \\
\mathbf{\Phi}_{j-1} &:= \exp(\mathbf{F}_{j-1}\tau_s)
\end{aligned} \quad , \tag{B.5}$$

where the subscript j denotes the Kalman filter iteration [9] and the superscript $-$ denotes a quantity at the end of the propagation phase. In contrast, the superscript $+$ denotes a quantity after the measurement update phase has ended.

Assuming that data is available at the time interval τ_s extrema, that is at t_j and t_{j-1}, but not between them, then $\mathbf{F}_{j-1}$ may be computed as $\frac{1}{2}\big(\mathbf{F}(t) + \mathbf{F}(t - \tau_s)\big)$. The matrix $\mathbf{\Phi}_{j-1}$, known as the transition matrix, is usually computed by means of a power-series expansion of $\mathbf{F}$ [9].

Similarly to the states estimates, the true states $\mathbf{x}_j$ may be expressed as functions of their previous values by integrating (B.1) over τ_s:

$$\mathbf{x}_j = \mathbf{\Phi}_{j-1}\mathbf{x}_{j-1} + \mathbf{\Gamma}_{j-1}\mathbf{w}_{s,j-1} \; , \tag{B.6}$$

where $\mathbf{F}(t)$ and $\mathbf{G}(t)$ are assumed constant over τ_s [9] and $\mathbf{w}_{s,j-1}$ and $\mathbf{\Gamma}_{j-1}$ denote the discrete system noise vector and the discrete system noise distribution matrix, respectively. Their products is

$$\mathbf{\Gamma}_{j-1}\mathbf{w}_{s,j-1} = \int_{t_j-\tau_s}^{t_j} \exp\Big(\mathbf{F}_{j-1}(t_j - t')\Big)\mathbf{G}_{j-1}\mathbf{w}_s(t')\mathrm{d}t' \; , \tag{B.7}$$

where $\mathbf{G}_{j-1}$ is calculated analogously to the computation of $\mathbf{F}_{j-1}$ [9].

B.1.2 State Vector and Covariance

A Kalman filter may estimate absolute system properties—such as the position, in navigation—or errors in the system's measurements, like the position measurement from an INS. The former case is referred to as total-state implementation, while the latter as error-state implementation.

The difference between the true state vector and its estimate is known as state vector residual $\delta\mathbf{x}$:

$$\delta\mathbf{x} = \mathbf{x} - \hat{\mathbf{x}} \; . \tag{B.8}$$

In an error-state implementation, $\delta\mathbf{x}$ denotes the residual errors in the system after the state estimates have been employed to correct it [9]. The error covariance matrix $\mathbf{P}$ is the covariance of the state vector:

$$\mathbf{P} = \mathrm{E}\big((\hat{\mathbf{x}} - \mathbf{x})(\hat{\mathbf{x}} - \mathbf{x})^\mathrm{T}\big) = \mathrm{E}(\delta\mathbf{x}\delta\mathbf{x}^\mathrm{T}) \; . \tag{B.9}$$

B.1.3 Measurement Model

The measurement vector $\mathbf{z}(t)$ is assumed by the conventional Kalman filter to be linearly dependent, via the measurement matrix $\mathbf{H}$, both on the state vector $\mathbf{x}(t)$ and the white measurement noise vector $\mathbf{w}_m$:

$$\mathbf{z}(t) = \mathbf{H}(t)\mathbf{x}(t) \; + \mathbf{w}_m(t) \; . \tag{B.10}$$

The corresponding discrete-time equation is [9]

$$\mathbf{z}_j = \mathbf{H}_j\mathbf{x}_j + \mathbf{w}_{m,j} \; . \tag{B.11}$$

B.1.4 Measurement Vector and Covariance

With

$$\mathbf{h}(\mathbf{x}) = \mathbf{H}\mathbf{x} \; , \tag{B.12}$$

the measurement innovation $\boldsymbol{\delta}\mathbf{z}^-$ may be defined as

$$\boldsymbol{\delta}\mathbf{z}^- = \mathbf{z} - \mathbf{h}(\hat{\mathbf{x}}^-) \; . \tag{B.13}$$

This quantity is therefore difference between the measurement vector and its prediction, whereby the latter is obtained from $\mathbf{h}$ evaluated in the state vector estimates at the end of the propagation phase, $\hat{\mathbf{x}}^-$.

Owing to their definition, measurement innovations consists of both the state estimation errors' propagation and the measurement errors which are uncorrelated with the states' estimates. In the Kalman filter, it is assumed that these measurement errors belong to a zero-mean distribution, generally assumed to be Gaussian, i.e., uncorrelated in time. The noise covariance matrix is defined as

$$\mathbf{R} = \mathrm{E}(\mathbf{w}_m\mathbf{w}_m{}^{\mathrm{T}}) \; , \tag{B.14}$$

which means that the ith diagonal element of $\mathbf{R}$ is the ith measurement vector component's variance.

B.1.5 Kalman Filter Algorithm

The algorithm that is described in this section pertains to an open-loop Kalman filter implementation. In this kind of implementation, no component of state vector estimate is fed-back to the system as it is done, instead, in a closed-loop implementation to correct the system itself [9]. This algorithm consists of ten steps, as depicted in Figure B.1.

In the 1st step, the transition matrix $\boldsymbol{\Phi}_{j-1}$ is calculated according to Section B.1.1. In the 2nd step, the system noise covariance matrix $\mathbf{Q}_{j-1}$ is computed. This matrix is defined as

$$\mathbf{Q}_{j-1} = \mathrm{E}(\boldsymbol{\Gamma}_{j-1}\mathbf{w}_{s,j-1}\mathbf{w}_{s,j-1}^{\mathrm{T}}\boldsymbol{\Gamma}_{j-1}) \tag{B.15}$$

and, usually, the $\mathbf{Q}$ matrix is designed after a tuning process.

In the 3$^{\text{rd}}$ step, the states' estimate are forwarded in time according to Equation (B.4). In the 4$^{\text{th}}$ step, the error covariance matrix is forwarded too, with [9]

$$\mathbf{P}_k^- = \mathbf{\Phi}_{j-1}\mathbf{P}_{j-1}^+\mathbf{\Phi}_{j-1}^{\text{T}} + \mathbf{Q}_{j-1} \quad . \tag{B.16}$$

The 5$^{\text{th}}$ step consists in the computation of the elements of the measurement matrix $\mathbf{H}_j$. In the 6$^{\text{th}}$ step, computation of the measurement noise covariance matrix $\mathbf{R}_j$, which, analogously to the system noise covariance matrix, is usually modeled by the Kalman filter designer through tuning [9].

The 7$^{\text{th}}$ step involves the Kalman gain matrix $\mathbf{K}_j$ calculation. This matrix embodies the weights of the new information provided by the measurements for the update of the state estimates and of the error covariance matrix. The expression for the Kalman gain matrix is obtained through the minimization of the error in the estimates $\hat{\mathbf{x}}_j^+$ by minimizing the trace of $\mathbf{P}_j^+$ with respect to the Kalman gain matrix itself [52].
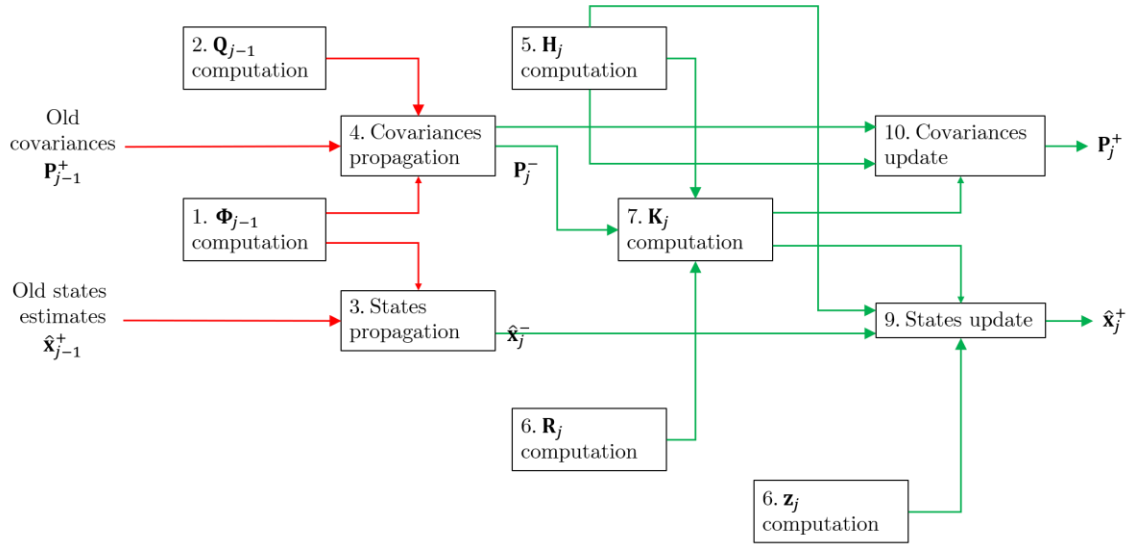
Figure B.1: Schematics of the main Kalman filter algorithm (based on [9]), with Propagation phase (red) and Measurement update phase (green)

In the 8$^{\text{th}}$ step the measurement vector $\mathbf{z}_j$ is formulated based on the raw measurements coming from the sensors

Finally, in the 9$^{\text{th}}$ and 10$^{\text{th}}$ steps, the states' estimates $\hat{\mathbf{x}}_j^-$ and the error covariance matrix $\mathbf{P}_j^-$, respectively, are updated. It can be shown that the update equations of $\hat{\mathbf{x}}_j^-$ and $\mathbf{P}_j^-$ are, respectively, [9]

$$\hat{\mathbf{x}}_j^+ = \hat{\mathbf{x}}_j^- + \mathbf{K}_j\delta\mathbf{z}_{j-1}^- \tag{B.17}$$

and

$$\mathbf{P}_j^+ = (\mathbf{I} - \mathbf{K}_j\mathbf{H}_j)\mathbf{P}_j^- \quad . \tag{B.18}$$

B.2 Extended Kalman Filter

When neither the system nor the measurement model can be assumed to be linear, nonlinear versions of the Kalman filter, such as the extended Kalman filter (EKF) shall be used [9]. The EKF features the nonlinear functions $\mathbf{f}(\mathbf{x})$ and $\mathbf{h}(\mathbf{x})$ instead of the $\mathbf{F}$ and $\mathbf{H}$. In this KF version, the time continuous system model is expressed by

$$\dot{\mathbf{x}}(t) = \mathbf{f}(\mathbf{x}(t), t) + \mathbf{G}(t)\mathbf{w}_s(t) \ . \tag{B.19}$$

From this, the propagation equation of the states' estimates can be obtained [9] as

$$\hat{\mathbf{x}}_j^- = \hat{\mathbf{x}}_{j-1}^+ + \int_{t_j - \tau_s}^{t_j} \mathbf{f}(\hat{\mathbf{x}}(t'), t')\mathrm{d}t' \ , \tag{B.20}$$

and, by assuming $\mathbf{f}$ constant over τ_s, (B.20) may be simplified as [9]

$$\hat{\mathbf{x}}_j^- = \hat{\mathbf{x}}_{j-1}^+ + \mathbf{f}(\hat{\mathbf{x}}_{j-1}^+, t_j)\tau_s \ . \tag{B.21}$$

In the EKF the absolute values of the errors in the states' estimates is assumed to be way smaller than the magnitudes of the state vector itself. This enables a linear model for the state vector residual [9]:

$$\delta\dot{\mathbf{x}}(t) = \mathbf{F}(t)\delta\mathbf{x}(t) + \mathbf{G}(t)\mathbf{w}_s(t) \ , \tag{B.22}$$

whereby the system matrix is linearized about the state vector estimate. In the time-discrete domain, this corresponds to:

$$\mathbf{F}_{j-1} = \left.\frac{\partial \mathbf{f}(\mathbf{x}, t_k)}{\partial \mathbf{x}}\right|_{\mathbf{x}=\hat{\mathbf{x}}_{j-1}^+} \ . \tag{B.23}$$

The time continuous measurement model is given by

$$\mathbf{z}(t) = \mathbf{h}(\mathbf{x}(t), t) + \mathbf{w}_m(t) \tag{B.24}$$

and the measurement innovation is

$$\delta\mathbf{z}_j^- = \mathbf{z}_j - \mathbf{h}(\hat{\mathbf{x}}_j^-, t_j) \ , \tag{B.25}$$

whereby the measurement vector at time t_j is

$$\mathbf{z}_j = \mathbf{h}(\mathbf{x}_j, t_j) + \mathbf{w}_{mj} \ . \tag{B.26}$$

The more the states' estimates have converged to the true state vector, the smaller the magnitude of the measurement innovation [9]. Therefore, a linear model may be formulated for the relationship between the measurement innovations and the state vector [9]:

$$\delta\mathbf{z}_j^- \approx \mathbf{H}_j\delta\mathbf{x}_j^- + \mathbf{w}_{mj} \ , \tag{B.27}$$

with

$$\mathbf{H}_j = \frac{\partial \mathbf{h}(\mathbf{x}, t_j)}{\partial \mathbf{x}}\bigg|_{\mathbf{x}=\widehat{\mathbf{x}}_j^-} = \frac{\partial \mathbf{z}(\mathbf{x}, t_j)}{\partial \mathbf{x}}\bigg|_{\mathbf{x}=\widehat{\mathbf{x}}_j^-}. \tag{B.28}$$

B.3 Loosely-coupled, Error-state Architecture

In a loosely coupled integration architecture each navigation subsystem enters its own computed navigation solution, or at least its own computed component of the navigation solution, to the fusing Kalman filter-based estimator, which may be for example the Extended Kalman Filter. By navigation solution, generally the three components, each, of position and velocity are meant, while a navigation solution component is herein used to refer to one of the components of position or velocity. In the case of an altimeter, the delivered navigation solution component is the third component of the position, provided the position is expressed in terms of latitude, longitude, and altitude. GNSS is generally capable to provide a full navigation solution, i.e., a tridimensional position measurement and a tridimensional velocity measurement, instead. Depending on the use case, the expression "navigation solution" may comprise also the states needed for a description of attitude [9].

More in particular, in the case of an error-state implementation, what actually enters the estimator is the deviation of this navigation solution component from its counterpart generated by the reference navigation subsystem, which is often an INS. This fusion architecture is schematically represented in Figure B.2.

Formally speaking, the state vector $\mathbf{x}$ contains the reference navigation subsystem's error states, denoted by $\mathbf{x}_{Ref}$, and the states of each aiding subsystem, $\mathbf{x}_{sub,i}$, known as augmented states. As the reference navigation subsystem is often an INS, the subscript Ref is changed to INS. With n aiding subsystems, the state vector is

$$\mathbf{x} = \begin{pmatrix} \mathbf{x}_{INS} \\ \mathbf{x}_{sub,1} \\ \mathbf{x}_{sub,2} \\ \vdots \\ \mathbf{x}_{sub,n} \end{pmatrix}. \tag{B.29}$$

The vector $\mathbf{x}_{INS}$ comprises the error in the navigation solution and potentially also some states for the biases and/or scale factors of the IMU (Inertial Measurement Unit) Similarly, $\mathbf{x}_{sub,i}$ consists of the biases/scale factor errors of the i-th subsystem that are desired to be estimated. Indeed, error states do not necessitate to be estimated for each navigation subsystem [9].

In the case the position is given in terms of altitude, longitude and altitude, the error states for the position are

$$\delta\mathbf{p} = \begin{pmatrix} \delta L \\ \delta \lambda \\ \delta h \end{pmatrix} = \begin{pmatrix} \tilde{L} - L \\ \tilde{\lambda} - \lambda \\ \tilde{h} - h \end{pmatrix} \tag{B.30}$$

where ~ denotes a measured quantity.
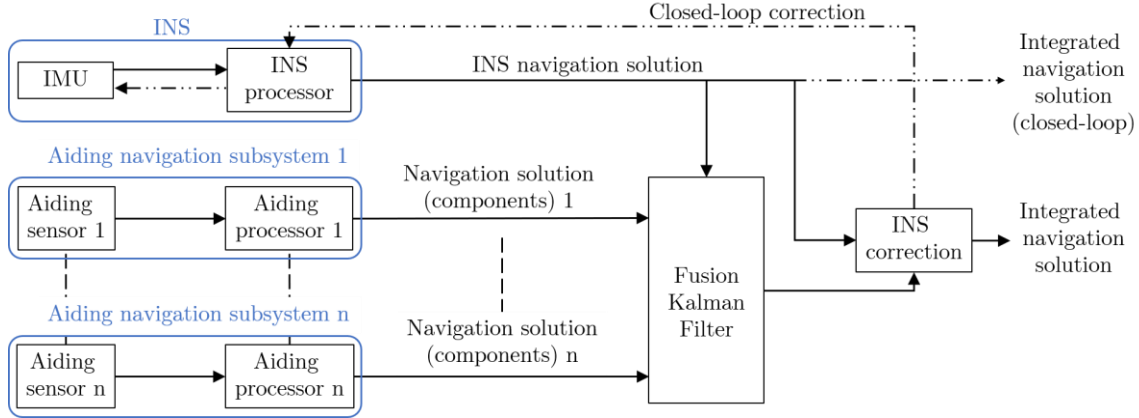
Figure B.2: Loosely coupled, error-state integration architecture in navigation (based on [9])

Getting back to the example of an altimeter as aiding system, whereby the general subscript sub, i is substituted by a, the corresponding component of the Kalman filter measurement vector is the difference between the altitude measured by the altimeter and its counterpart measured by the INS:

$$z_a = \tilde{h}_a - \tilde{h} \tag{B.31}$$

The measurement innovation is then

$$\delta z_a^- = \tilde{h}_a - \delta \hat{h}_a^- - \hat{h}^- \ , \tag{B.32}$$

where $\delta \hat{h}_a^-$ is the Kalman filter -estimated error in the altimeter's measurement, which may be potentially computed from $\mathbf{x}_b$, if some states of this subsystem are among the KF augmented states. If, for example, just a static bias b_b of the aforementioned altimeter was to be estimated, then $\delta \hat{h}_a^-$ would coincide with this bias. The third term in Equation (B.32) denotes the altitude in the predicted navigation solution.

At a given KF iteration, the measurement matrix portion corresponding to the altimeter is then [9]

$$H_{a,j} = \left(\frac{\partial z_a}{\partial \mathbf{x}_{INS}} \quad \mathbf{0} \quad \frac{\partial z_a}{\partial \mathbf{x}_a} \quad \mathbf{0} \right)_{\mathbf{x} = \widehat{\mathbf{x}}_j^-} . \tag{B.33}$$

Regarding the KF system model, it is known that INS and GNSS do not interact within it. Indeed, their only interactions takes place in the measurement model. As a result, the overall system matrix F, the transition matrix $\boldsymbol{\Phi}$ and the system noise covariance matrix $\mathbf{Q}$ can be partitioned in the following way:

$$\mathbf{F} = \begin{pmatrix} \mathbf{F}_{INS} & \mathbf{0} \\ \mathbf{0} & \mathbf{F}_G \end{pmatrix}, \qquad \boldsymbol{\Phi} = \begin{pmatrix} \boldsymbol{\Phi}_{INS} & \mathbf{0} \\ \mathbf{0} & \boldsymbol{\Phi}_G \end{pmatrix}, \qquad \mathbf{Q} = \begin{pmatrix} \mathbf{Q}_{INS} & \mathbf{0} \\ \mathbf{0} & \mathbf{Q}_G \end{pmatrix}, \tag{B.34}$$

with the subscript G denoting the GNSS partitions [9].

In an analogous way, it may be assumed that in general, within a peculiar Kalman filter -based navigation system, all navigation subsystems interact with the INS only in the measurement model. For the system matrix, this would yield:

$$\mathbf{F} = \begin{pmatrix} \mathbf{F}_{INS} & \cdots & \mathbf{0} & \mathbf{0} \\ \mathbf{0} & \mathbf{F}_{sub,1} & \mathbf{0} & \vdots \\ \vdots & \mathbf{0} & \ddots & \mathbf{0} \\ \mathbf{0} & \cdots & \mathbf{0} & \mathbf{F}_{sub,n} \end{pmatrix} , \tag{B.35}$$

and analogous shapes would result for the transition and the system noise covariance matrices.

It may also be assumed that there is no correlation between the measurement noise sources of the various aiding subsystems. This would result in the measurement noise covariance matrix being partitioned as:

$$\mathbf{R} = \begin{pmatrix} \mathbf{R}_{sub,1} & \cdots & \mathbf{0} \\ \vdots & \ddots & \mathbf{0} \\ \mathbf{0} & \mathbf{0} & \mathbf{R}_{sub,n} \end{pmatrix} . \tag{B.36}$$

If for the i-th navigation subsystem only a state is added to the KF state vector as an augmented state, then the $\mathbf{F}_{sub,i}$ partition of $\mathbf{F}$, degenerates into a scalar. In particular, if this augmented state corresponds, e.g., to a bias assumed to be static, i.e., without a known time variation, then $\mathbf{F}_{sub,i} = 0$. This, in turn, according to what is said in Section B.1.1, yields $\mathbf{\Phi}_{sub.i} = 1$.

Moreover, if the i-th navigation subsystem always provides a one-dimensional measurement, its corresponding $\mathbf{R}$ matrix's partition, i.e., $\mathbf{R}_{sub,i}$, is a scalar.

C. Gauss-Markov-Process Structure for Augmented States

The time correlation structures of realistic sensor errors may have complex structures. In order to model them within practical applications, Gauss-Markov Processes are often adopted both due to their modeling accuracy and to their simple two-parameters formulation. Furthermore, such models can be integrated in a KF by state augmentation without great complexity [53].

In a KF-based navigation systems, the dynamic components of accelerometers' and gyros' biases should be modeled, as augmented states within $\mathbf{x}_{INS}$, as exponentially fixed-variance 1st-order Markov processes, also known as 1st-order Gauss-Markov processes [9]. In general. In many systems, such as satellite-based or INSs, some sources of time-correlated sensor errors can be well modeled with stationary 1st-order Gauss-Markov processes (GMP) [53].

A stationary time-continuous first-order GMP a, with a gaussian noise component, is given by [53]

$$\dot{a}(t) = \frac{1}{\tau}a(t) + \sqrt{\frac{2\sigma^2}{\tau}}w(t) \ , \quad \text{with } w(t){\sim}N(0,1), \tag{C.1}$$

where $N(0,1)$ denotes a gaussian (or normal) distribution with zero mean and a standard deviation of 1. The GMP standard deviation and correlation time constant (also known as time constant)—denoted by σ and τ, respectively—are such that $\sigma \in \mathbb{R} \geq 0$ and $\tau \in \mathbb{R} > 0$. Anyway, since sensor outputs are often processed via digital computers, discrete-time first-order GMPs may be used to model sensor errors. Such a GMP can be expressed as:

$$a_n = \alpha a_{n-1} + \sqrt{\sigma^2(1-\alpha^2)}w_n \ , \qquad \text{with } w_n(t){\sim}N(0,1) \ , \tag{C.2}$$

where $\alpha = e^{\frac{-\Delta t}{\tau}}$ and Δt is the time interval between two successive time instants, i.e., $\Delta t = t_n - t_{n-1}$ [53].

When in a KF-based estimator, such as the one presented in the current section, the i-th aiding subsystem features only one augmented state, like a dynamic bias, and this is modeled as a discrete-time stationary first-order GMP, then from (C.5) it follows that

$$\mathbf{\Phi}_{sub,i} = \alpha_{sub,i} \ . \tag{C.3}$$

In Equation (C.3), $\alpha_{sub,i} = \exp(-\Delta t/\tau_{sub,i})$, Δt is the time interval between two

successive KF iterations and $\tau_{sub,i}$ is the time constant of the GMP used for the modeling of the i-th subsystem's augmented state. Additionally, in this case it may be shown that [9]

$$\mathbf{Q}_{sub,i} = \sigma_{sub,i}^2 (1 - \alpha_{sub,i}^2) \ . \tag{C.4}$$

When the values of the two parameters of this GMP model are uncertain, misleading error estimation within the KF can arise. Realistic and conservative values are therefore needed to upper bound the estimation errors when system noise sources can be modeled with a GMP structure [53]. Indeed, it is shown that one can upper bound the true KF estimation error covariance if the Power Spectral Density (PSD) of the system error model overbounds the one of the actual sensor errors for all frequencies [54].

In this work, a barometric altimeter's dynamic bias is integrated in a state vector as an augmented state with GMP structure. Values for the corresponding standard deviation and time constant are obtained by overbounding the PSD of this dynamic bias, as it is described in Section 8.1.1. In this regard, it is useful to write the expression for the PSD, denoted by S, of a time-discrete stationary first-order GMP:

$$S(\omega) = \frac{\sigma^2 \Delta t (1 - \alpha^2)}{1 + \alpha^2 - 2\alpha \cos(\omega \Delta t)} \tag{C.5}$$

where ω is the angular frequency, which is defined as $\omega = 2\pi f$, with f denoting the linear frequency [53].

List of Figures

111

List of Tables

Bibliography

[1] "Altitude, Flight Level and Height," SKYbrary, 20 July 2017. [Online]. Available: https://www.skybrary.aero/index.php/Altitude,_Flight_Level_and_Height. [Accessed 17 June 2021].

[2] Federal Aviation Administration, "Pilot/Controller Glossary," 12 October 2017. [Online]. Available: https://www.faa.gov/air_traffic/publications/media/pcg_chg_3_2-28-19.pdf. [Accessed 17 June 2021].

[3] "Altimeter Pressure Settings," SKYbrary, 26 February 2020. [Online]. Available: https://www.skybrary.aero/index.php/Altimeter_Pressure_Settings. [Accessed 16 June 2021].

[4] "Rules of the Air, Annex 2 to the Convention on International Civil Aviation," International Civil Aviation Organization (ICAO), Montreal, 2005.

[5] "ICAO Doc 8168, OPS/611, Procedures for Air Navigation Services, Aircraft Operations, Volume I, Flight Procedures," International Civil Aviation Organization (ICAO), 2006.

[6] R. Blanchard, "A New Algorithm for Computing Inertial Altitude and Vertical Velocity," *IEEE Transactions on Aerospace and Electronic Systems,* Vols. AES-7, no. 6, pp. 1143-1146, 1971.

[7] R. Blanchard, "An Improvement to an Algorithm for Computing Aircraft Reference Altitude," *IEEE Transactions on Aerospace and Electronic Systems,* Vols. AES-8, no. 5, pp. 685-687, 1972.

[8] E. Nossek, M. Suess, B. Belabbas and M. Meurer, "Analysis of Position and Timing Solutions for an APNT-System – A Look on Convergence, Accuracy and Integrity," in *Proceedings of the 27th International Technical Meeting of the Satellite Division of The Institute of Navigation (ION GNSS+ 2014)*, Tampa, Florida, 2014.

[9] P. D. Groves, Principles of GNSS, Inertial, and Multisensor Integrated Navigation Systems, Boston: Artec House, 2013.

[10] D. Macias-Valadez, R. Santerre, S. Larochelle and R. Landry, "Improving vertical GPS precision with a GPS-over-fiber architecture and real-time relative delay calibration," *GPS Solutions,* vol. 16, no. 4, pp. 449-462, 2012.

[11] T.-C. Li and V. Chueh, "Errors in the Pressure and Blanchard Altitudes for a

Cross Country Flight," in *Position Location and Navigation Symposium (PLANS), 2010 IEEE/ION*, Indian Wells, 2010.

[12] T.-C. Li and R. D. Shaner, "Analysis of pressure and Blanchard altitude errors computed using atmospheric data obtained from an F-18 aircraft flight," in *2002 IEEE Position Location and Navigation Symposium*, Palm Springs, 2002.

[13] T.-C. Li and D. N. Thunborg, "Pressure and Blanchard Altitudes Computed from Atmospheric Data Gathered from May through July 2000 at White Sands, New Mexico," in *Proceedings of the 57th Annual Meeting of The Institute of Navigation*, Albuquerque, 2001.

[14] S. Gaglione, A. Angrisano, G. Castaldo, C. Gioia, A. Innac, L. Perrotta, G. Del Core and S. Troisi, "GPS/Barometer augmented navigation system: Integration and integrity monitoring," in *2015 IEEE Metrology for Aerospace (MetroAeroSpace)*, Benevento, 2015.

[15] C. Hajiyev, U. Hacizade and D. Cilden-Guler, "Integration of barometric and GPS altimeters via adaptive data fusion algorithm," *International Journal of Adaptive Control and Signal Processing,* vol. 35, no. 1, pp. 2-14, 2021.

[16] X. Liang, C. Milner, C. Macabiau and P. Estival, "Integrity monitoring for A-PNT using barometric measurements aided MultiDMEs," in *Proceedings of the 33rd International Technical Meeting of the Satellite Division of The Institute of Navigation (ION GNSS+ 2020)*, Online, 2020.

[17] H. Hersbach, B. Bell, P. Berrisford, G. Biavati, A. Horányi, J. Muñoz Sabater, J. P. C. Nicolas, R. Radu, I. Rozum, D. Schepers, A. Simmons, C. Soci, D. Dee and J.-N. Thépaut, "ERA5 hourly data on pressure levels from 1979 to present," Copernicus Climate Change Service (C3S) Climate Data Store (CDS), 2018. [Online]. Available: DOI: 10.24381/cds.bd0915c6. [Accessed 15 June 20121].

[18] H. Hersbach, B. Bell, P. Berrisford, G. Biavati, A. Horányi, J. Muñoz Sabater, J. P. C. Nicolas, R. Radu, I. Rozum, D. Schepers, A. Simmons, C. Soci, D. Dee and J.-N. Thépaut, "ERA5: data documentation," European Center Medium Weather Forecast (ECMWF), 10 June 2021. [Online]. Available: https://confluence.ecmwf.int/display/CKB/ERA5%3A+data+documentation. [Accessed 15 June 2021].

[19] NGS.Webmaster, "What is the geoid?," National Geodetic Survey, 30 January 2001. [Online]. Available: https://geodesy.noaa.gov/GEOID/geoid_def.html. [Accessed 15 June 2021].

[20] B. Scherllin-Pirscher, A. K. Steiner, G. Kirchengast, M. Schwärz and S. S. Leroy, "The power of vertical geolocation of atmospheric profiles from GNSS radio occultation," *Journal of Geophysical research: atmospheres,* vol. 122, pp. 1595-1616, 2017.

[21] K. Brown, "Geophysical Altitudes," mathpages, [Online]. Available: https://www.mathpages.com/home/kmath054/kmath054.htm. [Accessed 15 June 2021].

[22] D. W. 8. D. Committee, "Department of Defense World Geodetic System 1984, Its Definition and Relationships with Local Geodetic Systems," Detense Mapping Agency, Fairfax, 1991.

[23] "Department of Defense World Geodetic system 1984, Its Definition and Relationships with Local Geodetic Systems, Version 1.0.0," National Geospatial-Intelligence Agency (NGA), Office of Geomatics, Arnold, 2014.

[24] "Manual of ICAO Standard Atmospheree, extended to 80 kilometres (262 500 feet), Document 7488/3," International Civil Aviation Organization, Montreal, 1993.

[25] A. Giez, C. Mallaun, M. Zöger, A. Dörnbrack and U. Schumann, "Static Pressure from Aircraft Trailing-Cone Measurements and Numerical Weather-Prediction Analysis," *Journal of Aicraft,* vol. 54, no. 5, 2017.

[26] "Minimum Operational Performance Standard (MOPS) for GNSS Aided Inertial Systems," RTCA, Inc., Washington, 2020.

[27] "Altimeter Temperature Error Correction," SKYbrary, 25 June 2021. [Online]. Available: https://www.skybrary.aero/index.php/Altimeter_Temperature_Error_Correction . [Accessed 17 June 2021].

[28] "EUROCONTROL Guidelines for Cold Temperature Corrections by ATS," EUROCONTROL, Brussels, 2014.

[29] G. M. Siouris, Aerospace Avionics Systems, Academic Press, Inc.: San Diego, 1993.

[30] "Transition Altitude/Level," SKYbrary, 18 September 2018. [Online]. Available: https://www.skybrary.aero/index.php/Transition_Altitude/Level. [Accessed 17 June 2021].

[31] "The Fourth Meeting of the South Asia/Indian Ocean ATM Coordination Group (SAIOACG/4) and the Twenty first Meeting of the South East Asian ATM Coordination Group (SEACG/21), ESTABLISHING A HARMONIZED TRANSITION ALTITUDE IN INDIA," International Civil Aviation Organization, Hong Kong, 2014.

[32] "Corrigendum to A-NPA 2012-01 of 28 February 2012 on Harmonised Transition Altitude," European Aviation Safety Agency, 2012.

[33] S.-s. Jan, D. Gebre-Egziabher, W. Todd and P. Enge, "Improving GPS-based landing system performance using an empirical barometric altimeter confidence bound," *IEEE Transactions on Aerospace and Electronic Systems,* vol. 44, no. 1, pp. 127-146, 2008.

[34] D. Wessmann and A. Rubin, "Vertical distances," Wikimedia Commons, 21 October 2009. [Online]. Available: https://commons.wikimedia.org/wiki/File:Vertical_distances.svg. [Accessed 5 July 2021].

[35] "Meteorological Terminal Air Report (METAR)," SKYbrary, 1 April 2019. [Online]. Available:

https://www.skybrary.aero/index.php/Meteorological_Terminal_Air_Report_(M ETAR). [Accessed 16 June 2021].

[36] "Altimeter Setting Procedures," SKYbrary, 16 April 2021. [Online]. Available: https://www.skybrary.aero/index.php/Altimeter_Setting_Procedures. [Accessed 17 June 2021].

[37] "The Second UK State Consultation on a Harmonised Transition Altitude (TA) of 18,000ft in the London and Scottish Flight Information Regions - Aviation Stakeholder Consultation Feedback Report," Civil Aviation Authority, Gatwick Airport South, 2016.

[38] N. Assorov, E. Nechaev and P. Surint, "ABOUT THE TRANSITION TO QNH PRESSURE IN THE RUSSIAN FEDERATION," *Civil Aviation High TECHNOLOGIES,* vol. 21, pp. 8-19, 2018.

[39] "Minimum Safe Altitude (MSA)," SKYbrary, 27 July 2017. [Online]. Available: https://www.skybrary.aero/index.php/Minimum_Safe_Altitude_(MSA). [Accessed 18 June 2021].

[40] "Meteorological Wind Directioin," San Francisco State University, Department of Earth & Climate Sciences, [Online]. Available: http://tornado.sfsu.edu/geosciences/classes/m430/Wind/WindDirection.html. [Accessed 16 June 2021].

[41] A. Mañero Contreras and C. Hajiyev, "Comparison of Conventional and Robust Adaptive Kalman Filters Based Integrated Altimeters," in *2019 20th International Carpathian Control Conference (ICCC)*, Krakow-Wieliczka, 2019.

[42] S.-s. Jan, D. Gebre-Egziabher, T. Walter and P. Enge, "Improving GPS-Based Landing System Performance using an Empirical Barometric Altimeter Confidence Bound," *IEEE Transactions on Aerospace and Electronic Systems,* vol. 44, no. 1, p. January, 2008.

[43] J. Lee, E. Hyeon, M. Kim and J. Lee, "Vertical Position Error Bounding for Integrated GPS/Barometer Sensors to Support Unmanned Aerial Vehicle (UAV)," in *30th Congress of the International Council of the Aeronautical Sciences (ICAS)*, Daejeon, 2016.

[44] A. Giez, C. Mallaun, M. Zöger, A. Dörnbrack and U. Schumann, "Use of Numerical Weather Prediction Analysis for Testing Pressure Altitude Measurements on Aircraft - An Application Example," in *Avionics & Space Testing*, Munich, 2017.

[45] S. Fritts, "The Complete Guide to Understanding METARs," Think Aviation, 4 January 2021. [Online]. Available: https://www.thinkaviation.net/understanding-metars-part-1/. [Accessed 18 June 2021].

[46] "How to Read An Aviation Routine Weather (METAR) Report," Drone Pilot Ground School, 23 July 2016. [Online]. Available: https://www.dronepilotgroundschool.com/reading-aviation-routine-weather-metar-report/#. [Accessed 19 June 2021].

[47] S. A. Beresnev, V. I. Gryazin and K. G. Gribanov, "Analysis of Wind Vertical Component Characteristics in the Stratosphere," *Russian Meteorology and Hydrology,* vol. 34, no. 11, pp. 724-731, 2009.

[48] C. Mallaun, A. Giez and R. Baumann, "Calibration of 3-D wind measurements on a single-engine research aircraft," *Atmospheric Measurement Techniques,* vol. 8, pp. 3177-3196, 1015.

[49] J. Blanch, T. Walter and P. Enge, "Gaussian Bounds of Sample Distributions for Integrity Analysis," *IEEE Transactions on Aerospace and Electronic Systems,* vol. 55, no. 4, pp. 1806-1815, 2018.

[50] "Gaussian Overbound," Stanford GPS Lab, Aeronautics & Astronautics Department, [Online]. Available: https://gps.stanford.edu/resources/software-tools/gaussian-overbound. [Accessed 08 July 2021].

[51] S. S. Osder and M. Kayton, "Air-Data Systems," in *Avionics Navigation Systems, 2nd Edition*, Boston, Wiley-Interscience, 1997, pp. 393-425.

[52] R. Brown and P. Hwang, Introduction to Random Signals and Applied Kalman Filtering with Matlab Exercises, 4th Edition, Boston: Wiley, 2012.

[53] O. García Crespillo, M. Joerger and S. Langel, "Tight Bounds for Uncertain Time-Correlated Errors with Gauss-Markov Structure," 2020.

[54] S. Langel, O. García Crespillo and M. Joerger, "A New Approach for Modeling Correlated Gaussian Errors using Frequency Domain Over-bounding," in *Position, Navigation and Timing Symposium (PLANS)*, 2020.